Experimental astrophysics with high power lasers and *Z* pinches

Bruce A. Remington*

Lawrence Livermore National Laboratory, Livermore, California 94450, USA

R. Paul Drake†

University of Michigan, Ann Arbor, Michigan 48109, USA

Dmitri D. Ryutov‡

Lawrence Livermore National Laboratory, Livermore, California 94450, USA

(Published 8 August 2006)

With the advent of high-energy-density (HED) experimental facilities, such as high-energy lasers and fast *Z*-pinch, pulsed-power facilities, millimeter-scale quantities of matter can be placed in extreme states of density, temperature, and/or velocity. This has enabled the emergence of a new class of experimental science, HED laboratory astrophysics, wherein the properties of matter and the processes that occur under extreme astrophysical conditions can be examined in the laboratory. Areas particularly suitable to this class of experimental astrophysics include the study of opacities relevant to stellar interiors, equations of state relevant to planetary interiors, strong shock-driven nonlinear hydrodynamics and radiative dynamics relevant to supernova explosions and subsequent evolution, protostellar jets and high Mach number flows, radiatively driven molecular clouds and nonlinear photoevaporation front dynamics, and photoionized plasmas relevant to accretion disks around compact objects such as black holes and neutron stars.

DOI: 10.1103/RevModPhys.78.755 PACS number(s):

CONTENTS

I. Introduction 755
II. Facilities and Capabilities 756
A. Introduction 756
B. High-energy lasers 756
C. Fast *Z* pinches and other pulsed power facilities 757
D. Astrophysics experiments 758
III. Opacities and Cepheid Variables 759
IV. Hydrodynamics of Core-Collapse Supernovae 762
A. Introduction 762
B. Multidimensional hydrodynamics in core-collapse supernovae 763
C. A sample problem: Shock wave breakout through the He-H interface 765
D. Issues of the hydrodynamic similarity 766
E. Experiments on SN type-II hydrodynamics 768
V. Supernova Remnants, Blast Waves, and Radiation 771
A. Introduction 771
B. General features of supernova remnants 771
C. Simulating one-dimensional dynamics 773
D. Interaction of shocks and clumps 773
E. Radiative effects in shocks 775
F. Blast waves 778
G. Summary 779
VI. Protostellar Jets and High Mach Number Flows 779
VII. Hydrodynamics of Photoevaporated Molecular Clouds 784
A. Introduction 784
B. Main physical processes 785
C. Hydrodynamic models of the formation of the elephant trunks 786
D. Laboratory experiments 786
E. Issues for experiments and theory 787
VIII. Planetary Interiors and Equations of State 788
IX. Compact Object Accretion Disks and Photoionized Plasmas 791
X. Outlook for the Future 796
Acknowledgments 797
References 797

*Electronic address: remington2@llnl.gov
†Electronic address: rpdrake@umich.edu
‡Electronic address: ryutov1@llnl.gov

I. INTRODUCTION

Over the past two decades, we have seen the emergence of a new experimental capability in the form of high-energy density (HED) facilities. These include high power lasers and fast magnetic pinch machines ("*Z* pinches"), which were developed largely as a result of the national inertial confinement fusion (ICF) program (Lindl *et al.*, 2004; Matzen *et al.*, 2005). Hand in hand with the emergence of these HED experimental facilities came the realization that a new class of laboratory astrophysics could be pursued (Ripin *et al.*, 1990; Rose, 1991; Drake, 1999; Remington *et al.*, 1999, 2000; Takabe, 2001; Remington, 2005). This new class of experimental HED astrophysics is complementary to but distinct from traditional laboratory astrophysics, such as measurements of low-energy nuclear cross sections. The new HED facilities allow matter to be placed, reproducibly, in extreme states of temperature, density, and velocity.

 ©2006 The American Physical Society

Measurements of these conditions and their evolution, when properly diagnosed, allow theoretical models and computer simulation codes to be tested under the extreme conditions relevant to HED regimes of astrophysics. Examples include measurements of (i) opacities relevant to stellar interiors (Rogers and Iglesias, 1994, 1998; Arnett, 2001; Bailey *et al.*, 2002; Chenais-Popovics, 2002; Wang *et al.*, 2004), (ii) the phase, conductivity, and equations of state of matter under conditions relevant to planetary interiors (Celliers *et al.*, 2004; Knudson *et al.*, 2004; Koenig *et al.*, 2004; Saumon and Guillot, 2004), (iii) scaled, strong-shock-driven turbulent dynamics relevant to supernova explosions (Robey, Zhou, *et al.*, 2003; Drake, Leibrandt, *et al.*, 2004; Miles, Braun, *et al.*, 2004); and (iv) ionization states of radiatively pumped photoionized plasmas relevant to accretion disks surrounding black holes or neutron stars (Foord *et al.*, 2004). Such measurements allow astrophysical models and large-scale simulation techniques to be tested and verified under relevant conditions. In each of these four areas, astrophysical models and simulations have been tested against HED laboratory data, leading to improvements in the models or modeling techniques, or a realization of the limitations of the simulation methods.

To achieve the relevant high-temperature, high-pressure, or strong shock conditions requires focusing macroscopic amounts of energy ($E \gtrsim 1$ kJ) into small spatial scales ($L \lesssim 1$ mm) over very short time intervals ($\delta t \ll 1$ μs). This allows the heating rates to greatly exceed the losses, resulting in high temperatures, pressures, and densities. High-energy, pulsed lasers achieve this by their ability to focus their energy into microscopic volumes over nanosecond time scales. Magnetic pinch facilities (Z pinches) achieve this by discharging large currents ($\gtrsim 1$ MA) through a cylindrical can or wire array that then implodes due to the $\mathbf{J} \times \mathbf{B}$ forces. Upon stagnation on the axis, the kinetic energy of imploding wires and the magnetic energy of the axial current is converted into an intense burst of heat and radiation. Both approaches for achieving HED conditions in the laboratory have been developed successfully over the past two decades. Sophisticated time, spatially, and spectrally resolved diagnostics have also been developed (Budil *et al.*, 1997; Boehly *et al.*, 1999; Koch *et al.*, 1999; Heeter *et al.*, 2001; Landen *et al.*, 2001). It was only after the deployment of such diagnostics on these facilities that the field of HED laboratory astrophysics has emerged and grown.

Connections to astrophysics achievable on these HED facilities have been pursued vigorously over the past decade, and the rate of progress has been steadily increasing. This is the topic of our review article, which is written with two separate audiences in mind: plasma physicists (such as laser experimenters, for example) and astrophysicists. We try to discuss each topic at a level that an interested researcher, not necessarily expert in the specifics, can still follow the essence of the discussion. Ample references are given, so that more in depth reading can easily be pursued. In Sec. II, a discussion of HED facilities is given, along with descriptions of typical classes of experiments. Section III is dedicated to a discussion of opacities and their impact on pulsating stars, such as the Cepheid variables. We discuss supernovae and supernova remnants, along with relevant laboratory experiments, in Secs. IV and V. Protostellar jets, high Mach number flows, and relevant experiments are discussed in Sec. VI. The dynamics of photoevaporation fronts in radiatively driven molecular clouds, such as the Eagle Nebula, are described in Sec. VII. Planetary interiors and the properties of matter under extreme states of pressure and density are the subject of Sec. VIII, and the radiatively dominated conditions around an accreting compact object are discussed in Sec. IX. We conclude with an outlook for the future in Sec. X.

II. FACILITIES AND CAPABILITIES

A. Introduction

The emerging field of high-energy-density laboratory astrophysics could not have developed 20 years ago. The necessary energy sources and diagnostic technologies did not exist. In the present section, we provide an overview of the remarkable facilities that can concentrate energy to levels of MJ/cm^3, and then diagnose the results as a function of time, space, and spectral content. We begin with a description of pulsed, high-energy lasers and fast Z pinches and then discuss two examples of typical astrophysics-related experiments.

B. High-energy lasers

A number of high-energy lasers have been constructed during the past 30 years, motivated by the challenge of achieving "inertial confinement fusion." The long-term goal is to create miniature fusion explosions with an energy gain of about 100. Such a laser system begins with a very high-quality laser beam, initially of low energy, which propagates through and extracts energy from Nd-doped laser glass. The first challenge is to prevent defects and diffraction from damaging the laser components as the energy per unit area of the laser beam reaches high levels. The second is to extract a large fraction of the stored energy. The first challenge was met in the 1970s, leading to several high-energy lasers capable of delivering >1 kJ of laser energy to a target. The largest of these lasers include the Omega laser at the Laboratory for Laser Energetics of the University of Rochester (Boehly *et al.*, 1999), the Gekko XII laser at Osaka University in Japan (Yamanaka *et al.*, 1987), and formerly the Nova laser at the Lawrence Livermore National Laboratory (Campbell *et al.*, 1986). A number of similar but smaller lasers have also contributed to the results discussed below, such as LULI at Ecole Polytechnique in Paris, France; Vulcan at Rutherford-Appleton Laboratory near Oxford, England; Trident at Los Alamos National Laboratory; Helen at Atomic Weapons Establishment laboratory in Aldermaston, England; Janus at Lawrence Livermore

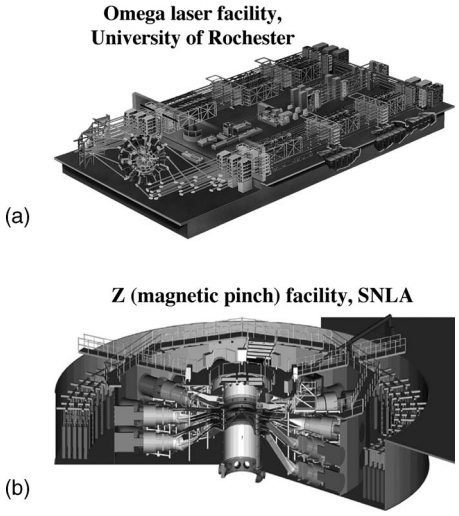

FIG. 1. Examples of high-energy-density experimental facilities. (a) The Omega laser facility. Note the "switchyard" at the left: it is used to distribute 60 laser beams as evenly as possible around the vacuum chamber where the target is situated. Such an arrangement is dictated by the principal objective of the Omega facility, which is the study of "direct drive" fusion (Boehly *et al.*, 1999). Image provided courtesy of the University of Rochester Laboratory for Laser Energetics. (b) Schematic of the *Z* facility at Sandia National Laboratories (Albuquerque). The outermost part is formed by Marx generators. They are connected to 36 water-insulated transmission lines which, in turn, feed magnetically insulated vacuum transmission lines converging at the central "diode," where energy is delivered to an experiment. This facility is now being refurbished, to increase the current from 20 to 30 MA (Matzen *et al.*, 2005). Image provided courtesy of the Sandia National Laboratory at Albuquerque.

National Laboratory; and the Nike laser at the Naval Research Laboratory, which amplifies KrF light in gas.

Figure 1(a) shows one example of such a laser system, the Omega facility, which can deliver 30 kJ to a target. The laser occupies approximately the area of one (American) football field. The initial laser beam, formed and amplified in the center of the laser bay, is split, amplified further, and eventually feeds the 60 amplifier chains that proceed down the sides of the laser bay toward the output end. Frequency conversion crystals then triple the frequency of these laser beams, decreasing their wavelength from 1.05 to 0.35 μm, and mirrors direct the laser beams toward the center of the target chamber. Typical laser pulse durations can range over 0.2–10 ns, and can be flat-topped, Gaussian, or custom-designed shapes. Beams can be individually pointed and focused, and within limits individually timed. Spot intensity spatial profiles can be tailored with phase plates, with spot diameters in the range of 0.2–1 mm. Larger spots, up to ~3 mm diameter, can be achieved by removing the phase plates and defocusing the beams.

The second challenge cited above, of using the stored energy more efficiently, is being met by the National Ignition Facility (NIF), now under construction at Livermore (Hogan *et al.*, 2001; Miller, 2004; Moses, 2004) and by the Laser MegaJoule (LMJ) under construction in France (Bettinger and Decroisette, 1999). For the laser beam to extract more of the stored energy it must pass through the Nd-doped glass several times, without destroying the quality or the focusability of the laser beam. The NIF and LMJ laser systems, with 192 and 240 beams, respectively, are anticipated to deliver ~2 MJ of laser energy to a target. This will enable the study of larger, hotter systems involving stronger shock waves and higher energy density configurations. Important new regimes will become accessible with these higher energy lasers; as discussed briefly in Sec. X.

C. Fast *Z* pinches and other pulsed power facilities

Pulsed power devices are also proving to be useful for experiments related to astrophysics. A pulsed power machine delivers a large current (and voltage) to a load, in a short, intense pulse (varying from a few ns to a few hundred ns). The most common device driven by pulsed power is a *Z* pinch (Ryutov, Derzon, and Matzen, 2000). In a *Z* pinch, stored electrical energy drives a large current through a cylindrical conductor, resulting in a large magnetic pinch force. This force accelerates the conducting matter inward, causing it to collide at the center of the pinch, converting kinetic energy and magnetic energy to thermal energy, much of which is radiated as x rays.

The largest of the existing *Z*-pinch facilities is the "*Z*" generator at Sandia, shown in Fig. 1(b), which can generate a current of 20 MA; it is now being refurbished to increase the current to ~30 MA and to provide a substantial degree of control over the pulse shape (Matzen *et al.*, 2005). There exist also two 5–10-MA facilities, the Saturn facility at Sandia and Angara-5 at Troitsk (Russia), as well as several 1-MA facilities, of which the MAGPIE generator at the Imperial College (London) is used most actively for experiments in laboratory astrophysics.

Z-pinch experiments permit several possible applications. First, by using an array of hundreds of high-*Z* wires one can obtain efficient conversion of electrical energy into thermal x rays (Sanford *et al.*, 2000). The *Z* machine at Sandia National Laboratories, as shown in Fig. 1(b), for example, can produce nearly 2 MJ of thermal x rays at a temperature above 1×10^6 deg. This x-ray energy can be used to launch a shock wave, but with much more energy and over a much larger area than is possible in laser experiments, which can be an advantage (Drake, 2002a). Second, by using many wires of moderate-*Z* material, one can produce large fluxes of $K\alpha$ x rays at energies of a few keV. This is useful for radiation transport experiments. Third, by manipulating the wires themselves one can produce other effects of interest. For example, by using a conical wire array one can produce a jet of material that radiatively collapses and is relevant to astrophysical jets (Lebedev *et al.*, 2002, 2005b).

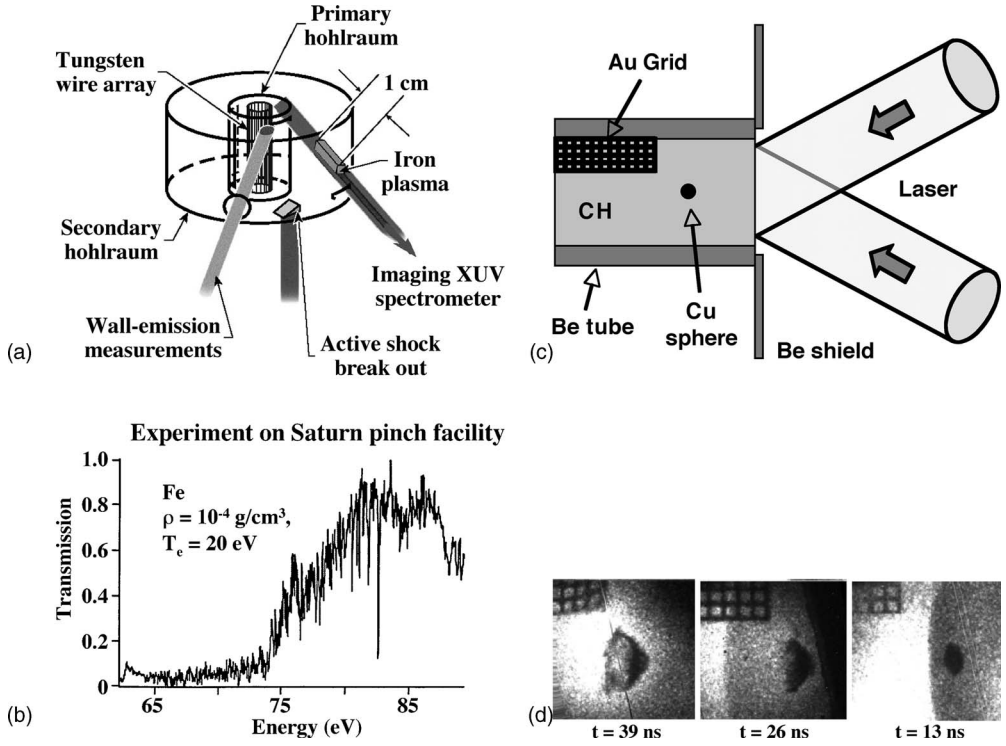

FIG. 2. Examples of laboratory astrophysics experiments done on high power lasers and *Z*-pinch facilities. (a) Opacity experiment using a *Z*-pinch driven hohlraum on the Saturn facility. The *Z* pinch implodes on the axis of a primary hohlraum which is used as a source of a thermal x-ray radiation for probing an iron plasma and measuring its opacity under conditions relevant to the physics of Cepheid variable stars. Adapted from Springer *et al.*, 1997. (b) Measurement of the Fe sample transmission spectrum from the experiment sketched in (a). Adapted from Springer *et al.*, 1997. (c) Typical hydrodynamics experiment using direct laser irradiation. In this case, the experiment (Robey *et al.*, 2002) is to study the interaction of a strong shock with a density clump, which is a typical astrophysical problem (Klein *et al.*, 2003). Several of the Omega beams are used to generate a source of x rays (a backlighter, see text) situated at the opposite side of the experimental assembly. (d) Using a gated x-ray pinhole camera ("x-ray framing camera"), radiographic images are obtained as a function of time showing the evolution of the shocked sphere. Adapted from Robey *et al.*, 2002.

In addition to *Z* pinches, it has been demonstrated that pulsed power devices can use $\mathbf{J}\times\mathbf{B}$ forces to accelerate flyer plates. Specifically, the *Z* machine has accelerated 9-mm-square, 0.35-mm-thick plates of Al to velocities above 20 km/s (Knudson *et al.*, 2001, 2003). Used as flyer plates, this permits equation of state experiments at pressures above a Mbar (10^{12} dynes/cm^2), which, together with work done on lasers, is directly relevant to the interiors of gas giant planets.

D. Astrophysics experiments

The experiments discussed in this article typically use one of two basic methods. In "hohlraum" experiments, known in inertial fusion as "indirect drive," a number of laser beams are used to irradiate the inner surface of a cavity made with a high-*Z* material; beams penetrate the cavity through several (small) holes. This is a hohlraum. Energies of tens of kJ can heat few-mm-scale hohlraums to temperatures of kT=100–200 eV. The experimental package may be located inside the hohlraum, to locate a sample within a uniform x-ray environment, outside the hohlraum, to control the orientation of the x-ray flux to it, or on the side of the hohlraum, to produce planar acceleration of the package. Many such experiments begin with the use of ablation by soft x rays the hohlraum contains, in order to create a pressure that drives a shock wave into some material. Other experiments are designed so that x rays in the hohlraum penetrate and heat the material to be studied.

The hohlraum geometry can also be created in the *Z*-pinch diode. In this case, the fast pinch is formed on the axis of the hohlraum. The experimental package can be situated either inside the hohlraum or on its surface; secondary hohlraums can also be used (see Sec. VIII.B in Ryutov, Derzon, and Matzen, 2000). An experiment using a *Z*-pinch driven primary plus secondary hohlraum is shown in Fig. 2(a). This experiment, which is discussed further in Sec. III, measured the opacity of iron under conditions relevant to stellar envelopes, and was directly relevant to reducing uncertainties in the models of pulsating stars, the so-called Cepheid variables (Rogers and Iglesias, 1994; Springer *et al.*, 1997). The *Z* pinch at the Saturn pulsed power facility at SNLA drove concentric primary and secondary cylindrical hohlraums. An iron sample placed in the secondary hohlraum was heated to equilibrium temperatures of ~20 eV at a density of $\sim 10^{-4}$ g/cm^3. Using a high-resolution, transmission grat-

ing spectrometer, the transmission of broad-band x rays, from the Planckian hohlraum radiation field, through the sample was spectrally recorded, which allowed the opacity of Fe to be determined with high spectral resolution as shown in Fig. 2(b). This data set was used to test models of the opacity of Fe under stellar envelope conditions.

The other typical setting is a so-called "direct drive" setting, used on high intensity lasers (not on Z pinches), where laser beams are focused directly onto the experimental target. Figures 2(c) and 2(d) illustrate such an experiment at the Omega laser. The Omega system was built to study direct drive laser fusion, in which laser beams directly strike a capsule, causing it to implode and produce fusion. This explains the large number of beams (60) and their even distribution (Fig. 1). On Omega, a planar shock can be launched using at most 12 (of the 60) beams. In this case the ablation by the laser irradiation creates the pressure that launches the shock to initiate the experiment. The experiment shown in Fig. 2(c) shows a ~120-μm-diameter solid Cu sphere embedded in a solid plastic (CH) cylinder (Klein *et al.*, 2000, 2003; Robey *et al.*, 2002). The laser drive launches a strong shock down the CH ($\rho \sim 1$ g/cm^3), which has decayed to $P_{\mathrm{shk}} \sim 12$ Mbar by the time it reaches the location of the Cu sphere. Upon passage through the Cu sphere, the shock compresses it, and induces vortical flow, morphologically similar to a smoke ring. The evolution of this shock-sphere dynamics is captured in a sequence of side-on x-ray shadowgraph images (radiographs) shown in Fig. 2(d). The gold spatial resolution grid shown in the upper left-hand corner of the images has a grid spacing of 63.5 μm, and is used to simultaneously measure magnification and spatial resolution of the x-ray imaging camera used. This experiment is discussed in more detail in Sec. V.

In many experiments, whether hohlraums or direct laser irradiation are used, additional laser beams produce x rays for diagnostic purposes. In fact, one often uses more laser beams for this purpose than to drive the experiment. Some of the beams may be used to irradiate a small spot on a material plate, situated behind the experimental package and known as a backlighter. Under laser irradiation, this plate produces energetic x rays, typically in an emission line or band. The x-ray energy is chosen so that components or structures in the target selectively absorb these x rays. When they are imaged onto a detector, the result is a radiograph of the target [Fig. 2(d)] not unlike the chest x ray a doctor may request. In addition, these diagnostic x rays can also be used for absorption spectroscopy or for time-resolved measurements. We describe below the results from a wide variety of experiments utilizing similar techniques as those illustrated in Fig. 2. The specific configuration and diagnostic details of each individual experiment presented will not be discussed in any depth, to allow a wider selection of results to be shown. Details for each specific experiment can be found in the references.

III. OPACITIES AND CEPHEID VARIABLES

Understanding the evolution of stars from birth to death forms one of the fundamental challenges facing astronomers and astrophysicists. A star begins from an initial "rapid" (several $\times 10^6$ yrs) gravitational collapse of a dense clump in a molecular cloud, in a region where the Jeans' (gravitational) instability dominates other dynamics [e.g., $\tau_{\mathrm{Jeans}} = (4\pi G\rho)^{1/2} <$ other dynamic time scales in the cloud; here G is the gravitational constant and ρ is the mass density]. If the mass of the star exceeds about $0.1 M_{\mathrm{Sun}}$, the central temperature and density reach the point where thermonuclear fusion of hydrogen into helium becomes the dominant energy source. At this point, the star settles into its main sequence phase in the Hertzsprung-Russell (HR) diagram, that is, a plot of luminosity versus temperature or, equivalently, magnitude versus spectral type (Bohm-Vitense, 1989a; Hansen and Kawaler, 1995). When approximately 10% of a star's original hydrogen is converted to helium, hydrogen depletion in the core starts to become significant. At this point, the delicate balance between core-generated thermal pressure due to nuclear burning and the inwardly directed gravitational force is perturbed, upsetting the condition of hydrostatic equilibrium, and the core starts to contract. This contraction increases the temperature and density to the point where helium burning begins, leading to a corresponding rise in the energy generation rate and luminosity. The star enters its "blue-loop" phase (Bohm-Vitense, 1989b).

If the star is sufficiently massive, $M \geq 5 M_{\mathrm{Sun}}$, its blue loop excursion is sufficiently large that its path on the HR diagram crosses and, more importantly, lingers in the Cepheid instability strip shown in Fig. 3(a) (Bohm-Vitense, 1989a). In this phase, an interesting global dynamics can occur, namely, stellar pulsation. All stars in this strip are observed to pulsate, with luminosities varying by factors of up to 2 or 3 over periods of days to weeks. The classical Cepheids refer to the δ Cephei supergiant stars, which are the brightest in this class of variable stars. Several other classes of stars also fall into the Cepheid instability strip and are variable, such as the RR Lyrae, δ Scuti, and W Virginis variables. Understanding the mechanisms underlying such stellar pulsations has been an ongoing challenge in astrophysics.

A remarkable feature of Cepheid variable stars is that their pulsation periods P are proportional to their average luminosities as shown in Fig. 3(b) (Bohm-Vitense, 1989a). Stellar pulsations result from a driven resonant standing compression wave of the star. Bigger stars are more luminous and, by virtue of their larger size, will have longer periods of pulsation. This relationship can be expressed as

$$P = \frac{Q}{(\bar{\rho}/\bar{\rho}_{\mathrm{Sun}})^{1/2}}, \tag{3.1}$$

where Q is a constant, $\bar{\rho}$ is the average density of the pulsating star, and $\bar{\rho}_{\mathrm{Sun}}$ is the average density of the sun $\bar{\rho}_{\mathrm{Sun}} \approx 1.4$ g/cm^3. For a given mass, (spatially) larger stars

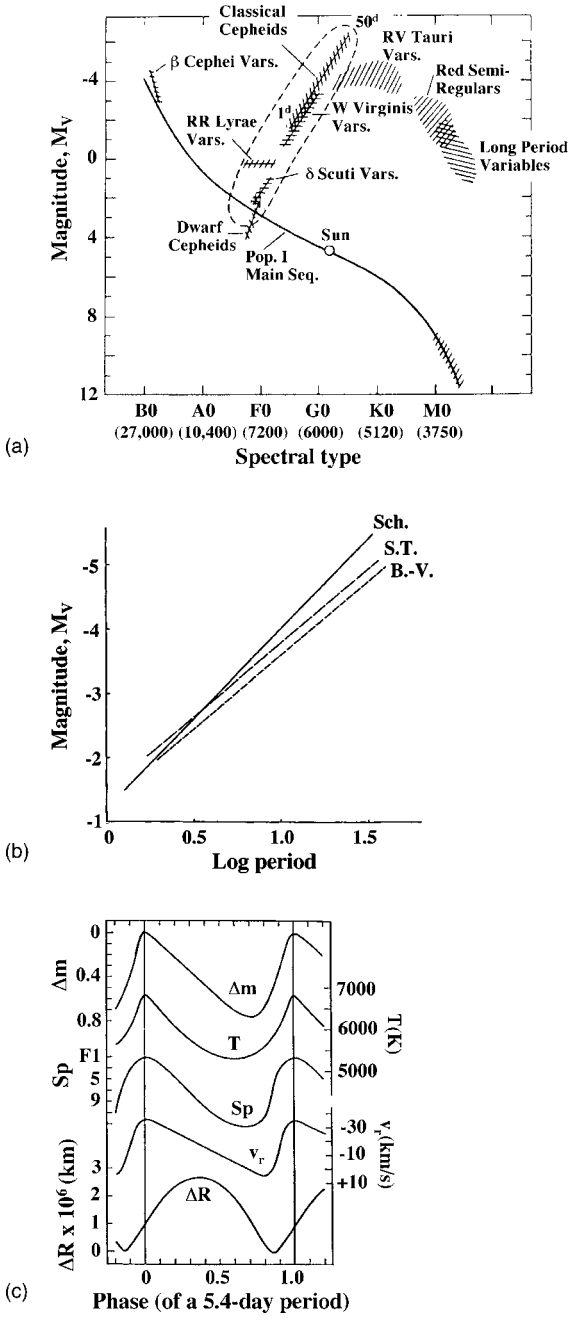

FIG. 3. Cepheid variable stars offer a useful "galactic yardstick," based on their pulsation dynamics. (a) Hertzsprung-Russell diagram of magnitude versus spectral type for stars along the main sequence, and variable stars, including those along the Cepheid instability strip. Also shown along the horizontal axis are temperatures (K) in parentheses, and their corresponding spectral types. Adapted from Bohm-Vitense, 1989a. (b) Plots of the stellar pulsation period–magnitude (or luminosity) linear relation, showing that the longer the period of oscillation, the brighter the star (lower magnitude). The three curves result from different analyses of this correlation. These curves form the basis for the use of Cepheid variables as galactic yardsticks, to infer distances. Adapted from Bohm-Vitense, 1989a. (c) The phase relations for the variable star δ Cephei, showing the correlations between periodic pulsations of visual magnitude (Δm), i.e., brightness, effective temperature (T), spectral type (Sp), radial velocity (v_r), and radius (ΔR). Adapted from Bohm-Vitense, 1989a.

are more luminous, have lower average densities, and longer periods of oscillation, hence the luminosity-period correlation.

The criteria to set up a global standing wave in a star is based on hitting a resonance between a driving force and one or several normal modes of oscillation (pulsation) in the star. Consider first a fictitious adiabatic star (Bohm-Vitense, 1989b), and assume a small pulsation randomly began, say, near to the convection layer. At peak compression, the temperature would be maximum due to the $P \cdot dV$ work done on the star by gravity. At peak expansion, the temperature would be minimum due to the $P \cdot dV$ work done by the star on itself during expansion. The radially outward velocity would be maximum at the equilibrium radius as the star was expanding outwards. If the star were truly adiabatic, this pulsation would continue forever, never growing (or decreasing) in amplitude. This would definitely not lead to the large global pulsations of ~20% in radius characteristic of Cepheid variable stars. To generate a global pulsation requires a resonant driving force, a condition that can result from a nonadiabatic heat flow. Similar to pushing a swing at its resonance frequency, as the star leaves peak compression and moves into its expansion phase, e.g., near the point of peak outward velocity, there needs to be a slightly increased outward push. This can be due, in this case, to a higher interior temperature and, hence, higher pressure. This added outward push, in phase with the oscillation, causes the pulsation amplitude to increase, leading to a variable star. The resulting phase relations are shown in Fig. 3(c) for a δ Cephei star, showing periodic oscillations of magnitude, temperature, spectral type, radial velocity, and radius. Notice that the radial velocity peaks in phase with temperature, which is proportional to pressure, and which occurs just after the star leaves peak compression ($\Delta R = 0$) and starts to expand.

Opacity plays a key role in causing this resonant temperature enhancement. For a solar mixture of H, He, and "metals" ($Z \geq 3$), the Rosseland mean opacity κ_R is shown as a function of temperature T for a constant value of ρ / T^3 (where ρ corresponds to density) in Fig. 4(a) (Rogers and Iglesias, 1994). There are bumps or broad peaks in the average opacity as temperature is increased, corresponding to thermal energies sufficient to excite or ionize H, He, and higher-Z metals through their various electron shells. On the rising side of one of these bumps (sometimes called "κ mountains"), resonant conditions can occur in the heat flow that can lead to stellar pulsations. As the star contracts, the temperature rises increasing the opacity, which allows less radiative heat from the core to leak out, raising the temperature and pressure even further. This leads to a slightly enhanced outward push as the star starts its outward movement, in resonance with the oscillatory motion of the star. Near peak expansion, the temperature drops due to the work done by the star on itself. This lowers the opacity, allowing more radiative heat to leak out, dropping the interior pressure, allowing the star to contract more strongly. The result is that in this resonant

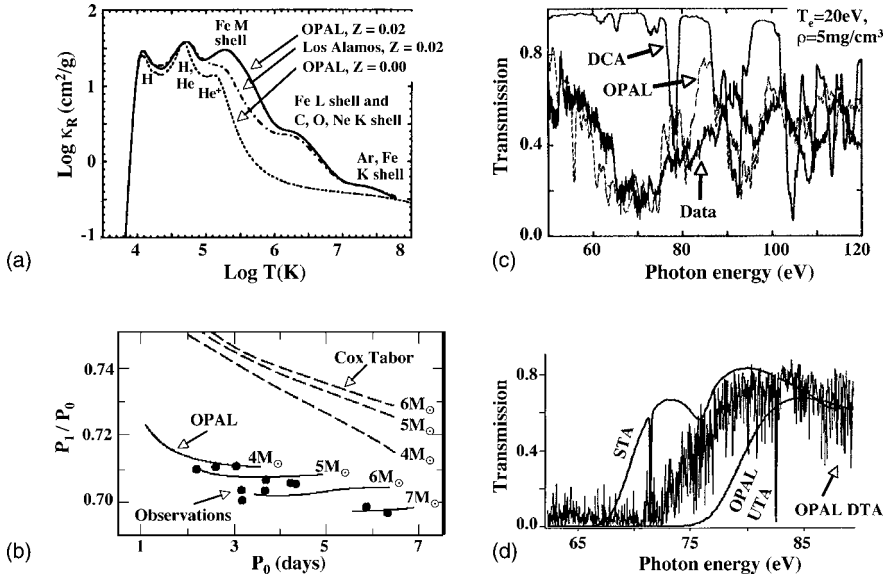

FIG. 4. Modern opacity simulations, tested against experiments, have improved our understanding of cepheid variable star pulsation. (a) Opacity versus temperature for a 15-element mixture of solar composition, along a path of constant ρ/T^3. OPAL calculations are shown for a zero metallicity star (no elements heavier than He, and denoted "$Z=0$"), and for a $Z=0.02$ solar metallicity star (2% mass fraction in elements heavier than He). Results from a previously used set of Los Alamos opacities for $Z=0.02$ are also shown. Adapted from Rogers and Iglesias, 1994. (b) Diagram of the ratio of the first two harmonics periods of a beat Cepheid variable star. Circles represent observations. The upper set of three (dashed) curves correspond to the simulated result using older opacities, which ignore the full fine structure of the metals. The lower (solid) curves correspond to simulations with OPAL-DTA, including the full fine structure, in particular, for Fe. Adapted from Rogers and Iglesias, 1994. (c) Plot showing measured versus calculated transmission through a thin Fe sample heated to conditions of $T\approx 20$ eV and $\rho\approx 5$ mg/cm^3. Two OPAL opacity simulations are shown, one using DCA with hydrogenic oscillator strengths, which ignores term splitting (top curve), and the other using full DTA with intermediate coupling, which causes term splitting. The latter, more complete opacity calculation more closely reproduces experimental results. Experiments were carried out on the Nova laser. Adapted from Rogers and Iglesias, 1994. (d) Comparison of theoretical Fe transmission spectra at the measured conditions of $T\approx 20$ eV, and $\rho\approx 10^{-4}$ g/cm^3. The calculations correspond to the STA opacity model (upper curve), OPAL-DTA model (intermediate curve, showing the line fine structure), and OPAL-UTA (lower curve). The intermediate curve closely reproduces experimental results [shown in Fig 2(b)]. Including the transition fine structure changes the predicted average opacities significantly. Adapted from Springer *et al.*, 1997.

condition the amplitude of global oscillation increases leading to a pulsating star. These pulsations do not increase in amplitude indefinitely, however. Once the pulsation amplitudes become large enough that the heating during compression takes the opacity over the top of the κ mountain, the opacity drops on compression, allowing radiation to leak out, and serving as a damping mechanism.

There is an intimate connection between stellar pulsation period and opacity. Global oscillations are standing sound (compression) waves in the star, so the period must be proportional to the ratio of star diameter to average sound speed. But sound speed varies with temperature as $T^{1/2}$. Since a higher stellar opacity holds in heat by inhibiting radiative heat losses, temperature is a monotonically increasing function of opacity. The result is that an increased stellar opacity leads to a shorter period of pulsation. This is summarized by writing the following approximate relation for stellar oscillation period:

$$P \propto \frac{D_{\rm star}}{c_s} \propto \frac{D_{\rm star}}{T^{1/2}} \propto \frac{D_{\rm star}}{\kappa^{n/2}}, \tag{3.2}$$

where $D_{\rm star}$ and c_s correspond to the stellar diameter and average sound speed. For simplicity, we have assumed, over a small enough interval of temperature on the rising side of the bump, that $\kappa \sim T^{\rm m}$ and $n=1/m$. This period-opacity relation is portrayed rather dramatically in a plot of the period of oscillation of the second harmonic (P_1) versus the period of the fundamental mode (P_0) for beat Cepheids shown in Fig. 4(b). Using older opacities, which did not include all relevant transitions for metals, in particular Fe, the calculated opacities were too low and the calculated pulsation periods were too large (Cox and Tabor, 1976). When a more complete accounting of the Fe opacities was taken in the opacity code OPAL (Iglesias and Rogers, 1991; Rogers and Iglesias, 1992) the calculated periods for the beat Cepheids were brought into much better agreement with observations as shown in Fig. 4(b).

Opacity calculations are enormously complex, especially for higher-Z materials ($Z>$ several). The OPAL calculations have been improved by comparison with experiments under a variety of conditions, as shown in Figs. 4(c) and 4(d). In one of the first Fe opacity measurements, done on the Nova laser, one laser beam with a wavelength of 0.53 μm was used to heat a 250-nm-thick Au foil by direct irradiation with a square 1-ns pulse of 3.3 kJ (Da Silva *et al.*, 1992; Springer *et al.*,

1992). The x-ray flux thus generated volumetrically heated and expanded a 20-nm sample of Fe to a temperature of ~20 eV at densities of ~5 mg/cm^3. A second laser beam with a 2-ns square pulse of 0.53-μm light irradiated a second Au foil, generating backlighter x rays whose transmission through the sample was measured with a time-resolved ("streaked") extreme ultraviolet spectrometer. The measured Fe transmission spectrum, shown in Fig. 4(c), showed a dominant absorption feature centered at 70 eV corresponding to an important $\Delta n=0$ ($n=3$ to $n=3$) transition, overlooked in previous opacity calculations, such as that shown by the upper curve corresponding to a detailed configuration accounting (DCA) calculation (Cox and Tabor, 1976; Rogers and Iglesias, 1994). The newer DTA (detailed term accounting) calculations using the OPAL opacity code, including term splitting (Iglesias and Rogers, 1991; Rogers and Iglesias, 1992) reproduce this feature quite well. Transitions such as this, missing in previous opacity calculations, lead to the enhanced opacities in the models of beat Cepheid variables that allow the models to more closely reproduce the observed pulsation frequencies as shown in Fig. 4(b).

Opacity models differ more significantly at lower densities $\rho<1$ mg/cm^3, where density-induced line broadening and smearing is lower. Under these conditions, "forests" of fine-structure transitions can be resolved experimentally. The time scales to achieve steady-state, local thermodynamic equilibrium (LTE) conditions at lower densities, however, is longer. In this regime, large Z-pinch facilities offer a more attractive setting for such opacity measurements. Their characteristic time and spatial scales are longer. An example of a key opacity experiment done on Fe on the Saturn Z-pinch facility is shown in Figs. 2(b) and 4(d) (Springer *et al.*, 1997) and briefly described in Sec. II. The obtained transmission spectrum of this Fe sample ($\rho=10^{-4}$ g/cm^3) was then compared with predictions of various LTE opacity models, as shown in Fig. 4(d). The supertransition array (STA) model (Bar-Shalom *et al.*, 1989), which averages over large groups of configurations, overpredicts the transmission data in this regime, whereas the unresolved transition array (UTA) model (Iglesias and Wilson, 1994) underpredicts the data. The OPAL calculation (Iglesias and Rogers, 1991; Rogers and Iglesias, 1992), which captures the complex arrays of fine-structure absorption lines, falls in between in the figure and is in much better agreement with the data [shown in Fig. 2(b)]. Experimental measurements such as those shown in Figs. 4(c) and 2(b) are indispensable in refining and "calibrating" sophisticated opacity models such as OPAL.

IV. HYDRODYNAMICS OF CORE-COLLAPSE SUPERNOVAE

A. Introduction

A core-collapse supernova (SN) marks the explosive death of a massive star. Supernovae (SNe) involve a very broad range of physical processes. Their description requires the coupling of disparate areas of science, such as nuclear physics, general relativity, hydrodynamic stability, and turbulence. To make things even more complex, there are several types of SNe with different mechanisms of energy release.

The kinetic energy release in a typical SN event is ~10^{51} ergs, but only a few percent of this amount is emitted as visible light. Still, supernovae are sometimes brighter than their entire host galaxy. The light as detected by optical telescopes comes not from the core of the exploding star, where the energy release has occurred, but rather from a photosphere, to which the energy is transported by a complex combination of hydrodynamic flows and radiative transport. In linking the energy release in the SN core with the visible light curve, a correct description of the transport of material and radiation is very important. Opacity models in particular are critical to modeling radiation transport. In this area, laboratory experiments are making significant contributions by providing direct measurements under the conditions relevant to a real problem.

A nice description of SN phenomenology, as well as existing theories of their formation, can be found, e.g., in the book by Arnett (1996). Other papers of general interest include Bethe (1990), Woosley (1990), and Woosley and Eastman (1997). Some more recent surveys can be found in "Cosmic Explosions" (Proceedings of the 10th Astrophysical Conference, College Park, Maryland, 1999, AIP Conference Proceedings No. 522).

Supernovae are believed to explode by two fundamental mechanisms: collapse of the core (in large stars) and thermonuclear explosion (in small stars below eight solar masses at birth). Classification by types is based on spectra and is too involved to discuss here. We will focus on only core-collapse SNe (type II) and thermonuclear SNe (type Ia). Type-II SNe are thought to occur as the result of a gravitational collapse and neutronization of the iron core of the star; their formation is accompanied by generation of a short but very intense burst of neutrinos (carrying away some 99% of the released energy). Neutrinos form a blast wave near the center of the progenitor star, which ultimately, and by a mechanism still not fully understood, blows it apart and gives rise to a tremendous increase of luminosity. The collapsed core forms a neutron star that might later be detected as a pulsar. Experiments discussed in Secs. IV.C–IV.E are relevant to type-II SNe.

Type-Ia SNe are believed to be caused by a thermonuclear burn of carbon-oxygen white dwarfs. One of the key problems in the physics of this system is the propagation of the nuclear "flame" from the ignition point, specifically, the stability of the flame, and the transition from a subsonic burn (deflagration) to a supersonic detonation. There is a significant amount of information on these issues obtained in experiments on the propagation of chemical flames, summarized in particular by Williams (1985), with more recent work involving Khokhlov and others reviewed by Drake (1999). In the present experiments using current high-power lasers it is hard to expect that conditions for a thermonuclear burn of a DT

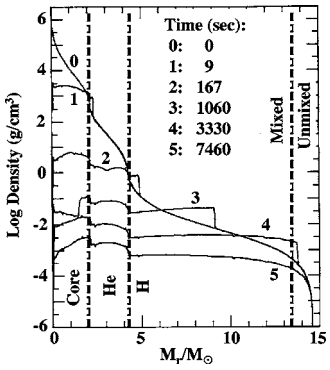

FIG. 5. Variation of the density distribution after the explosion of SN 1987A. (Shigeyama and Nomoto, 1990). Time $t=0$ corresponds to the instant just before the explosion. M_r is a Lagrangian mass within a certain radius. Steep density gradients in the progenitor star situated at $M_r/M_\odot \approx 2.5$ and $M_r/M_\odot \approx 4$ correspond to the oxygen (labeled "core") -helium and helium-hydrogen transition zones, respectively. After the transit of the shock wave through these zones, the pressure gradient changes sign and the Rayleigh-Taylor instability develops leading to a 3D mixing process which is thought to be important in the explanation of the light curve. The vertical dashed line at $M_r/M_\odot \approx 13.5$ indicates the location out to which core ^{56}Co has to be pre-mixed for 1D simulations of SN1987A to reproduce light curve observations. This large degree of mixing, which has been difficult to reproduce with large-scale simulations, is referred to here as the "SN mix problem." Adapted from Shigeyama and Nomoto, 1990.

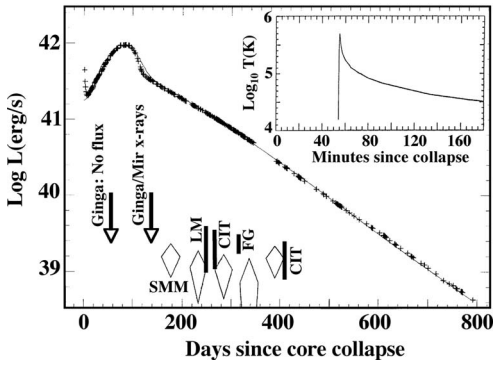

FIG. 6. Light curve for SN1987A. The "+" symbols are the observed light curve, and the thin solid line is an analytic model described by Arnett (1996). Different dates indicated show when x rays were first detected on day 139 by the Ginga/Mir experiment, when γ rays from ^{56}Co were detected by the Solar Maximum Mission (SMM) at day 178, and when subsequent detections of γ rays occurred by several balloon experiments (CIT, LM, FG). Inset: A calculation of the evolution of temperature versus time as the shock breaks out from the surface of the star. Adapted from Arnett, 1996

mixture and propagation of ignition from the hot spot can be reached. Perhaps such conditions will be reached with the NIF and Megajoule facilities that are now under construction (see Secs. II and X). Type-Ia SNe, used to measure the distances to high-redshift galaxies, provide the essential data supporting the present conclusion that the expansion of the Universe is accelerating (Kirshner, 1999; Perlmutter *et al.*, 1999).

From the broad array of problems related to our understanding of SN explosions, we shall concentrate on the laboratory simulation of hydrodynamic phenomena in the type-II SN explosions. We choose this subset because, on the one hand, multidimensional hydrodynamic effects are thought to be very important (see Sec. IV.B for more detail) and, on the other hand, there already exist successful experiments of this type related to the shock breakout through the He-H interface. In addition, the analysis of the scalability and other constraints can be nicely illustrated; this example can serve as a template for similar analyses of other problems.

B. Multidimensional hydrodynamics in core-collapse supernovae

It is believed that the progenitor star, just before the SN explosion, had a layered ("onion-skin") structure, with the dense core surrounded by layers of helium and hydrogen (Fig. 5 from Shigeyama and Nomoto, 1990). When the core collapses, an outward propagating shock is launched by the "core bounce" process. When this shock reaches the surface of the star, after an interval of ~1 h, the star lights up in a burst of luminosity, and the optical SN has begun. The observed light curve for the most famous recent supernova in a Large Magellanic Cloud, SN 1987a, is shown in Fig. 6, and the inset shows temperature versus time at the surface of the star at and following shock break out (Arnett, 1996).

Theoretical analyses have shown that it is impossible to explain the explosion of SN type II without taking into account two-dimensional (2D) and 3D hydrodynamic effects. The energy deposition by neutrinos in the zone surrounding the collapsing core is insufficient, in a spherically symmetric case, to drive the explosion of the star's outer layers. Certainly, some complex nonspherically symmetric motions must be involved, and only their inclusion (in a phenomenological manner) by Bethe and Wilson (1985) allowed creating a plausible model for supernova explosions.

Another problem where 3D dynamics are important is the postshock mixing of the star's inner parts, mainly heavy core elements, outwards into the overlying envelope of hydrogen and helium. The observed early appearance of heavy elements, such as ^{56}Ni and ^{56}Co, in the photosphere of SN 1987A [see Sutherland (1990), and references therein] is incompatible with the spherically symmetric expansion; significant effort has been spent on developing a mixing theory based on the Rayleigh-Taylor (RT) instability (Arnett, 1988; Arnett *et al.*, 1989). To illustrate the magnitude of mixing required to explain the observations, we show a vertical dashed curve at $M_r/M_\odot = 13.4$ in Fig. 5 (Shigeyama and Nomoto, 1990). This corresponds to the location to which ^{56}Co had to be premixed (which is nearly the entire progenitor star) so that a 1D explosion simulation reproduced the observed light curve for SN1987A. Figure 7 (Kifonides *et al.*, 2000, 2003) illustrates the spikes produced

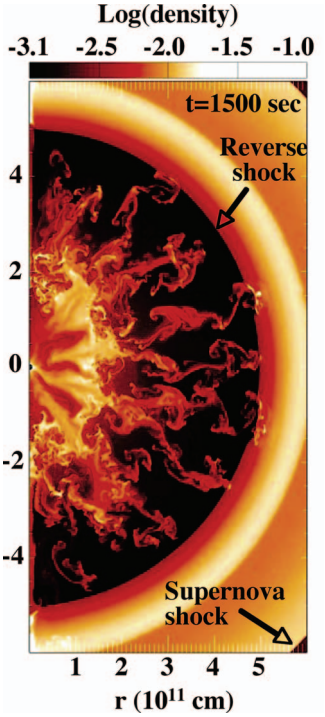

FIG. 7. (Color) Density distribution (log ρ[g/cm^3]) 1500 s after core bounce. The supernova shock (outermost discontinuity) is located at $r \approx 9\times10^{11}$ cm. A dense shell (visible as a whitish ring) has formed between the SN shock and reverse shock at $r \sim 5\times10^{11}$ cm, with its outer boundary coinciding with the He/H interface. The fastest moving RT spikes have just reached the reverse shock. Adapted from Kifonidis *et al.*, 2003.

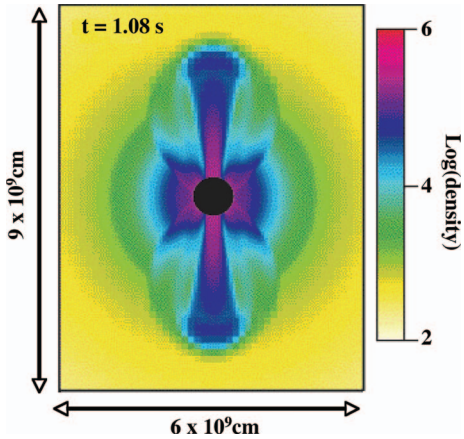

FIG. 8. (Color) Jet-induced explosion. Frames show the density in the x-z plane passing through the center of computational domain, at 1.08 s after the jet initiation. The jet axis (and presumably the rotation axis) is vertical here. The size of the panel is 9×10^9 cm vertically and 6×10^9 cm horizontally. Adapted from Khokhlov *et al.*, 1999.

in the strongly nonlinear stage of the RT instability. The RT spikes have just encountered the reverse shock and slowed down abruptly. A principal motivation of the experiments discussed below is that multidimensional simulations of the RT instability had failed to explain the observations. We call this here the "SN mix problem." Two possibilities follow: the simulations might be in error or other physics might be responsible for the observations. Well-scaled experiments have shown, however, that the simulations are probably correct with regard to the large-scale RT behavior.

Experiments have also led to the realization that hydrodynamic turbulence might affect the behavior of SNe in ways the simulations cannot reproduce. This is one example of other physics with the potential to affect the observed quantities. Experiments now underway are addressing this possibility. Another example of other physics is provided by spectropolarimetric studies, which allow an evaluation of the asphericity of an object. These have shown that between two weeks and two months after the explosion most SNe manifest gross deviations from spherical symmetry (Jeffery 1991; Trammell *et al.*, 1993; Tran *et al.*, 1997; Leonard *et al.*, 2000; Wang *et al.*, 2002). These observations are consistent with the suggestion that the collapse of a rotating, magnetized stellar core might produce bipolar jets that would perforate the outer layers and quickly reach the photosphere, thereby providing one more explanation for the early arrival of heavy elements to the photosphere (Fryer, 1999). A strong enough magnetic field breaks the spherical symmetry and may generate magnetohydrodynamics instabilities that are typically three-dimensional and might produce such jets (LeBlanc and Wilson, 1970; Spruit, 1999; Fryer and Heger, 2000; Wheeler *et al.*, 2000). This motivated a recent set of hydrodynamic calculations of jet-driven SNe explosions by Khokhlov *et al.* (1999); Fig. 8 shows one of their results. Scaled hydrodynamic experiments relevant to this model are also now underway.

The importance of nonspherically symmetric hydrodynamics is also shown by the fact that neutron stars usually received a strong "kick" during the explosion that creates them (Cordes *et al.*, 1993; Lyne and Lorimer, 1994). This seems to imply that there are significant gross asymmetries at an early stage of the implosion which are enhanced in the course of the implosion (Burrows and Hayes, 1996; Fryer *et al.*, 1998; Scheck *et al.*, 2004). In addition, relatively little is known about effects of rotation in the core-collapse process. The angular velocity of a progenitor varies both in radius and in the azimuthal angle. The velocity shear will grow during the implosion causing the development of shear-flow turbulence, whose effect on the mix during the implosion may be an important factor (Heger *et al.*, 2000).

An interesting new 2D computational study (Kifonidis *et al.*, 2006) offers a different approach to breaking the spherical symmetry of the explosion. Lowering the neutrino luminosity but extending its duration and reducing its decay rate during the first second of the explosion allows hydrodynamic instabilities (advective-acoustic instability) in the neutrino heated postshock layers to grow to sufficient strength in low-order modes to deform the shock. This perturbed inner ejecta and shock allow the highest velocity metal clumps to exit the He layer prior to the formation of the reverse shock at the He-H "interface," and their velocities remain high. The interaction of the perturbed shock with the He-H inter-

face induces the Richtmyer-Meshkov instability, which in turn leads to a deeper mixing of hydrogen into the core at late times. These 2D simulation results are much more consistent with the observations of SN1987A that previous results from this group (Kifonidis *et al.*, 2000, 2003). Their results draw attention to the importance of capturing early-time, low-order modes and the mutual interaction of multiple stages of hydrodynamic instabilities from the core to the envelope. In the lexicon of HED laboratory experiments this would be called an "integrated simulation." Recent (Drake, Leibrandt, *et al.*, 2004) and continuing experiments have been addressing the role of low-order modes in mixing. Attacking the more complex problem with divergence and multiple interfaces should become viable on the National Ignition Facility.

In summary, there are several complex and still unresolved hydrodynamic problems which have a deep impact on our understanding of the supernovae starting from the central question of why they explode at all. A concerted attack on these problems, including scaled laboratory experiments, is both necessary and possible.

C. A sample problem: Shock wave breakout through the He-H interface

We use the problem of shock wave breakout through the He-H interface for designing scaled laboratory experiments. This example allows one to clearly identify the most important steps in developing scaled laboratory experiment. These steps (which will be described in more detail in the following subsections) are (i) ensure that a hydrodynamic description is adequate, (ii) evaluate the role of transport processes (such as heat conduction), (iii) determine the equation of state, (iv) characterize initial conditions, and (v) consider whether some simplification in geometry is possible (e.g., can some time interval of evolution of a planar system adequately describe the evolution of a spherically divergent system).

As a representative set of plasma parameters in the He-H transition region (Table I), we have chosen a set of parameters based on the work of Müller *et al.* (1991). In Table I, L is the density gradient scale length, v is the characteristic velocity, T is the plasma temperature (the electron and ion temperatures are equal), and ρ is the plasma density. The blast wave that blows the star apart first accelerates and then decelerates the transition region. During the deceleration the pressure gradient is still outward. Because this opposes the inward density gradient, the transitional zone is RT unstable. The characteristic acceleration experienced by a given fluid element upon arrival of the blast wave can be estimated as v/τ, with $\tau \sim L/v$, to be $v^2/L \sim 2.5\times10^5$ cm/s^2 (Ryutov *et al.*, 1999). The gravitational acceleration is orders of magnitude smaller and is also negligible in the laboratory experiment to be discussed. The representative parameters of the first laboratory experiment simulating the He-H interface instability (Remington *et al.*, 1997) are listed in the right-hand column of Table I.

TABLE I. Comparing characteristic parameters of a SN 1987a plasma in the He-H transition layer ($t\sim2000$ s) and of a laboratory experiment at $t=20$ ns since the onset of the radiation drive.

Parameter	SN 1987a	Laboratory experiment
L (cm)	9×10^{10}	5.3×10^{-3}
v (cm/s)[a]	2×10^{7}	1.3×10^{5}
ρ (g/cm^3)	7.5×10^{-3}	4.2
p (dyn/cm^2)	3.5×10^{13}	6×10^{11}
Eu[b]	0.29	0.34
Re	2.6×10^{10}	1.9×10^{6}
Pe	2.6×10^{5}	1.8×10^{3}

[a]The velocity in this table is defined as the rate of broadening of the density peak [Figs. 9(a) and 9(b)], not the interface velocity [Fig. 9(c)].
[b]Eu is the Euler number, $\mathrm{Eu}=v(\rho/p)^{1/2}$.

We will now quickly go through the five questions formulated at the beginning to this section. As was shown by Ryutov *et al.* (1999), the hydrodynamic description applies to both systems, although in the case of a supernova the pressure is dominated by radiation, whereas in the laboratory experiment it is dominated by the gaseous pressure. The viscosity and thermal conductivity are small (i.e., the Reynolds and Peclet numbers are large). Under such circumstances, both systems can be adequately described by the Euler equations (e.g., Landau and Lifshitz, 1987).

The dominance of the radiation pressure in the case of the supernova means that the equation of state is that for the ideal gas with the adiabatic index $\gamma=4/3$. It is desirable that the medium used in the laboratory experiment have equations of state deviating not too strongly from that for the polytropic gas with $\gamma=4/3$. Even if some deviations are present, however, one should not expect the appearance of any dramatic differences, because the Euler equations are structurally stable with respect to variations of γ.

Setting up appropriate initial conditions for 2D and 3D simulations of the dynamics at or near an "interface" usually starts with a set of 1D simulations, which determine the overall profiles for density, temperature, velocity, and other relevant quantities. There exist numerous simulations describing the propagation of the shock through the He-H interface [see, e.g., Müller *et al.* (1991) and Kane *et al.* (2000)]. In their 1D versions, all are quite reliable and all present a similar picture of the main hydrodynamic parameters that are needed as a starting point for studying the 2D and 3D hydrodynamics. An example of the density and pressure profiles is shown in Fig. 9(a).

In the laboratory experiment, the experimental package is driven by the ablation pressure produced by the absorption of the intense radiation on one of the package sides. Changing the shape and power of the laser pulse allows a certain degree of control over the time dependence of the ablation pressure. The temporal evo-

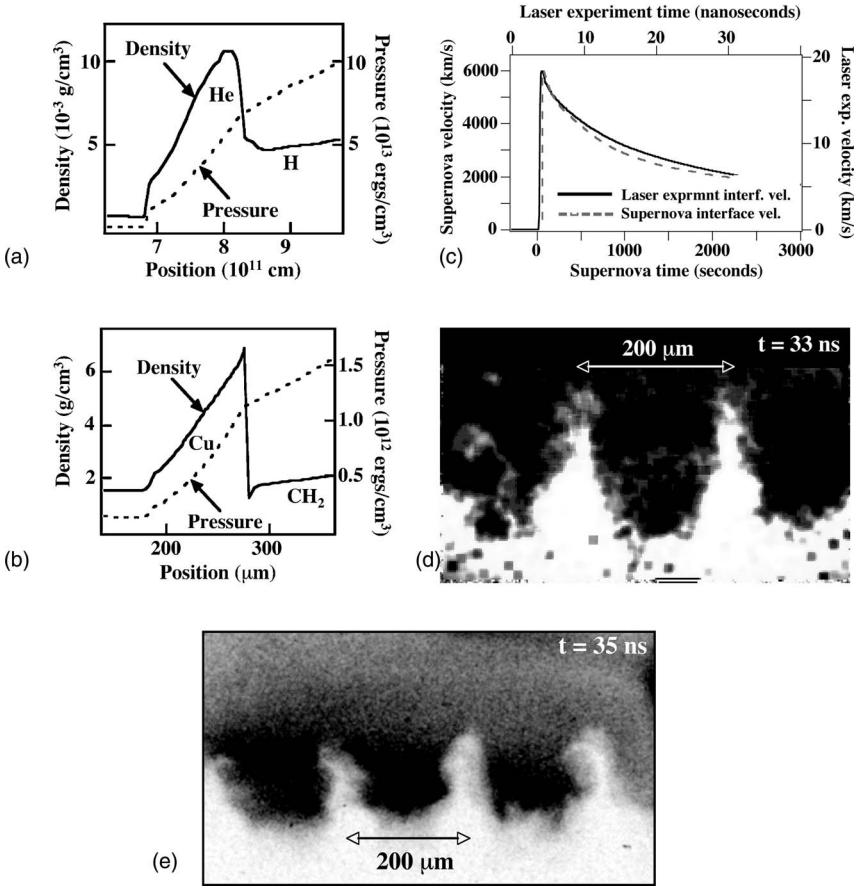

FIG. 9. Hydrodynamic simulations for the supernova and laboratory experiment. (a) Spatial profiles of the pressure and the density for the SN at 2000 s, and (b) the laboratory experiment at 20 ns. Adapted from Ryutov *et al.*, 2001. (c) The velocity of the He-H interface in the supernova and in the scaled laser experiment. The curves are essentially identical, up to the scale transformation. This is a prerequisite for making a scaled laboratory experiment on the evolution of 2D or 3D perturbations. Adapted from Kane, Arnett, *et al.* (1999). (d) A radiograph obtained at $t=33$ ns of the nonlinear RT induced mixing in the first scaled SN experiment. Adapted from Remington *et al.*, 1997. (e) A sum over multiple images from the same experiment as shown in (d), corresponding to an average time of $t_{ave}=35$ ns. Adapted from Remington *et al.*, 1999.

lution of the shock wave strength and the density and pressure distribution near the interface where the RT instability is evolving can, for example, be modified. One can also vary the materials constituting the package and thickness of the layers. Figure 9(b) shows the density and pressure profiles across the interface between copper and plastic obtained in this way. Indeed, these distributions are quite similar to those expected in the SN [Fig. 9(a)]. The temporal dependence of the parameters in the simulation experiment can be adjusted to match that of the supernova. This is illustrated in Fig. 9(c) (Kane, Arnett, *et al.*, 1999) with a plot showing the velocity versus time of the interface for the SN and laboratory experiment.

In the experiment by Remington *et al.* (1997) a planar geometry was used. This means that this particular experiment can imitate the real SN system only for a limited interval of time within which the radius of the He-H interface has not changed by more than 20% or so. This, in turn, means that only relatively short-wavelength perturbations can be simulated. Figure 9(d) shows a sample radiograph from this experiment showing the RT evolution of a $\lambda=200$ μm wavelength perturbation well into the nonlinear regime.

D. Issues of the hydrodynamic similarity

An attractive feature of laboratory experiments for assessing the 2D and 3D SN hydrodynamics and for code validation is the ability to control and vary the initial conditions, repeat an experiment as many times as needed, and equip it with various diagnostics as required. However, in order to produce relevant results one has to constraint the variation of the parameters in such a way as to maintain the laboratory system to be hydrodynamically similar to its astrophysical counterpart (despite the 10–20 orders of magnitude differences in the spatial and temporal scales).

By now, a detailed analysis of the similarity constraints met in the hydrodynamics and magnetohydrodynamics is available (Ryutov *et al.*, 1999, 2001; Ryutov, Drake, and Remington, 2000; Ryutov and Remington, 2002). This analysis has shown that the similarity constraints can be easily satisfied within the framework of a so-called Euler similarity, which holds if the Reynolds and Peclet numbers, as well as the magnetic Reynolds number, are very large in both systems.

The Euler similarity stems from the equations of ideal magnetohydrodynamics,

$$\frac{\partial \rho}{\partial t}+\nabla\cdot\rho\mathbf{v}=0,$$

$$\rho\left(\frac{\partial \mathbf{v}}{\partial t}+\mathbf{v}\cdot\nabla\mathbf{v}\right)=-\nabla p-\frac{1}{4\pi}\mathbf{B}\times\nabla\times\mathbf{B},$$

$$\frac{\partial \mathbf{B}}{\partial t}=\nabla\times\mathbf{v}\times\mathbf{B}, \tag{4.1}$$

corresponding to conservation of mass, momentum, and Faraday's law of induction (sometimes called the "line tying equation"). Here $\mathbf{v}$, ρ, p, and $\mathbf{B}$ are the velocity, density, pressure, and magnetic field, respectively. Assuming that the fluid is polytropic, that is, that energy density is proportional to pressure, one can write the following energy equation (e.g., Landau and Lifshitz, 1987):

$$\frac{\partial p}{\partial t} + \mathbf{v}\cdot\nabla p = -\gamma p \nabla\cdot\mathbf{v}, \tag{4.2}$$

where γ is the adiabatic index (the ratio of specific heats). For a fully ionized nonrelativistic gas γ is equal to 5/3; for a gas where the radiation pressure is dominant γ is equal to 4/3; for a diatomic molecular gas γ is equal to 7/5. Equation (4.2) implies that there are no dissipative processes in the fluid, so that the entropy of any fluid element remains constant.

Consider the initial value problem for the set of equations (4.1) and (4.2). Let us present the initial spatial distributions of the density, pressure, velocity, and magnetic field in the following way:

$$\rho_{(t=0)} = \rho^* f\left(\frac{\mathbf{r}}{L^*}\right), \quad p_{(t=0)} = p^* g\left(\frac{\mathbf{r}}{L^*}\right),$$

$$v_{(t=0)} = v^* \mathbf{h}\left(\frac{\mathbf{r}}{L^*}\right), \quad B_{(t=0)} = B^* \mathbf{k}\left(\frac{\mathbf{r}}{L^*}\right), \tag{4.3}$$

where L^* is the characteristic spatial scale of the problem and the other quantities marked by an asterisk denote the value of the corresponding parameter at some characteristic point; the dimensionless functions (vectorial functions) f, g, $\mathbf{h}$, and $\mathbf{k}$ are of order unity. They determine the spatial shape of the initial distribution. We note that there are five dimensional parameters determining the initial conditions:

$$L^*,\ \rho^*,\ p^*,\ v^*,\ B^*. \tag{4.4}$$

Let us then introduce dimensionless variables (which we denote by tilde) in the following way:

$$\tilde{\mathbf{r}} = \frac{\mathbf{r}}{L^*}, \quad \tilde{t} = \frac{t}{L^*}\sqrt{\frac{p^*}{\rho^*}}, \quad \tilde{\rho} = \frac{\rho}{\rho^*}, \quad \tilde{p} = \frac{p}{p^*},$$

$$\tilde{\mathbf{v}} = \mathbf{v}\sqrt{\frac{\rho^*}{p^*}}, \quad \tilde{\mathbf{B}} = \frac{\mathbf{B}}{\sqrt{p^*}}. \tag{4.5}$$

When one expresses the set of equations (4.1) and (4.2) in terms of the dimensionless variables, one finds that this set maintains its form, just all the quantities get replaced by their analogs bearing the tilde sign. Initial conditions presented in the dimensionless variables acquire the following form:

$$\tilde{\rho}_{(\tilde{t}=0)} = f(\tilde{\mathbf{r}}), \quad \tilde{p}_{(\tilde{t}=0)} = g(\tilde{\mathbf{r}}),$$

$$\tilde{\mathbf{v}}_{(\tilde{t}=0)} = v^*\sqrt{\frac{\rho^*}{p^*}}\mathbf{h}(\tilde{\mathbf{r}}), \quad \tilde{\mathbf{B}}_{(\tilde{t}=0)} = \frac{B^*}{\sqrt{p^*}}\mathbf{k}(\tilde{\mathbf{r}}). \tag{4.6}$$

One sees that the dimensionless initial conditions for the two systems are identical if the dimensionless functions f, g, $\mathbf{h}$, and $\mathbf{k}$ maintain their form, and the two dimensionless parameters $v^*\sqrt{\rho^*/p^*}$ and $B^*/\sqrt{p^*}$ remain unchanged,

$$v^*\sqrt{\frac{\rho^*}{p^*}} = \text{inv}, \quad \frac{B^*}{\sqrt{p^*}} = \text{inv} \tag{4.7}$$

(the abbreviation "inv" stands for invariant). The parameter $v^*\sqrt{\rho^*/p^*}$ is usually called "the Euler number" Eu. In other words, provided these two parameters are invariant and initial states are geometrically similar (i.e., the functions f, g, $\mathbf{h}$, and $\mathbf{k}$ are the same), one would have the same dimensionless equations and the same dimensionless initial conditions for *any two hydrodynamical systems* meaning that the systems will evolve identically in a scaled sense.

Returning to the dimensional form, it is straightforward to show by substitution that Eq. (4.1) is invariant under the following scale transformation relating the supernova (SN) setting to the laboratory (lab) setting:

$$h_{\text{SN}} \to a h_{\text{lab}}, \quad \rho_{\text{SN}} \to b\rho_{\text{lab}}, \quad p_{\text{SN}} \to c p_{\text{lab}},$$

$$\tau_{\text{SN}} \to a(b/c)^{1/2}\tau_{\text{lab}}, \tag{4.8}$$

where h, ρ, p, and τ correspond to characteristic spatial, density, pressure, and time scales, respectively (Ryutov *et al.*, 1999). When the transformation (4.8) is inserted into Eq. (4.1), the constants a, b, and c cancel, and the dynamics described by Euler's equation are indistinguishable in the SN hydrodynamics and the laboratory experiment. Both settings are probing the same nonlinear hydrodynamics. Any insights gained through the laboratory experiment apply directly to the SN through the mapping described by Eq. (4.8). For example, the deep nonlinear SN hydrodynamics illustrated in the simulation shown in Fig. 7 could be scaled to the laboratory via Eq. (4.8) and tested with experiments. It is quite possible that such a properly scaled experiment at this level of nonlinearity would have evolved into the fully turbulent regime [see, for example, Figs. 12(c) and 13], as opposed to quasilaminar RT spike penetration, which could affect the overall outward core penetration and core-envelope mixing.

Normally, similarity arguments are used to ensure that some parameter (of interest in a particular problem) can be scaled between two systems. This can be, e.g., the hydrodynamic resistance to the body moving in a fluid, or the energy confinement time in a plasma device [as in Connor and Taylor (1977)]. We are demanding much more, that the whole dynamic evolution of two systems with properly scaled initial conditions be similar.

There are only two constraints (4.7) on five parameters (4.4) determining the evolution of the system. For the second system, one can choose arbitrarily three parameters, say, L^*, ρ^*, and p^*, and, by choosing the mag-

nitude of the characteristic velocity and magnetic field so as to maintain conditions (4.7), obtain a system which behaves similarly to the first one, up to the change of scales. It is very important to recognize that the Euler similarity applies not only to smooth solutions of the Euler equations, but also to solutions containing shock waves. The proof can be found in the work of Ryutov, Drake, and Remington (2000).

The Euler similarity holds for scales exceeding the dissipative scales Δ_{diss}, which are small compared to the global scale L. In the RT instability driven by the onset of an acceleration, dissipation-scale vortices do not appear instantaneously. It takes several eddy turnover times at the global scale (several L/v) for them to appear. In other words, the Euler similarity (with dissipative terms neglected) will correctly describe an early stage of the instability, until small-scale vortices are formed. [We are assuming smooth transition layers, with density scale length L; if one deals with a sharp (zero-scale) transition, small-scale perturbations may appear early in the pulse.] During this early stage there is no need to make any assumptions about the turbulent viscosity, introduce Reynolds stresses, and other approximate ways of description: the Euler equations correctly describe this stage, including the formation of smaller-scale vortices. In a number of cases, including the SN explosion and its laboratory simulation, this means that much of the evolution relevant to SN core penetration can be adequately described by the Euler equations, with viscosity neglected. Within the time interval of several L/v the system can already reach a strongly mixed state.

It is interesting, however, to assess what would happen later in time, were there is a need to study this later evolution. The question we pose is to what extent will the behavior of the two systems be similar at larger scales if Reynolds numbers, albeit very large, are different in the two systems (meaning that the relative values of the dissipative scales are different). One suspects that the differences on the global scale will not be very large; they will probably appear in the terms of order of ln(Re), or in terms that depend on Re even more weakly. This assertion is based on the results from a number of relevant problems exhaustively studied experimentally. Examples include turbulent pipe flow [see, e.g., Landau and Lifshitz (1987)], and a turbulent flow past a body at high Reynolds number [see Gjevik (1980), Cantwell (1981), and Van Dyke (1982) for excellent pictures of such flows over a broad range of Reynolds numbers]. The issue of the development of dissipative scales in laboratory experiments has been discussed recently by Robey and co-workers (Robey *et al.*, 2002; Robey, 2004; see also Dimotakis, 2000). The first steps have been made in experiments on the early generation of small-scale turbulence by introducing short-wavelength perturbations at the interface (Kuranz *et al.*, 2005).

The question of when does scaling break down needs further study. In other words, at what point in the evolution would a scaled SN experiment no longer correctly reproduce the nonlinear or turbulent SN dynamics. It may be informative to conduct a set of experiments related to each other by a broader (than the Euler) similarity, the so-called "perfect similarity," which holds for an arbitrary equation of state (not necessarily polytropic) (Ryutov and Remington, 2003a, 2003b; Ryutov *et al.*, 2004). The goal would be to determine at what stage of the evolution differences would arise solely due to differences in Re. As this requires a large change of spatial scale and hence of the drive energy, the advent of the NIF laser (see Sec. II.B) may open up this possibility.

E. Experiments on SN type-II hydrodynamics

For the past several years a team of researchers has conducted a series of experiments aimed at the problem of RT instabilities at the H-He interface. The point of these experiments is to observe the nonlinear dynamics of this process in a well-scaled environment. In the context of the results, one can then ask whether the simulation codes in fact calculate the deeply nonlinear behavior of the RT instability correctly, and whether any other physics, not present in the simulations, appears in the experiments. All these experiments begin by producing a blast wave, as discussed above, applying the initial ablation pressure either through direct laser irradiation or through x-ray irradiation (see Sec. II). The subsequent structure in the target then determines which aspects of RT dynamics are being explored.

The first such experiments (Kane, Arnett, *et al.*, 1997, 1999, 2000; Kane *et al.*, 1997; Remington *et al.*, 1997, 1999) used the Nova laser to examine RT growth from a single-mode initial perturbation at a planar interface. The target structure involved a 85-μm-thick Cu layer followed by 500 μm of plastic (CH_2 at $\rho=0.95$ g/cm^3). The profiles of density and pressure 20 ns after the laser pulse began are shown in Fig. 9(b) (Ryutov *et al.*, 1999). The Cu-plastic interface was rippled by a sinusoidal perturbation with a 200-μm wavelength and a 20-μm amplitude. Figure 9(d) shows a radiograph of the resulting structure at 33 ns (Remington *et al.*, 1997) and Fig. 9(e) shows the result averaged over multiple images corresponding to an average time of 35 ns (Remington *et al.*, 1999). The distance from the valleys to the peaks in the observed modulations (known as the "bubble-to-spike" distance) has become approximately equal to the initial wavelength of 200 μm, meaning that the evolution has entered the nonlinear regime. Simulations using the astrophysical code PROMETHEUS (Fryxell, Müller, and Arnett, 1991; Arnett, 1996) and the laboratory code CALE (Tipton, 1990), reproduced this result, but the detailed shape of the structures did not closely resemble what was observed in this first experimental attempt.

Subsequent experiments (Robey *et al.*, 2001) have both improved the quality of the data and explored other aspects of RT dynamics, using the Omega laser. One aspect explored has been RT growth in diverging systems, both cylindrical and spherical (Drake *et al.*, 2002). In the spherically expanding case (not shown) a hemispherical plastic capsule (of density 1.37 g/cm^3, in-

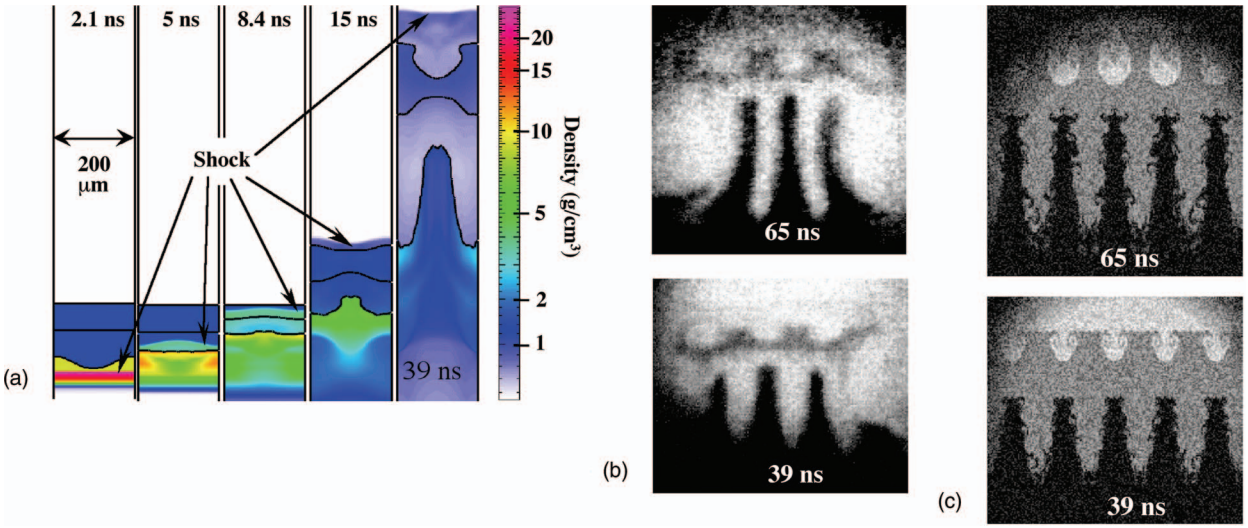

FIG. 10. (Color) Code simulations vs experiment on coupled interface effects. (a) The laser beams strike a 10-μm-thick ablator layer on the front surface of the Cu (ρ_0=8.9 g/cm^3), which is of 85 μm average thickness. The Cu interface is modulated at a wavelength of 200 μm and an amplitude of 15 μm, backed by a polyimide plastic layer, 150 μm thick, with a 75-μm-thick CH tracer with a 4.3 at. % doping of Br. Both have a density of 1.4 g/cm^3. The final layer is 1700 μm of CRF foam at ρ_0 =0.1 g/cm^3. In the experiments, the resulting structures are radiographed from the side by x-ray backlighting as discussed in Sec. II. Adapted from Kane *et al.*, 2001. (b) The experimental radiograph at 39 ns (bottom) and 65 ns (top) for the experiment corresponding to the design simulation shown in (a). Adapted from Kane *et al.*, 2001. (c) The results from FLASH simulations of this same experiment. Adapted from Calder *et al.*, 2002.

side radius 220 μm, and thickness 110 μm) was irradiated from the inside. It included a patch of Ge-doped plastic as a tracer for radiography, and was in some cases modulated with an initial mode (70-μm wavelength, 10-μm peak-to-valley amplitude). The capsule was mated to a large volume of low-density (50–100 mg/cm^3) foam. The unmodulated capsule retained its shape while expanding nearly a factor of 3 in radius. The modulated capsules developed highly nonlinear structures. This experiment was simulated using CALE and the front-tracking hydrodynamics code FRONTIER (Glimm *et al.*, 2001). Here again, and in the presence of better data, the simulations reproduced the qualitative features but not the exact quantitative details.

Another aspect of RT dynamics explored by experiments has been the coupling between interfaces. In an exploding star, the initial modulations of interior layers can induce structure into the blast wave that can affect layers outside it. The experiment to examine this (Kane *et al.*, 2001) used the target structure shown in Fig. 10(a), with details described in the caption, and the results are shown in Fig. 10(b). One can see the Cu spikes, extending upward from below, and the modulations in the second interface, made visible by the tracer strip in the plastic below the interface. Detailed simulations of this experiment were carried out as part of a validation study by Calder *et al.* (2002, 2004) for the astrophysical code FLASH, which includes adaptive grids and other advanced features. Comparison of the simulation results with experimental images supports the same conclusion as in the previous cases. The qualitative features of the data are reproduced very well by simulations. Quantitatively, several details are not accurately reproduced, including the exact spike length, the height of the structures in the interface, and the behavior at the edges of the system. In the specific case of the FLASH simulations, the length of the Cu spikes was found to change with the number of levels of mesh refinement in the simulation, but did not appear to be converging toward the experimental value.

Experiments on the development of multimode perturbations and the transition to a turbulent mix at the interface have been carried out and analyzed in the context of their correspondence to the code results (Robey, Zhou, *et al.*, 2003 Miles, Braun, *et al.*, 2004; Miles, Edwards, *et al.*, 2004). Robey, Zhou, *et al.* (2003) observed the evolution of an eight-mode pattern [Fig. 11(c)], and the simulations, shown in Fig. 11(a) as a numerical radiograph and in Fig. 11(b) with experimental noise artificially added in, are in a reasonable agreement down to the scales determined by the experimental resolution of ~10 μm Miles, Braun, *et al.* (2004). In the simulations and experiment described by Miles, Edwards, *et al.*, (2004), the instability was driven by a strong blast wave giving rise to a Mach number for the growing perturbations as high as 0.2–0.4. Surprisingly, their simulations suggest that the instability "remembers" small-scale details of the initial conditions well into nonlinear stage of the evolution. An example of the experimental results over the range of 13–37 ns is given in Figs. 12(a)–12(c). The initial perturbation corresponded to an initial wavelength (λ) and amplitude (η_0) of 50 and 2.5 μm, with a λ=5 μm, η_0=0.25 μm "noise" mode superposed (Miles, Edwards, *et al.*, 2004). An M=15 blast wave is driven

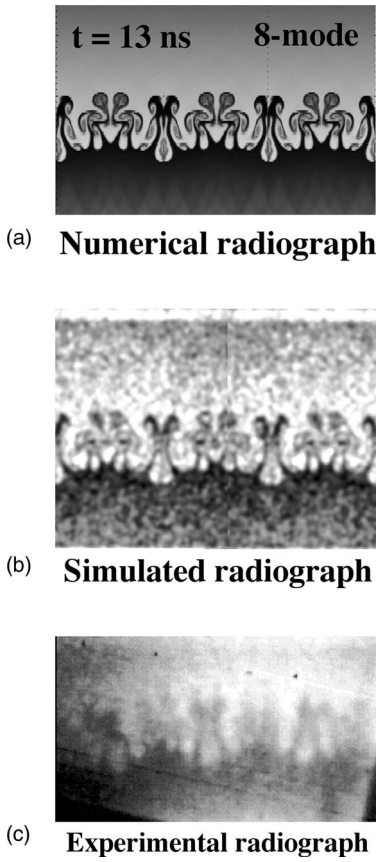

FIG. 11. Comparison of numerical simulations and experiment on a multimode RT instability. (a) A numerical radiograph from simulations. (b) Same as (a), except with experimental noise added into the simulated output. (c) The experimental radiograph at $t=13$ ns, on strong shock-driven experiments done at the Omega laser. Adapted from Miles, Braun, *et al.*, 2004.

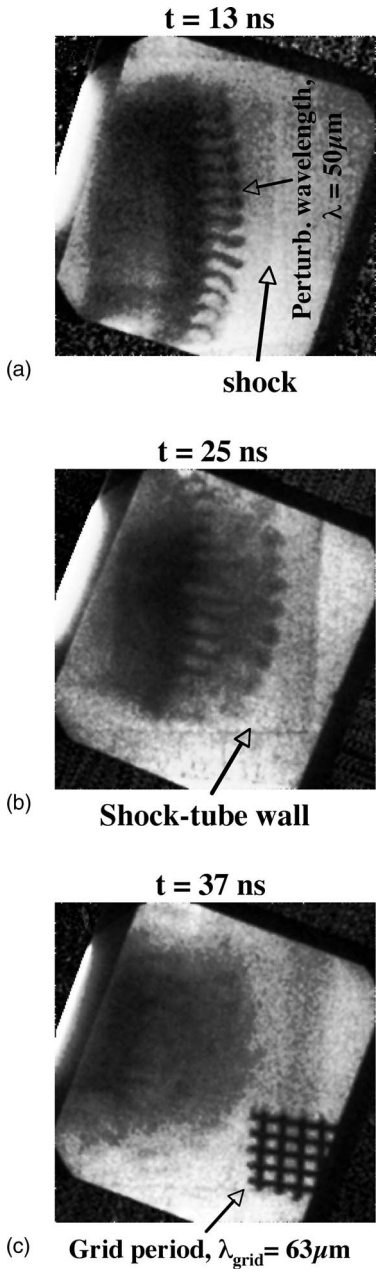

FIG. 12. Experimental observation of a possible transition to turbulence in the deeply nonlinear stage of the RT instability. Side-on radiographs at (a) $t=13$ ns, (b) $t=25$ ns, and (c) $t=37$ ns (Robey, 2004; Miles *et al.*, 2005). Adapted from Miles *et al.*, 2005.

through the polyimide– ($\rho=1.41$ g/cm^3) CRF foam ($\rho=0.05$ g/cm^3) interface. Approximately laminar RT spike evolution is observed at 13 ns. By 25 ns, the spikes are starting to interact through the KH-induced broadening of the spike tips. By 37 ns, it appears that the evolution has entered a fully mixed, fully turbulent regime. This late-time experimental image looks quite different from the laminar, albeit chaotic, RT spikes from the SN simulation shown in Fig. 7. It would appear that the SN simulation is not capturing the transition to a fully mixed, fully turbulent state, due to the finite numerical Re.

A computational development that holds great promise for these types of simulations is the adaptive mesh refinement technique, which now allows such integral simulations to be done in three dimensions. In Fig. 13, we show initial results from such a simulation (Miles *et al.*, 2005) for a proposed NIF experiment. The simulation corresponds to a 2D single mode perturbation with $\lambda=50$ μm wavelength, $\eta_0=2.5$ μm initial amplitude, superposed with a random 3D noise function, and was driven with a similar strong blast wave ($M\sim20$) across a polyimide-foam interface. The simulations were done in both two dimensions (top row) and three dimensions (bottom row). The differences are striking. The 2D and 3D simulations are similar up to the $\eta/\lambda\sim2.5$ (where η/λ corresponds to the peak-to-valley perturbation amplitude over the dominant perturbation wavelength). Beyond this stage of evolution, however, the 3D simulation undergoes a dramatic mixing transition, and enters the fully mixed, fully turbulent regime, whereas the 2D simulation is chaotic, but still largely laminar. Although these simulations assumed a NIF-scale drive, it is interesting that the transition to a fully mixed state occurs at a similar η/λ in the Omega experiment, shown in Figs.

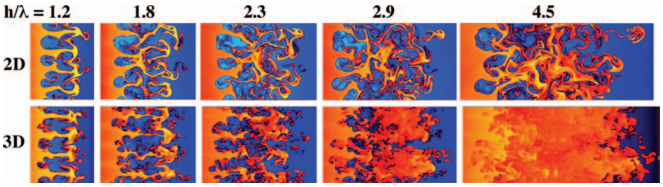

FIG. 13. (Color) Results from adaptive mesh refinement simulations of a proposed scaled SN hydrodynamics experiment for NIF. The hypothetical experiment simulated was assumed to be similar to that described in Fig. 12, except that it was driven harder, with a $M\sim 20$ shock. Also, a 3D high mode number noise spectrum was added onto the 2D single-mode perturbation as a seed. The top row was for simulations run in 2D, versus the bottom row was done in 3D with an adaptive mesh refinement code. With simulations run in 3D, with a 3D high-frequency noise spectrum, the deep nonlinear RT evolution is observed computationally to pass through the mixing transition, and enter a fully turbulent regime. Adapted from Miles *et al.*, 2005.

12(b) and 12(c). The conclusion, for the SN blast-wave drive, is that once $\eta/\lambda \gtrsim 5$, the RT evolution should transition into a fully mixed, fully turbulent state. If anything, this transition slightly slows down the overall spike and bubble front penetration (Miles *et al.*, 2005). As a result, based on the experiments shown in Fig. 12 and the 3D adaptive mesh refinement simulations shown in Fig. 13, it seems very unlikely that 3D turbulent mixing in the SN problem could resolve the "SN mix problem." It seems one needs, rather, to examine the initial conditions for the explosion for a resolution to this problem of core penetration. The impact of initial conditions on mixing has been addressed in recent experiments (Drake, Leibrandt, *et al.*, 2004), and is continuing.

At this point one can ask what are the implications of the experiments to date for the questions asked above. Based on comparisons with experiments, the simulations appear to correctly calculate deeply nonlinear RT dynamics, although the details are not precisely reproduced and obtaining good agreement with experiment often requires iteration. From the point of view of global evolution, it would appear unlikely that the simulations are sufficiently in error to explain the observations from SN 1987A.

As to whether other physics appears in the dynamics that the codes do not address, the answer is twofold. At the level of these simple yet deeply nonlinear systems, other physics does not appear to be a significant effect. (To be sure, the systems were set up to emphasize pure hydrodynamics.) An issue of the effect of the Reynolds number, which, although very large in both laboratory and astrophysics, differs substantially between the two systems, is more subtle. It seems likely that this will be addressed in future experiments (Robey *et al.*, 2003). In conclusion, this work has shown that laser experiments can be carried out for parameters that are scalable to the dynamics of actual SNe. The results have demonstrated rather conclusively that the hydrodynamics codes work well, even into the deep nonlinear regime, in scaled SN settings. Discrepancies between SN models and SN observations seem more likely to be due to the initial conditions assumed, rather than due to the complexity of the nonlinear hydrodynamics simulations.

V. SUPERNOVA REMNANTS, BLAST WAVES, AND RADIATION

A. Introduction

The explosion of a star lasts only a few months. In contrast, the remnants from these explosions, that is, supernova remnants (SNRs), can be observed for centuries if not millennia. SNRs are the observable structures that form through the interaction of the ejecta from a stellar explosion with the surrounding (circumstellar) environment. In addition, SNRs are widely believed to produce most of the cosmic rays that irradiate the Earth. Laboratory experiments can help improve our understanding of some of the mechanisms present in SNRs, and can help test the computational models we build to interpret their behavior. In Sec. V.B, we provide some background regarding SNRs, whereas in the rest of this section we summarize existing experiments.

B. General features of supernova remnants

Supernova remnants are created from the kinetic energy of the exploding star, typically about 10^{51} ergs. The stellar ejecta from the explosion undergo a homologous expansion, with velocity v, radial distance r, and time t related by $v=r/t$. Expansion cooling reduces the temperature of this material to a low value early on, so that nearly all the energy of the ejecta is in kinetic energy. The first phase of SNR evolution is the free expansion (or "young remnant") phase, during which the leading edge of the expanding ejecta drives a "forward shock" into circumstellar matter at velocities of order 10 000 km/s. A "reverse shock" propagates from the contact discontinuity (i.e., the "interface" where the SN ejecta meets the ambient medium) back into the ejecta; in the laboratory frame this reverse shock at this phase still moves in the outward direction (Chevalier, 1982). Eventually, the mass of the accumulated circumstellar matter exceeds the mass of the stellar ejecta. This is generally taken to mark the (gradual) transition to the Sedov-Taylor phase. As this phase begins, the reverse shock runs in to the center of the SNR and disappears, after which the SNR is believed to develop the characteristic structure of a Sedov-Taylor blast wave (Whitham, 1974, p. 192). During this phase, the SNR has a single shock behind which the density and pressure decrease, and a radial size that increases with time as $R(t)\sim t^{0.4}$. Eventually the SNR becomes an old remnant, corresponding to essentially a big bubble in the sky, with denser material around it.

Throughout the development of the SNR, the shocked matter radiates energy, which escapes because the SNR is optically thin. The role of radiation varies depending on the specific parameters of the particular

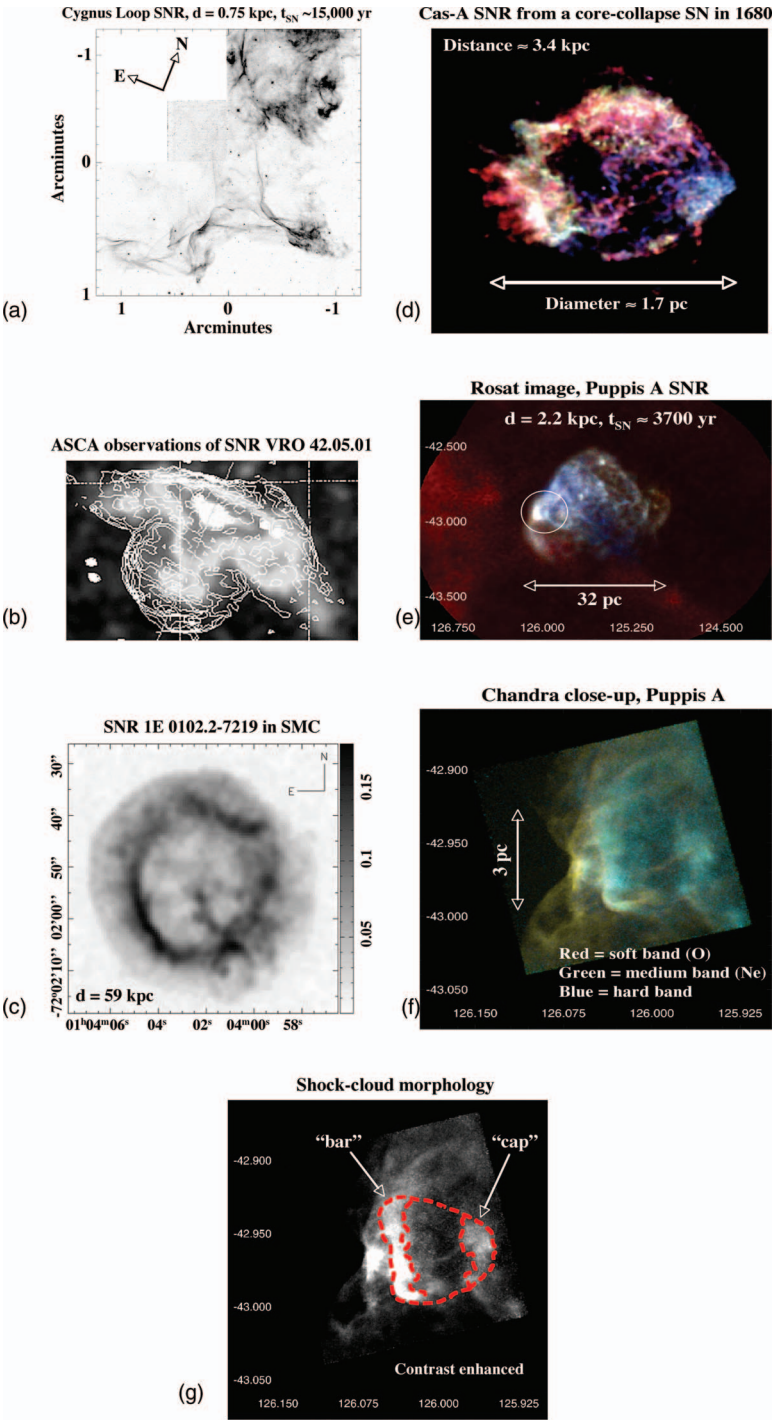

FIG. 14. (Color) Supernova remnants offer a visual example of strong shock dynamics in the universe. (a) Hubble Space Telescope Wide-Field Planetary Camera 2 observations in Hα of the Cygnus Loop supernova remnant (SNR), which is located at a distance of ~0.75 kpc, and is the result of a supernova that occurred ~15 000 yr ago. The image shows the SNR blast wave interaction with an interstellar cloud on physical scales of 10^{15} cm. Shocks viewed face-on produce diffuse emission, while sharp filaments are characteristic of correspond to shocks viewed edge-on shocks. Individual shocks in the cloud of density $n \approx 10^{-15}$ cm^{-3} are observed to have velocity $v_s = 170$ km s^{-1}. The image is scaled linearly from 0 (white) to 4 $\times 10^{-14}$ ergs cm^{-2} s^{-1} pixel^{-1} (black). Adapted from Levenson and Graham, 2001. (b) Interaction of a supernova remnant (the hemispherical object to the lower left) and a molecular cloud (the elongated object above). The figure shows a grayscale image of the x-ray emission, overlaid with a contour image of the radio emission. Adapted from Guo and Burrows, 1997. (c) An image of SNR E0102.2-7219 from Chandra. Colors encode the x-ray photon energy (red is softer, blue is harder, white is the mean spectrum). Adapted from Gaetz *et al.*, 2000. (d) Cassiopea-A remnant. Colors correspond to three different energy bands: 0.6–1.65 keV (red), 1.65–2.25 keV (green), and 2.25–7.50 keV (blue). Adapted from Hughes, Rakowski *et al.*, 2000. (e) Rosat x-ray image of Puppis A supernova remnant. Reproduced from Hwang *et al.*, 2005. (f) Chandra x-ray image of the Bright Eastern Knot region of Puppis A SNR. Reproduced from Hwang *et al.*, 2005. (g) Same as (f), only in black and white with contrast enhancement, and with the shock-cloud "cap" and "bar" features indicated. Adapted from Hwang *et al.*, 2005.

event and on the phase that the remnant is in. In particular, conditions can be met (usually late in the explosion) where radiation causes a collapse of the shocked material into a thin shell (Cioffi *et al.*, 1988; Blondin *et al.*, 1998; Cohen *et al.*, 1998), which can manifest a number of specific instabilities (Vishniac, 1983; Bertschinger, 1986; Innes *et al.*, 1987; Ryu and Vishniac, 1987). The Cygnus Loop, a 15 000-year-old remnant that is close enough to be six times the size of the Moon on the night sky, is in this phase. A small part of this remnant is shown in Fig. 14(a) (Levenson and Graham, 2001). The structures evident in the Cygnus Loop are not an exception: the remnants almost universally reveal complex 3D structures. The origin of these structures can be related to initial 3D nonuniformities of circumstellar medium, to instabilities at the contact discontinuity or the blast wave, to 3D features "imprinted" on the ejecta during the SN explosion itself, or to various combinations of these.

In particular, the massive stars that are thought to be the progenitors for core-collapse supernovae are usually formed in regions where dense molecular clouds are present. Therefore there is a significant chance that the ejecta from the star will interact with other matter such

as a molecular cloud. Figure 14(b) shows such an interaction (Guo and Burrows, 1997).

An example that is thought to be related to the Rayleigh-Taylor instability at the contact discontinuity (Gull, 1973; Shirkey, 1978; Dickel *et al.*, 1989; Gaetz *et al.*, 2000) is shown in Fig. 14(c) which shows one of the Chandra images of SNR E0102.2-7219 (Blair *et al.*, 2000; Gaetz *et al.*, 2000; Hughes, Rakowski, and Decourchelle, 2000; Rasmussen *et al.*, 2001). One can see modulations, spectroscopically identified to be at the contact surface, that seem likely to have been produced by Rayleigh-Taylor instabilities. It is notable that the mode number of these modulations appears larger than the mode number typically seen in simulations.

A memory of the initially unstable and structured explosion of the core-collapse supernova may be responsible for an amazing array of knots, filaments, and flocculi in the relatively young (300-year old) Cassiopeia A remnant shown in Fig. 14(d) (Anderson and Rudnick, 1995; Reed *et al.*, 1995; Keohane, *et al.*, 1996; Hughes *et al.*, 2000). Again, there are "bubbles" and "spikes" at various places around the outer boundary that appear Rayleigh-Taylor-like.

An example of x-ray images of a prominent shock-cloud interaction in the Puppis A SNR is shown in Figs. 14(e)–14(g) (Hwang *et al.*, 2005). Figure 14(e) shows the entire SNR, in an x-ray image taken with the Rosat x-ray satellite. This remnant sits at a distance of ~2.2 kpc, and is the result of a core-collapse SN IIL/b explosion of a $\sim 25M$ progenitor some ~3700 years ago. A higher resolution x-ray image of the region called the Bright Eastern Knot was taken with the Chandra x-ray observatory, and is shown in Fig. 14(f). Here the colors correspond to the soft band (O) in red, medium band (Ne) in green, and hard band in blue. A contrast-enhanced, black and white version of this image is shown in Fig. 14(g), with a region identified as a shock-cloud interaction identified. In particular, features called the "cap" and "bar" are indicated. These will be discussed in more detail in Sec. V.D, in the discussion of a scaled, strong shock, laboratory experiment (Klein *et al.*, 2003).

Many of these aspects of SN explosions can be simulated in laboratory experiments with high-intensity lasers or *Z* pinches. In the rest of this section we discuss experiments of various degrees of complexity related to (i) the overall 1D dynamics, (ii) the interaction between high-speed flows and density clumps, and (iii) studies of various aspects of radiative shocks.

C. Simulating one-dimensional dynamics

In order to create an experimental setting that can be scaled to actual SNR conditions, one must produce a system in which flowing, cool ejecta encounter a reverse shock, with the shocked material driving a forward shock through low-density matter. The first experiments to accomplish this were those of Drake and co-workers (Drake, Carroll, *et al.*, 1998, 2000; Drake, Glendinning, *et al.*, 1998; Drake, Smith, *et al.*, 2000) using the Nova laser facility (Campbell *et al.*, 1986). These experiments were in a planar geometry, intended to simulate a small segment of the overall SNR expansion. The experiment began when an intense x-ray flux, produced by laser heating of a gold cavity, irradiated a 200-μm-thick layer of plastic. The x rays ablated the plastic, launching a strong shock wave through it, at a pressure of 5×10^{13} dynes/cm^2 (50 Mbars). This was the analog of the initial blast wave produced by the SN explosion. This shock wave compressed, accelerated, and heated the plastic. When the shock broke out of the plastic, the ejecta from its rear expanded, accelerated, cooled, and decompressed across a 150-μm-wide gap. In an actual SNR, spherical expansion provides the decompression (McKee, 1974). Here the gap served an analogous function. The ejecta then launched a forward shock into the ambient matter, in this case a foam whose density was less than 1% of the density of the compressed plastic layer. The ejecta stagnated against the (moving) contact surface with the foam, which launched a reverse shock into the ejecta, just as occurs in an SNR. In a young SNR and in this experiment, respectively, $\mathrm{Re} = 6 \times 10^8$ and 7×10^6, $\mathrm{Pe} = 10^7$ and 10^4. Radiative losses are unimportant in both systems. Based on Euler scaling, the relation of the time scales is that 1 ns in the experiment corresponds to 1 year in the SNR. This system can be used for basic setup and benchmarking of hydrodynamic simulations.

D. Interaction of shocks and clumps

The local structures observed in SNRs may result from instabilities, but much of it probably is due to clumpiness in the circumstellar matter or in the ejecta. The clumpiness may in turn affect the development of instabilities, as has been explored in some simulations (Jun *et al.*, 1996; Kane, Drake, and Remington, 1999). Since clumps introduce substantial vorticity into the fluids that interact with them, experiments with clumps test the accuracy of simulations somewhat differently than shock waves and interface instabilities do. To date, no experiment has addressed the impact of multiple clumps, like those explored by Jun *et al.* (1996), on SNR evolution. However, two experimental studies have made relevant measurements with a single clump.

The issue of cloud destruction by a shock has been addressed in some detail in experiments begun at the Nova laser (Klein *et al.*, 2000, 2003) and continued at the Omega laser (Robey *et al.*, 2002). Both sets of experiments involve the generation of a nearly planar blast wave, within a shock tube, its propagation over a significant distance, and its subsequent interaction with a dense sphere of material. The geometry of the Omega experiment has been shown in Fig. 2(c). In this experiment, by the time when the shock arrives at the location of the solid Cu sphere, it (the shock) has long since been overtaken by the rarefaction from the front surface of the irradiated material, giving it a blast-wave structure not unlike that present in a Sedov-Taylor phase SNR.

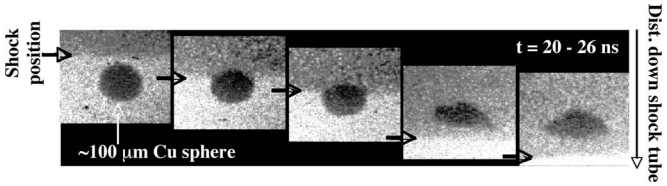

FIG. 15. Experimental images from the early-time evolution of the strong shock ($M=v_{shk}/v_{sound}\sim 10$) compression of a $\sim$100-μm-diameter solid copper sphere embedded in plastic (initial density contrast $\rho_{Cu}/\rho_{CH}\sim 10$). The initial experiment was done on the Nova laser (Klein *et al.*, 2003). This set of images spans the interval of 20–26 ns, where $t=0$ corresponds to when the laser first turns on. The first image on the left shows the shock approaching the uncompressed Cu sphere. The final image on the right shows the fully compressed, umbrella shaped Cu sphere. The images in between show the shock progression through the sphere. Adapted from Klein *et al.*, 2003.

When the shock wave traverses the sphere, the sphere compresses (gets "crushed"). The interaction of the sphere with the postshock flowing plasma produces vortex rings, visible in the last panel of Fig. 2(d). The vortex rings are subject to an azimuthal bending instability (the "Widnall instability") that then produces three-dimensional structure. These experiments provide an excellent test of the ability of astrophysical codes to simulate this type of shock-cloud interaction. Three-dimensional (3D) simulations are required to reproduce these observations. The results from the original experiment on the Nova laser are shown in the full time sequence in Figs. 15 and 16 (Klein *et al.*, 2003). In Fig. 15, the strong ($\sim$Mach 10) shock is shown traversing a $\sim$100-μm-diameter Cu sphere embedded in solid plastic (CH), with an initial density contrast of $\rho_{Cu}/\rho_{CH}\sim 10$. The shock passes through the Cu sphere over the time interval of 20–26 ns (where $t=0$ corresponds to when the laser turned on). During this transit interval, the Cu sphere compresses and distorts into an "umbrella" shape. At later times [Figs. 16(a)–16(f)], the vorticity deposited into the Cu by the shock-sphere interactions cause the Cu plasma "cloud" to evolve into a vortex ring (something like a smoke ring) with a central "cap" or plasma reservoir lagging behind. In the side-on x-ray radiographs shown in Fig. 16(d) these features are labeled bar and cap, respectively. At the latest times [Figs. 16(e) and 16(f)], this vortex ring evolution has triggered an azimuthal (Widnall) instability, and the plasma "smoke ring" starts to break up and evolve towards turbulence in this 3D instability. Simulations of these shock-cloud dynamics are shown in Fig. 17. The 2D simulations [Figs. 17(a) and 17(b)] capture the early-time, cloud compression phase, but fail to reproduce the late-time (i) evolution into a cap and bar shape, (ii) triggering of the Widnall instability, and (iii) transition to turbulence. [Note that we have corrected a typographical error of a factor of 10 in the axes of Figs. 3–11 in Klein *et al.* (2003). The axes of Figs. 17(a) and 17(b) here give the correct spatial scale for the simulation.] The 3D simulation of the laboratory experiment using a realistic equation of state [Fig. 17(c)] shows the complexity of the 3D dynamics, and does show the reservoir cap and vortex ring shape (Robey *et al.*, 2002). The scaled astrophysics simulation using an ideal equation of state [Fig. 17(d)] also shows the cap plus vortex ring bar shape (Klein *et al.*, 2003). Correspondence can now be made between 3D simulations [Figs. 17(c) and 17(d)], experiments [Figs. 16(c) and 16(d)], and x-ray observations of SNR shock-cloud interactions [Figs. 14(e)–14(g)]. The correspondence is striking and compelling, and demonstrates a new capability in HED astrophysics to couple observations, simulations, and scaled laboratory experiments (Hwang *et al.*, 2005).

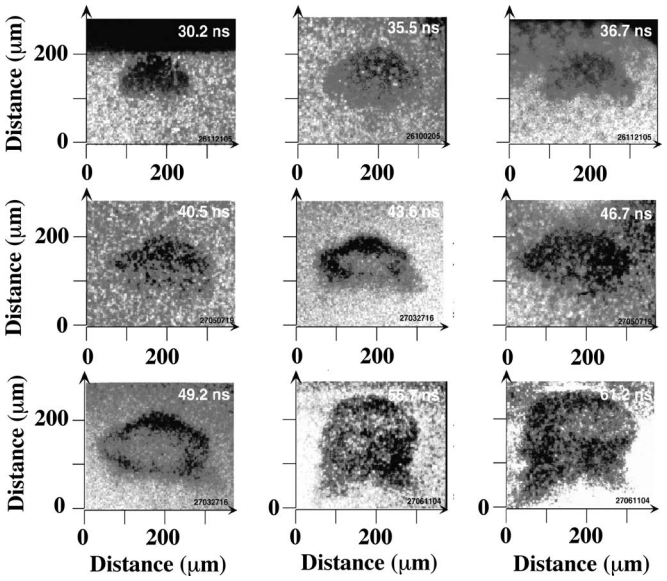

FIG. 16. Late-time evolution of the Cu sphere (scaled cloud) shock-cloud experiment, done on the Nova laser (Klein *et al.*, 2003). The experimental images span 30.2–61.2 ns, and show the evolution from the early-time aftermath of shock compression (30–40 ns) to the formation of vortex rings (42–49 ns), through the initial stages in the transition to turbulence (55–61 ns). Adapted from Klein *et al.*, 2003.

In other experiments, Kang *et al.* created the density structures present in a young SNR and observed their interaction with a (rather large) spherical obstacle (Kang *et al.*, 2000; Kang, Nishihara, *et al.*, 2001; Kang, Nishimura, *et al.*, 2001). The setting was similar to that realized by Drake and co-workers described at the beginning of Sec. V.C (Drake, Carroll, *et al.*, 2000), but now the low-density foam contained a 150-μm-diameter ZrO_2 sphere to observe the interaction of the shock and the ejecta with this sphere. The authors have clarified some details of this experiment for us that may prove useful in reading their papers. The structure of the $C_{10}H_{14}O_4$ foam consists of a thin fiber network, with μm-scale cell sizes. The total laser intensity, and not the intensity of each beam, was 2×10^{14} W/cm^2. The simulations in the papers are all for an initial CH layer thickness of 50 μm. The experiment produced images that show the forward shock, the layer of denser stagnated ejecta, and some complex structures that developed

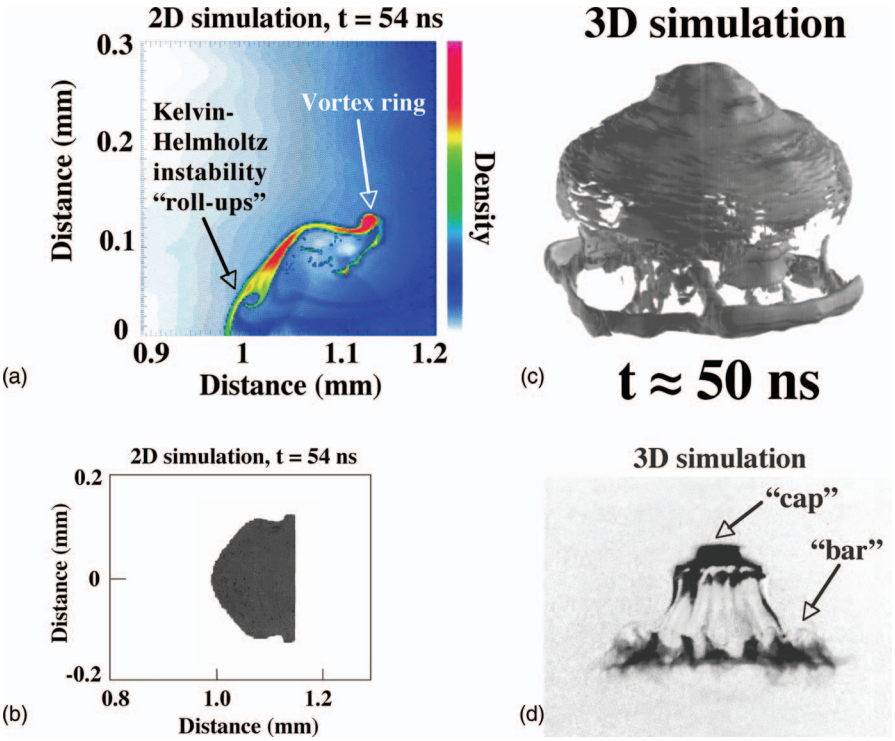

FIG. 17. (Color) Simulations of the shock-cloud experiment done on the Nova laser. (a) One result, showing a color density plot at 54 ns, from a 2D simulation of the experiment shown in Fig. 16. The 2D simulation shows the formation of an unperturbed vortex ring in the "skirt," and a Kelvin-Helmholtz instability induced roll-up in the "cap." (b) Simulated 2D radiograph, assuming 4.5-keV Ti Heα x rays. (c) 3D simulations of the laboratory experiment with realistic EOS. Adapted from Robey *et al.*, 2002. (d) The result from a 3D simulation of a strong astrophysical shock interacting with an isolated cloud, using an ideal EOS, and an adaptive mesh refinement hydrodynamics code. Adapted from Klein *et al.*, 2003.

through their interaction with the sphere, attributed to vortex ring formation.

Beyond the global interaction of a shock wave with a molecular cloud, there are also questions of the detailed interactions of the shock wave driven into the cloud with clumps that contain the vast majority of the cloud mass (Chevalier, 1999). Experiments (Poludnenko *et al.*, 2004) have been designed to examine such interactions using the *Z* machine at the Sandia National Laboratories, but have not yet been accomplished. Experiments where the blast wave was launched into the medium with a modulated cluster density have just begun (Moore *et al.*, 2005a, 2005b).

E. Radiative effects in shocks

Radiative shocks exhibit a range of behavior that depends on the optical depth of the downstream and upstream regions relative to the shock (Drake, 2005). Present-day laboratory experiments provide the possibility to address issues of the radiative cooling of shocked material and the formation of ionized precursors by the radiation of the shocked material. As an example, we present Fig. 18 based on experiments discussed by Bouquet *et al.* (2004) and carried out at the LULI nanosecond laser facility. We first show the result of an illustrative simulation with the ASTROLABE code [Fig. 18(a)]. We see the characteristic structure of a strongly radiating shock, with the ion temperature initially very high, nearly ~1 keV (roughly corresponding to a standard Rankine-Hugoniot relation), then decreasing because of the energy exchange with electrons. Electrons, in turn, are cooled by atomic excitation and ionization processes, with a substantial part of this energy radiated away from the shock region. Eventually, the temperature decreases to a mere 20 eV, whereas the density reaches a value ~30 times higher than the initial density.

In this experiment, laser beams were focused onto a thin (2 μm) polyethylene ablator which pushed a 25-μm layer of a polyethylene foam; the ablator and foam were separated by a 3-μm titanium x-ray shield to prevent x rays formed at the ablation front from preheating the foam "piston." On the other side of the foam, a Xe gas at a density of 1.3×10^{-3} g/cm^3 was situated. The whole design was aimed at driving a shock in matter at low density, so that, at a given laser intensity, the shock velocity would be high, and one would reach temperatures sufficient to make radiative effects important. The foam/gas interface acted as a piston that moved at a velocity of ~70 km/s, driving a strong shock into the Xe gas.

A Mach-Zender interferometer was used to measure the electron density; an interferogram is shown in Fig. 18(b). One sees the trajectory of the shock in Xe (dashed curve), as well as the trajectory of the front end of the ionized precursor (solid curve) produced by photoionization of the unshocked gas by the radiation from the shock region.

Shown in Fig. 18(c) is a comparison of the experimental and calculated profiles of electron density, 200 μm away from the foam surface (which serves as a pusher). The position of the shock corresponds to the steep part of the curve; the left part of the curve corresponds to an ionization precursor. The difference between measurements and simulations is attributed to 2D effects and early preheat.

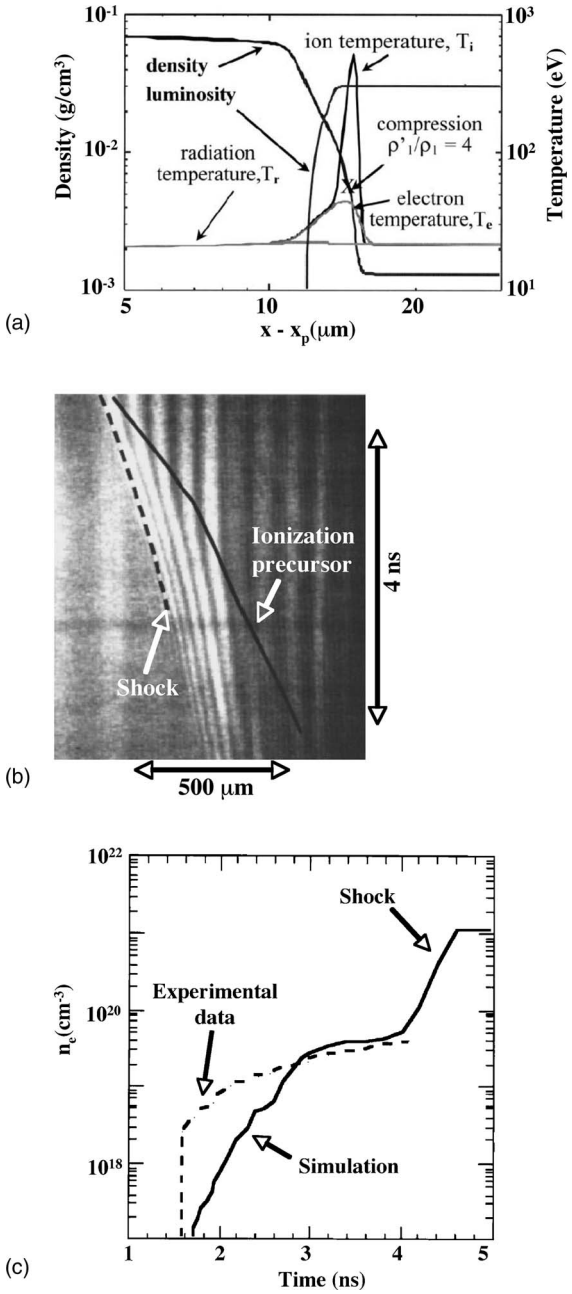

FIG. 18. Formation of a radiative precursor in a strongly shocked Xe gas experiment. (a) Results from 1D design simulations with the radiative hydrocode ASTROLABE, showing that compressions as high as 50 were predicted, due to strong radiative cooling. The initial shock heating was predicted to initially go into ions (T_i), with $T_e = T_i$ equilibration occurring downstream from the shock. (b) The shock trajectory and ionization precursor were measured with optical diagnostics, allowing the average shock speed of 67 km/s to be determined. (c) The electron density profile was also measured with a Mach-Zehnder interferometer, showing the strong ionization precursor, compared with the simulation. Adapted from Bouquet *et al.*, 2004.

Experiments by Keiter *et al.* (2002) on the Omega laser also involve the initial acceleration of a block of material to high velocity. Up to ten laser beams struck the front surface of this target, delivering several kJ of energy to an 800-μm-diameter spot in a 1-ns pulse. The laser irradiation shocked and accelerated a 60-μm-thick plastic layer, which crossed a 160-μm vacuum gap to impact a low-density foam, usually of density 0.01 g/cm^3. This drove a shock wave through the foam at ~100 km/s.

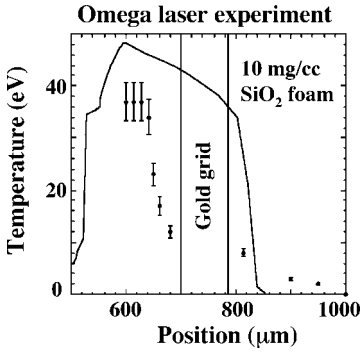

FIG. 19. Data from the radiative precursor experiment of Keiter *et al.* (2002). Temperature profile inferred from the absorption spectroscopy, along with results of a simple 1D radiation hydrodynamics simulation. Adapted from Keiter *et al.*, 2002.

The structure of the precursor was diagnosed using absorption spectroscopy. Additional laser beams irradiated a thulium backlighter plate, permitting an imaging crystal spectrometer to obtain absorption spectra. Absorption lines were detected from up to six different ionization states. The lines from higher ionization states appear at higher temperatures. This allows one, with the help of the OPAL atomic code (Iglesias and Rogers, 1996; Rogers and Iglesias, 1994, 1998), to determine the temperature profile in the precursor. Figure 19 shows an example of the results, and of an initial comparison to results from a very simple radiation hydrodynamic model. One can anticipate that such experiments could provide quality benchmark data for astrophysical modeling.

The observation of a radiatively collapsed shocked layer has also been demonstrated in the experiment by Reighart *et al.* (2006), who used a 3-mm-long, 0.6-mm inner diameter shock tube filled with xenon gas at a density of 6×10^{-3} g/cm^3. The pusher ("piston") was a 50-μm-thick beryllium layer. Simulations with the 1D Lagrangian code HYADES (Larsen and Lane, 1994) have shown the formation of a collapsed layer in the case when radiation losses were taken into account [see Fig. 20(a)] (Reighard, 2006). Note the logarithmic vertical scale: the density in the radiatively collapsed layer is twice as high as in the case with no radiation. Two-dimensional simulations using the code FCI2 (Buresi *et al.*, 1986; Busquet, 1993) allowed accounting for the effect of a finite radius of the shock tube [Fig. 20(b)]. The 2D experimental radiographic image [Fig. 20(c)] shows remarkable agreement with simulations. Note that the velocity of the collapsed layer was quite high, ~140 km/s.

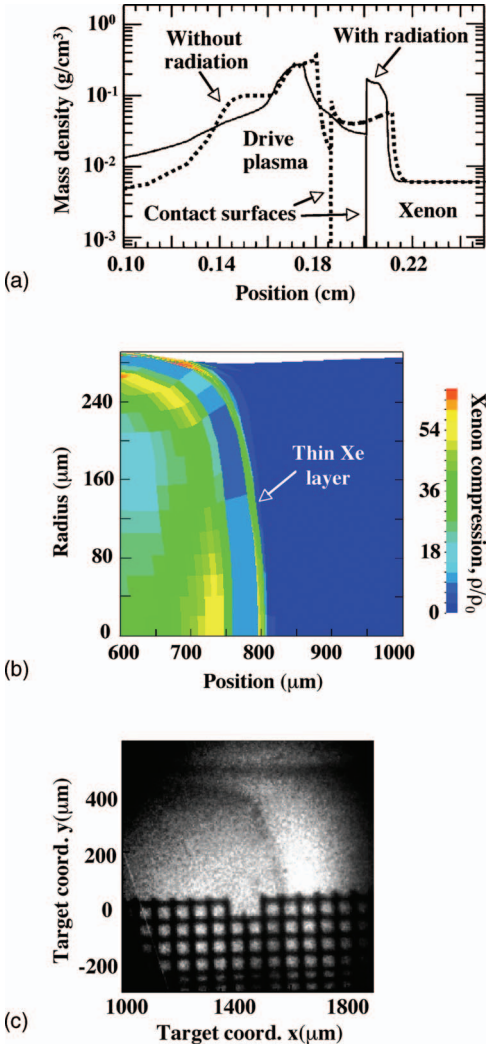

FIG. 20. (Color) Formation of a collapsed layer in dense Xe gas. (a) Density profiles calculated with the HAYDES code for the case with radiation (solid line) and no radiation (dashed line). Adapted from Reighard *et al.*, 2006. (b) Simulations using FCI2, of the 2D geometry, with the finite radius of the shock tube taken into account. (c) Radiographic image showing remarkable agreement with 2D simulations. Adapted from Reighard *et al.*, 2006.

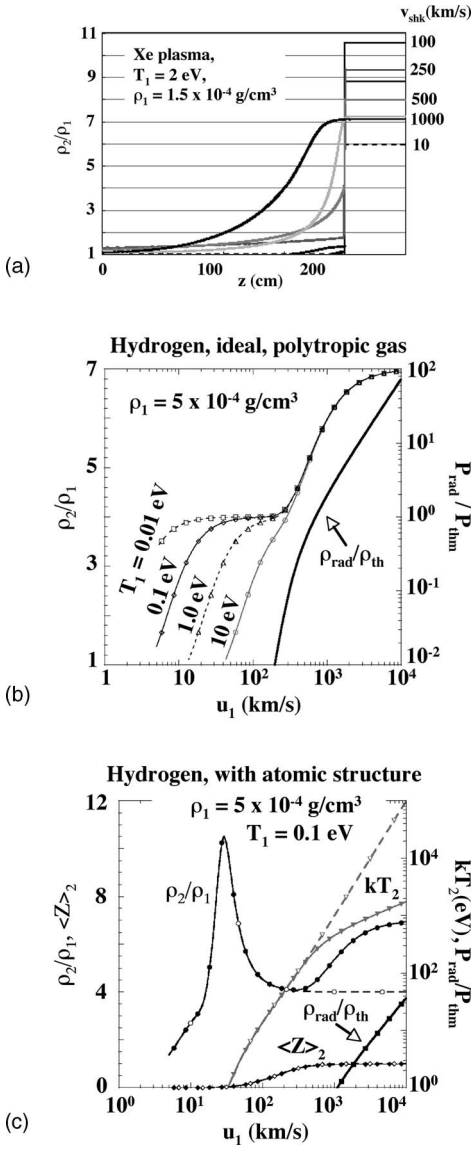

FIG. 21. Effects of the equation of state and radiation on the shock. (a) Radiative precursor for the shock wave in Xe (initial density 1.5×10^{-4} g/cm^3, initial temperature 2 eV). Adapted from Michaut, Stehle, *et al.*, 2004. (b) Shock compression solutions vs initial temperature, including radiation, assuming an ideal polytropic ($\gamma=5/3$) gas. (c) Same as (b) only now treating the atomic structure and ionization, assuming $\rho_1=5\times10^{-4}$ g/cm^3, and $T_1=0.1$ eV for the hydrogen gas. Adapted from Michaut, Stehle, Leygnac, *et al.*, 2004.

Progress has also been made in the theory of radiative shocks, within the approximation of high opacity and local thermodynamic equilibrium. In particular, Michaut and co-workers (Michaut, Stehle, *et al.*, 2003; Michaut, Stehle, Leygnac, *et al.*, 2004) have considered the role of radiation in the jump relations for strong shocks in monatomic gases. These approximations, unfortunately, were never fully satisfied in any of the aforementioned experiments. Still, some interesting qualitative features are worth mentioning: It turns out that the density compression ratio is not a monotonic function of the shock velocity. At a small velocity, when radiation, excitation, and ionization are unimportant, the compression ratio ρ_2/ρ_1 is 4 (for monatomic gases). At higher velocities, when the excitation and ionization "consume" a considerable fraction of the energy of shocked matter, but the radiation pressure is still small, the compression ratio can be quite high, more than 10 (in other words, the equation of state can be very "soft"). However, at yet higher velocity where the radiation pressure becomes dominant in the shocked material, the compression ratio drops to 7 (corresponding to the adiabatic index of radiation $\gamma=4/3$). All this is illustrated for Xe in Fig. 21(a) (Michaut, Stehle, *et al.*, 2004). These effects play a role even in light gases, like hydrogen [Figs. 21(b) and 21(c)] (Michaut, Stehle, Leygnac, *et al.*, 2004). In Fig. 21(b), the shock is assumed to propagate through hydrogen, which in this case is treated as an ideal, polytropic, $\gamma=5/3$ gas.

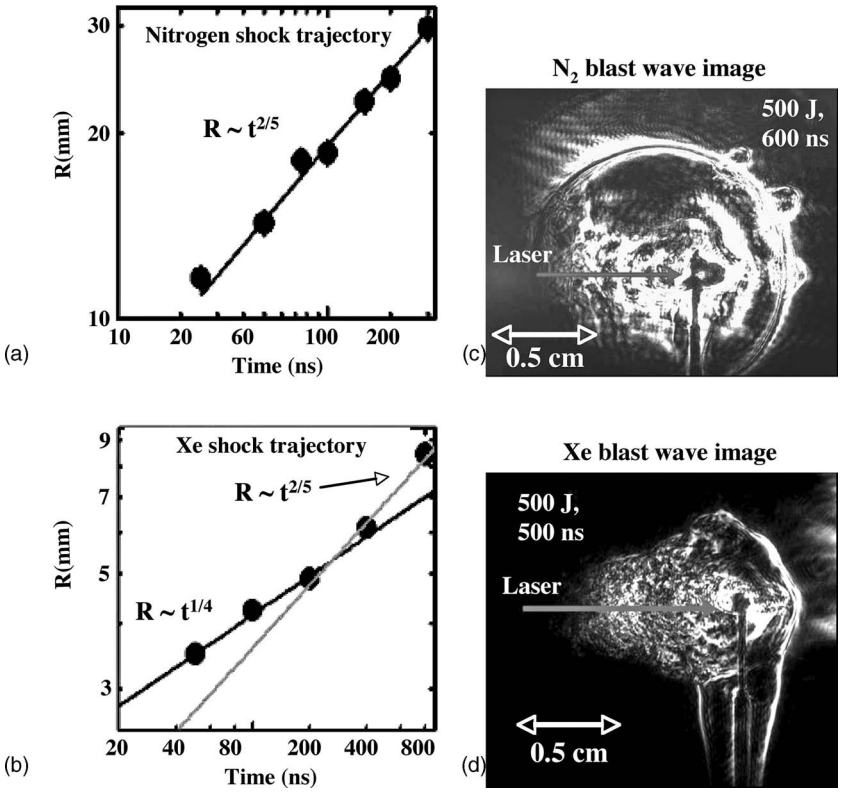

FIG. 22. Blast waves in nitrogen and xenon. Measured shock trajectories for (a) nitrogen and (b) xenon. Measured structure by dark-field imaging of the blast wave for 500-J energy input for (c) nitrogen and (d) xenon. Adapted from Edens *et al.*, 2004.

As long as the initial gas temperature is not too hot, there is a range of shock velocity, ~10–100 km/s, that leads to the strong shock (nonradiative) compression limit of $\rho_2/\rho_1=(\gamma+1)/(\gamma-1)=4$. At higher shock speeds radiative effects become strong, the gas becomes an optically thick, radiation-dominated, $\gamma=4/3$ fluid, for which $\rho_2/\rho_1=7$. The situation changes strongly when atomic structure (namely, bound, excited states, and ionization) is taken into account. In this case, over the regime where bound excited states and ionization occurs, the gas has a lower effective γ, and is much more compressible. This is shown in Fig. 21(c) as the broad peak in ρ_2/ρ_1, occurring for shock strengths in the range of 20–40 km/s (Michaut, Stehle, *et al.*, 2004; Michaut, Stehle, Leygnac, *et al.*, 2004).

F. Blast waves

Experimentally both cylindrical (Ditmire *et al.*, 2000; Shigemori, Ditmire, *et al.*, 2000; Edwards *et al.*, 2001) and spherical (Grun *et al.*, 1991; Edens *et al.*, 2004, 2005; Hansen *et al.*, 2005, 2006) blast waves have been studied. Effects observed include the dependence of the expansion trajectory on the equation of state and on the role of radiation, in the spirit of Keilty *et al.* (2000), Liang and Keilty *et al.* (2000), and the effects of the Vishniac instability of thin shells. We discuss here in detail two recent experiments of this type.

The first was performed by Edens *et al.* (2004) on the Janus laser facility at Livermore (Glaze, 1976) and at the *Z*-Beamlet facility at Sandia (Rambo *et al.*, 2005). A 1-ns laser pulse with energy ranging from 10 J to 1 kJ was focused onto the tip of a metal or nylon pin situated in a target chamber filled with Xe or N_2 at a pressure of between 5 and 10 Torr. The fast energy release at the pin tip created a blast wave, visualized by dark field imaging.

In the case of Xe, the blast wave trajectory initially followed the $r\sim t^{0.25}$ law corresponding to strong radiative losses from the material assembled by the blast wave (Keilty *et al.*, 2000; Liang and Keilty *et al.*, 2000). Later in the pulse, when the gas cooled down, a transition to the Sedov-Taylor dependence $r\sim t^{0.4}$ occurred. In the case of nitrogen, the $t^{0.4}$ dependence was observed throughout the whole experiment [Figs. 22(a) and 22(b)].

The dynamics of a blast-wave-induced thin shell should manifest the overstability predicted by Vishniac. Indeed, in the Xe plasma small-scale structures were clearly visible, whereas in the case of nitrogen the scale of the structures was larger [Figs. 22(c) and 22(d)]—in agreement with the simple observation that the Xe shell should be thinner because of stronger cooling. In a recent experiment by Edens *et al.* (2005), the evolution and decay of the amplitude of a rippled blast wave in nitrogen gas was measured and compared with predictions from the Vishniac theory. This comparison showed that the ripple amplitude decay rate was consistent with a polytropic index (gamma) of 1.4, which was higher than predicted by simulations with a 1D radiation-hydrodynamics code. One interpretation given was that the nitrogen gas was ionized more than expected due to the radiative precursor preceding the shock front.

An interesting effect was observed by Hansen *et al.* (2005, 2006). They used the technique just mentioned to

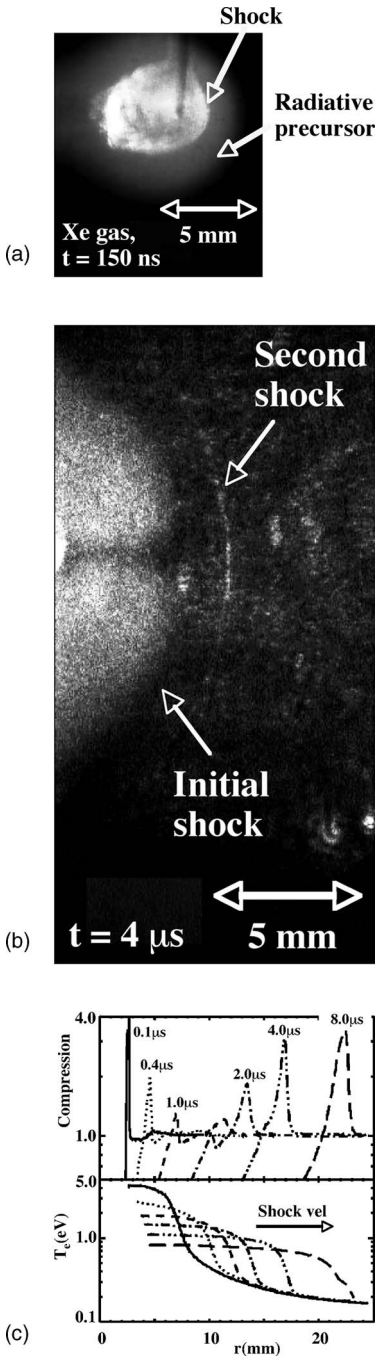

FIG. 23. The emergence of a second shock driven by the ionized precursor in strongly shocked Xe. (a) Schlieren image at $t=150$ ns and (b) at $t=4$ μs. (c) The corresponding spherically symmetrical modeling. Adapted from Hansen *et al.*, 2005.

launch a shock wave into Xe gas and then followed the evolution of the system over a long time scale, up to ~30 μs. At $t=150$ ns, both the shock and gas ahead of the shock are visible [Fig. 23(a)]. Later in time the initial shock weakens and is no longer visible. However, at $t=4$ μs, a second shock appears, at a position well ahead of the possible position of the first shock [Fig. 23(b)]. This suggests that the second shock is driven by the energy deposited in the radiative precursor region, a conclusion supported by numerical simulations shown in Fig. 23(c).

G. Summary

Experiments addressing the dynamics of supernova remnants have demonstrated that blast waves can be produced in laboratory experiments that are scalable to real astrophysical objects. Shock crushing of isolated dense clumps has been reproduced and successfully simulated by hydrodynamic codes, thereby creating a high degree of confidence in the validity of 3D numerical simulations of similar astrophysical objects. Blast wave instabilities have been observed and related to the corresponding astrophysical phenomena. This provides substantial support to the existing astrophysical models of blast waves, their instabilities, and their interactions with clumps. These experiments, for example, dramatically illustrated the need for 3D simulations to reproduce the details of the dynamics of shock-cloud interactions, and demonstrated what is missed with 2D simulations (Robey *et al.*, 2002; Klein, *et al.*, 2003).

What will be established in the future is the global effect of radiative cooling as a strong shock traverses a medium, such as a molecular cloud, where inhomogenieties exist. The effect of radiative cooling on strong-shock-induced turbulent mixing is an exceedingly difficult problem to address quantitatively, yet it occurs routinely in astrophysics. A good example is the proposed jet-induced shock triggering of star burst activity. A particularly interesting case, pointed out recently by Fragile and co-workers, is the jet-induced star formation in "Minkowski's object," a small irregular starburst system associated with a radio jet in the nearby cluster of galaxies Abell 194 (Fragile *et al.*, 2004). The mechanism proposed by Fragile *et al.* suggests that shocks generated by a galactic jet propagating through an inhomogeneous medium, such as a clumpy molecular cloud, can trigger the collapse of localized overdense regions, which then become active star-forming sites. Simulations of these high Mach number interactions show both the complexity of and need for coupled radiative, nonlinear hydrodynamics for shock-induced star formation. Given the enormous complexity of the coupled radiative, nonlinear hydrodynamics of these simulations, benchmark data are crucial, and now possible. Experiments under development today on HED facilities will be invaluable in the future in establishing benchmarks for this particularly difficult problem.

It is worthwhile mentioning that, in addition to the hydrodynamic phenomena discussed in this section, there exist a broad range of collisionless effects, which, in particular, are thought to be responsible for cosmic ray generation in supernova remnants. In principle, HED facilities might contribute to simulations of such phenomena (Drake, 2000), although experiments of this type remain rare to date (Woolsey *et al.*, 2001, 2002, 2004; Drake, 2002b; Courtois *et al.*, 2004; Gregory *et al.*, 2005).

VI. PROTOSTELLAR JETS AND HIGH MACH NUMBER FLOWS

Astrophysical jets present some of the most visually intriguing images that we encounter in the galaxy and

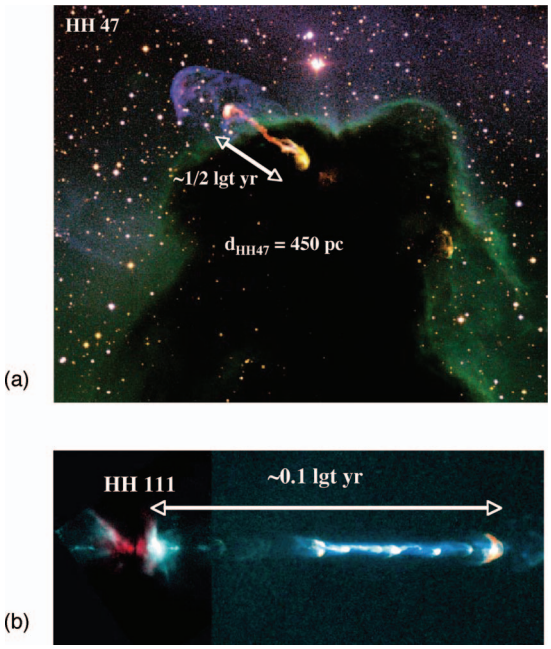

FIG. 24. (Color) Jets from young stellar objects in the galaxy. (a) Optical image of the protostellar jet, Herbig-Haro (HH) 47. The bipolar HH 47 complex embedded in the dense Bok Globule 1500 light years away at the edge of the Gum Nebula: (red) [SII] emission; (green) Hα; (blue) [OIII]. (b) Optical image of the jet, HH 111. Adapted from Reipurth and Bally, 2001.

universe (DeYoung, 1991; Reipurth and Bally, 2001). These jets cover an enormous range of spatial scale, from 10^{17} cm for jets from young stellar objects, as shown in Fig. 24, to 10^{24} cm for jets associated with quasars or active galactic nuclei harboring massive black holes (Birkinshaw and Davies, 1985; Chiaberge *et al.*, 2003). The class of stellar jets known as Herbig-Haro (HH) objects are thought to be collimated bipolar outflows emerging from accretion disks during the star formation process. Examples of a Herbig-Haro jets, HH 47 (Heathcote *et al.*, 1996) and HH 111 (Hartigan *et al.*, 2001), are shown in Fig. 24 (Reipurth and Bally, 2001). Typical velocities of HH jets are a few hundred km/s at densities of $n_{\rm jet}=10-100$ cm^{-3}. In terms of density contrast, it is thought that $\eta=n_{\rm jet}/n_{\rm ambient}\approx 10$, where $n_{\rm jet}$ and $n_{\rm ambient}$ are the jet and ambient number density, respectively (Morse *et al.*, 1992; Reipurth and Bally, 2001). High Mach number, high-density jets can be radiatively cooled, which greatly affects the dynamics and morphology (Blondin *et al.*, 1990; Stone and Norman, 1994; Frank *et al.*, 1998).

Models of jet formation generally fall into two broad categories. One category assumes that jets are formed as a consequence of matter falling into a compact central object from a magnetized rotating accretion disk (Pudritz and Norman, 1986; Lovelace *et al.*, 1993; Shu *et al.*, 1995; Livio, 1999). In the case of HH jets, the compact central object is the protostar or young stellar object. A second class of models assumes that the accretion process onto a central object results in a toroidal accretion disk, with density maximum along the equator and minimum at the poles, which define the symmetry (and rotation) axis. Spherically symmetric, outflowing winds from the central object then interact with this toroidal density profile, which leads to a funneling of the wind into bipolar jets following the rotation axis (Icke *et al.*, 1992). A variation on this is the formation of jets by convergence of supersonic conical flows, in particular, in the presence of strong radiative cooling (Tenorio-Tagle *et al.*, 1988). Observational data are insufficient at this time to conclusively discriminate between these classes of models, and indeed both may be operating simultaneously.

The jet internal Mach number [jet velocity/sound speed inside the jet, i.e., $v_{\rm jet}/c_s$(jet)] is one of the parameters used in describing jet dynamics and evolution. In astrophysical jets, the jet Mach number is generally very large, $M_{\rm jet}>10$. One effect of high Mach number on jet dynamics is to reduce the level of tip broadening due to Kelvin-Helmholtz instabilities in the working surface. An additional effect is to reduce the amount of mixing along the sides of the jet. These effects are illustrated by the three simulations show in Fig. 25(a) (Norman *et al.*, 1982). The effect of radiative cooling is even more dramatic (Blondin *et al.*, 1990; Stone and Norman, 1994; Xu *et al.*, 2000). Radiative cooling lowers the pressure inside the jet, leading it to compress further, increasing the collimation, such as shown by the simulations in Fig. 25(b) (Blondin *et al.*, 1990). As radiative cooling increases, as quantified by the cooling parameter $\chi=L_{\rm cool}/R_{\rm jet}$, the jet density and collimation increase. A fundamental question is how these jets remain so well collimated over propagation distances exceeding ~10 jet diameters or more (Reipurth and Bally, 2001). The effect of radiative cooling on jet morphology is still strong, even when magnetic field effects are included in the jet evolution, as shown in Fig. 25(c) (Frank *et al.*, 1998).

An emerging new experimental capability may prove useful in testing aspects of these models in addressing the collimation question. With the development of sophisticated high power lasers and magnetic pinch facilities around the world, the ability to conduct well-controlled and well-diagnosed laboratory experiments on high Mach number hydrodynamic jets is now becoming possible (Stone *et al.*, 2000). Laboratory experiments allow the effects of high Mach number, radiative cooling, and possibly magnetic fields on jet dynamics to be probed individually or in combinations (Shigemori *et al.*, 2000; Lebedev *et al.*, 2002; Foster *et al.*, 2005). The potential benefit of this research to astrophysics is only starting to be recognized and pursued.

One example, done on the Omega laser at the University of Rochester, is a purely hydrodynamic (nonradiative, nonmagnetic), high Mach number jet, shown at two different times in Figs. 26(a) and 26(b) (Foster *et al.*, 2002). In the experiment, a set of 12 laser beams at a total energy of ~6 kJ enters a cylindrical gold cavity (hohlraum) on one end through the laser entrance hole, and converts to x rays at or near the inner gold wall surface, generating a burst of radiation of temperature $T_r\approx 200$ eV, which lasts of order ~1 ns. A solid Al cy-

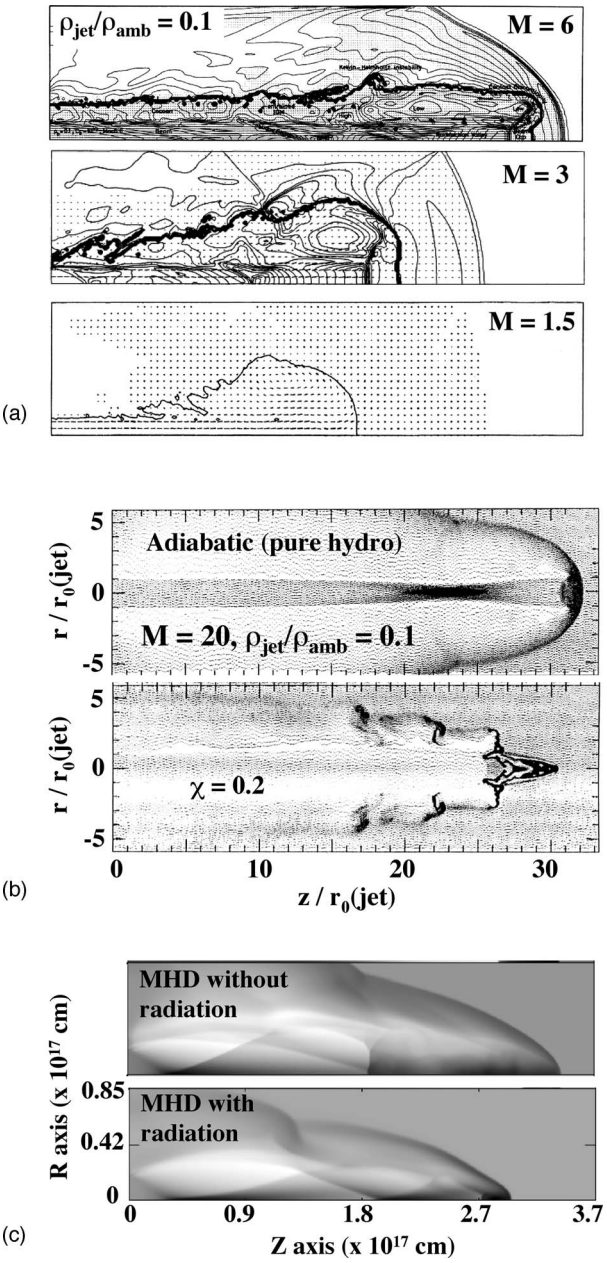

FIG. 25. Simulations of high Mach number jets relevant to HH jets. (a) Simulations showing the effect of Mach number in the jet morphology. Adapted from Norman *et al.*, 1982. (b) Simulations of high Mach number jets relevant to HH jets, showing the sensitivity to the amount of radiative cooling. Adapted from Blondin *et al.*, 1990. (c) Simulations showing the effect of radiative cooling on a high Mach number, magnetized jet. Adapted from Frank *et al.*, 1998.

lindrical plug of dimensions 200 μm diameter by 150 μm length is mounted on a hole on the wall of the hohlraum opposite the laser entrance hole, with 100 μm of the Al protruding into the hohlraum. This Al cylinder is butted up against a ~1-mm-long tube filled with a solid-density plastic (CH) reservoir. The radiation bath in the hohlraum ablatively launches converging shocks into the Al cylindrical plug. The magnitudes of the observed early-time jet and shock velocities suggest that an initial, very high-pressure region in the center of the Al cylinder, $P>100$ Mbar (i.e., 10^{14} dyne/cm^2), is created. The Al-CH interface at the entrance to the CH reservoir is at ambient pressure, hence the high internal pressure in the Al launches a high Mach number jet of Al moving axially down the CH tube. This jet is imaged radiographically, by generating a timed burst of hard x rays behind the target, and imaging the jet as a shadow (to "backlighter" x rays). This external source of backlighter x rays is generated by focussing several of the Omega beams onto an auxillary planar disk of material such as Ti, generating a bright source of He-α x rays at 4.7 keV. The jet shown in Fig. 26(a) has moved about three jet diameters, and a very prominent Kelvin-Helmholtz (KH) rollup is observed at the jet tip. The bow shock in the plastic is also very evident in these images. Simulations of the experiment are shown in Fig. 26(a), and the experimental data are in Fig. 26(b). The internal Mach numbers in these jets are $M_{\rm int}=v_{\rm jet}/c_s({\rm jet})\approx 3$, whereas the external Mach numbers are $M_{\rm ext}=v_{\rm jet}/c_s({\rm ambient})\approx 5$. The density ratio at the time of the images is $\eta=\rho_{\rm jet}/\rho_{\rm ambient}\sim 0.3$, due to the decompression of the Al, and the shock compression of the plastic. Once launched, these jets were purely hydrodynamic, with effects due to radiation being insignificant other than generating the initial ablation pressure source. For hydrodynamic jets such as these, a rigorous scale transformation can relate the laboratory experiments to the astrophysical setting. (See the scaling discussion in Sec. IV on supernova hydrodynamics.)

A scaled up version of this experiment has now been done on the *Z* magnetic pinch facility, and observed considerably later in time at 150 ns, as shown in Fig. 26(c) (Bennet *et al.*, 2004; Sinars *et al.*, 2004). This image used a bent spherical crystal, monochromatic imaging diagnostic to cast the image onto x-ray film and onto an image plate. Here, the high Mach number hydrodynamic jet has propagated 5–10 jet diameters, and still appears to be well collimated, and apparently reasonably laminar. Another approach using direct laser illumination to drive a shock that launches a jet of titanium through a collimator (acting like a microgun barrel) has been developed on the Omega laser, and backlit imaging out to several hundreds of ns has been demonstrated. An image from such a jet, using point projection imaging, is shown in Fig. 26(d) (Foster *et al.*, 2005). In this case, the jet tip or working surface displays an interesting appearance suggesting a transition to turbulence. Simulations done prior to these laser shots, one result of which is shown in Fig. 26(e), did indeed suggest that the jet evolution might transition into turbulence (Taylor *et al.*, 2004; Rosen *et al.*, 2005). Postshot simulations, compared with experiment, suggest that $\rho_{\rm j}\approx 0.1$ g/cm^3, $\rho_{\rm j}/\rho_{\rm a}\approx 1$, $T\approx 3$ eV, $v_j\approx 10$ km/s, $M_{\rm int}\approx 3$, ${\rm Re}\approx 10^6$, and ${\rm Pe}\approx 10^3$ for regions near the head of the primary jet at $t=300$ ns (Foster *et al.*, 2005). The primary jet is followed by a secondary jet, caused by the collapsing collimator ("gun barrel"). This secondary jet overtakes the primary jet causing a multitude of internal shocks and shock re-

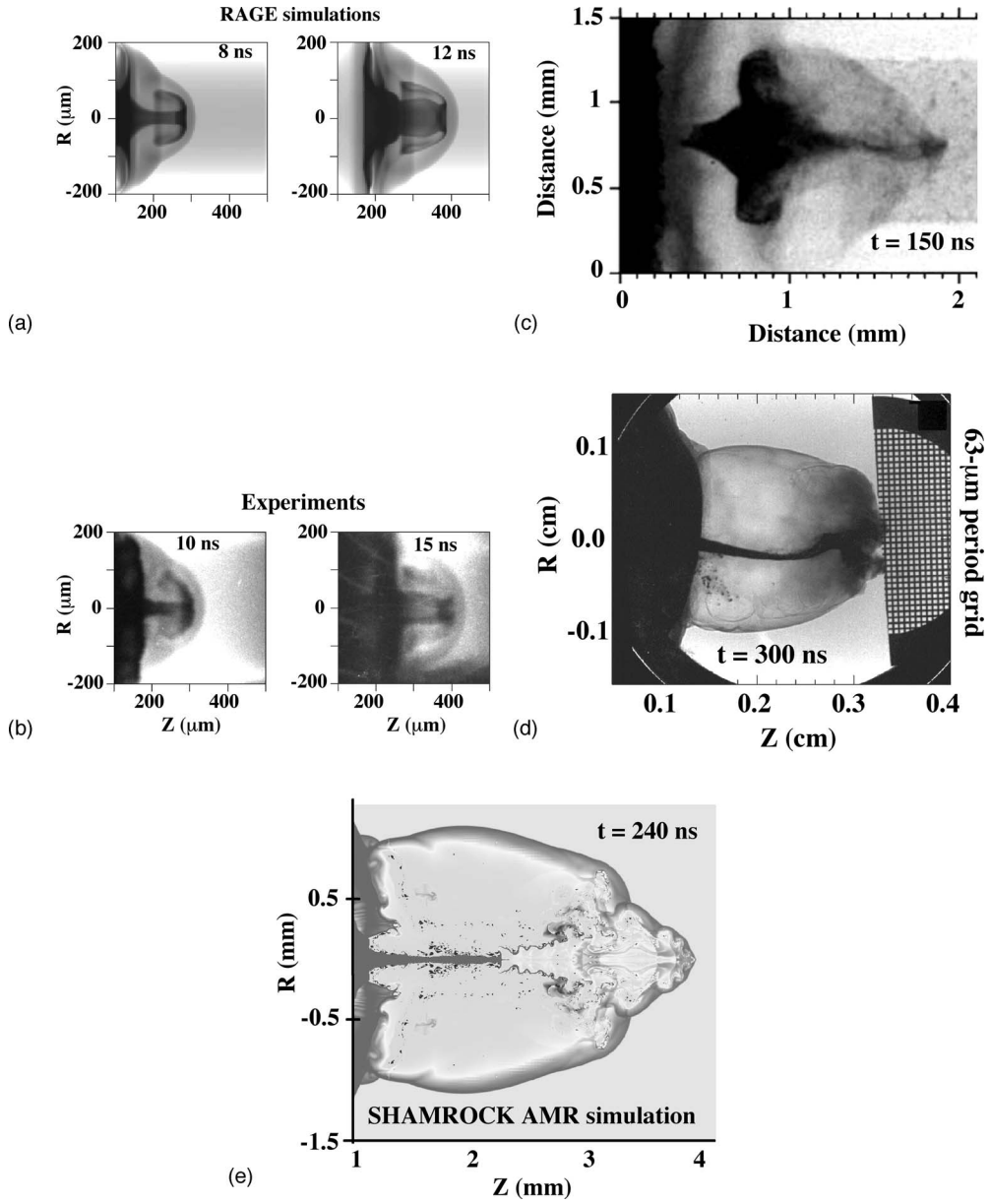

FIG. 26. Simulations and experiments of high Mach number jets on high power laser and *Z*-pinch facilities. (a) Simulations and (b) experimental images of a high Mach number, purely hydrodynamic (nonradiatively cooled) Al jet experiment done on the Omega laser. Adapted from Foster *et al.*, 2002. (c) High Mach number jet image taken on an experiment at the *Z* magnetic pinch facility. Adapted from Sinars *et al.*, 2004. (d) Image of a high Mach number jet driven by direct laser illumination of the target package, on the Omega laser, and backlit late in time, at 300 ns. Adapted from Foster *et al.*, 2005. (e) Simulation of the high Mach number turbulent jet, carried out prior to doing experiments, suggesting that the jet might indeed transition into turbulent hydrodynamics. Adapted from Taylor *et al.*, 2004.

verberations between the jet and bow shock. The behavior of grossly asymmetric (3D) jets has begun with the use of four beams (out of 192) at the National Ignition Facility (Blue *et al.*, 2005).

On the *Z*-pinch field facility Magpie, high Mach number jets were produced by applying fast-rising current, reaching 1 MA in 240 ns, to a conical array of fine metallic wires (Lebedev *et al.*, 2002). The resistive heating of the wires by current rapidly converts the outer surfaces of the wires to plasma, and through the $\mathbf{J}\times\mathbf{B}$ force, a fraction of this plasma implodes onto the axis. Due to the initial conical shape of the wires, the imploded "precursor" plasma has a net axial velocity component which turns the plasma stagnated on the axis into a jet. If the wires are high *Z*, such as tungsten, the jet is radiatively cooled, which increases its collimation and Mach number. Three jets thus produced with wire arrays of Al (little radiative cooling), Fe (moderate radiative cooling), and W (strongly radiatively cooled) are shown in Fig. 27(a) (Lebedev *et al.*, 2002). As the W precursor plasma stagnates on axis, the jet radiatively cools and remains well collimated as it emerges from pinch regions. This high Mach number jet can then be impacted into an ambient medium, such as a CH plasma target.

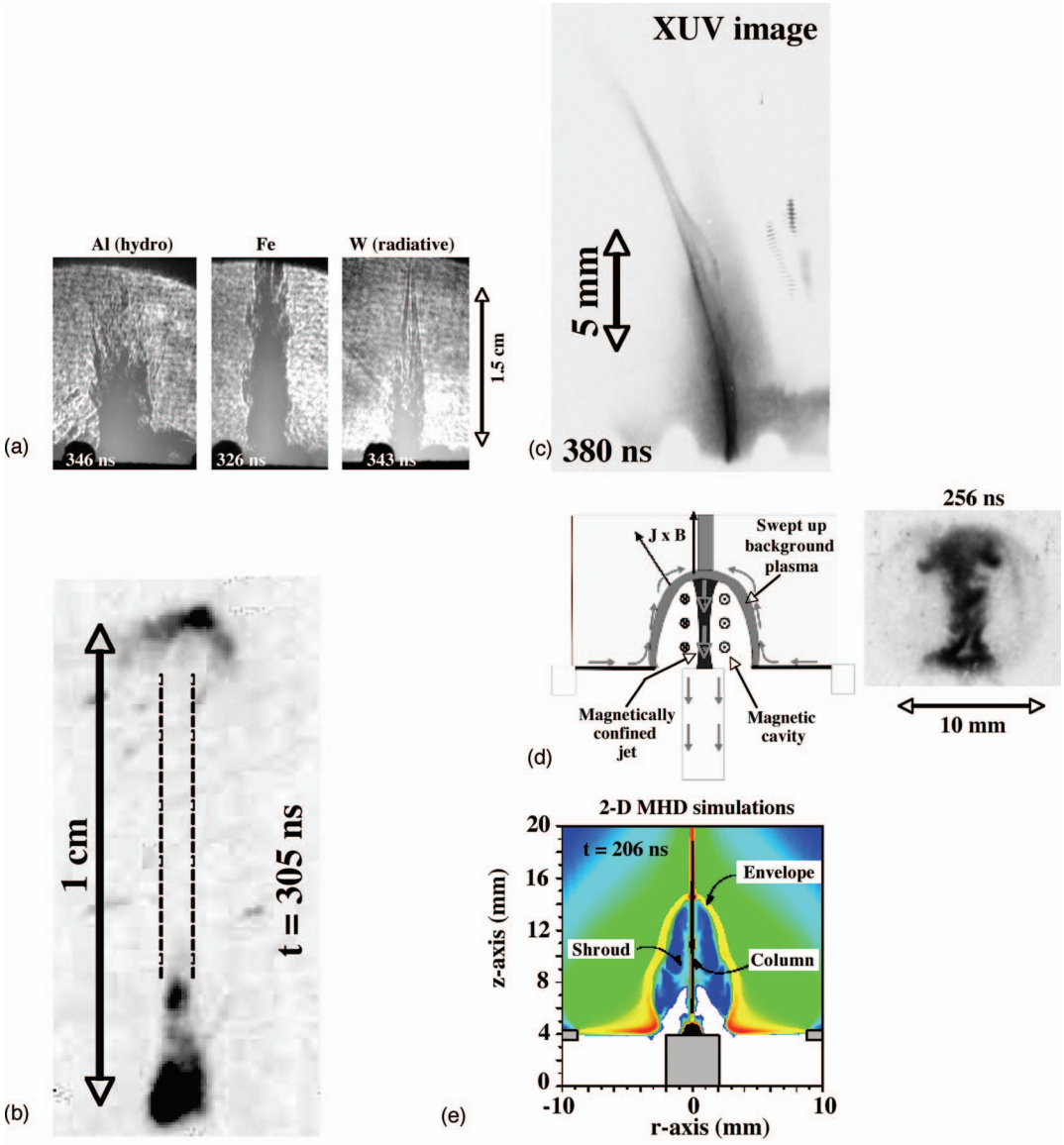

FIG. 27. (Color) Jet experiments and simulations from the Magpie magnetic pinch facility. (a) Images of jets of Al, Fe, and W plasma created by conical arrays of wires of the same material at the Magpie magnetic pinch facility. Adapted from Lebedev *et al.*, 2002. (b) Experimental image of a high Mach number, radiatively cooled W jet impacting a CH foil downstream, causing the working surface to reheat, and emit soft x rays. Adapted from Lebedev *et al.*, 2002. (c) Similar to (b), but this jet is being deflected transversely, due to the lateral flow of plasma (laboratory "stellar wind") impacting the jet, creating a lateral ram pressure. Adapted from Lebedev *et al.*, 2005b. (d) Images of a magnetic tower jet created by a radial wire array. Adapted from Lebedev *et al.*, 2004. (e) Simulations of a magnetic tower jet created by a radial wire array. Adapted from Ciardi *et al.*, 2005. These jet experiments were carried out on the Magpie *Z*-pinch facility.

During this impact the jet tip region (working surface) reheats and starts to radiate in the soft x ray again. An example of such an impact from jet experiments done on the Magpie pinch facility is shown in Fig. 27(b) (Lebedev *et al.*, 2002). Shown in Fig. 27(c) is the case where a radiatively cooled W jet is deflected sideways by a scaled "stellar wind," caused by ablating a suitably placed CH foil (Lebedev *et al.*, 2005b). Such jet deflections have been observed in some HH jets. Detailed images of the working surface of such jets have been obtained on the Magpie facility (Ampleford *et al.*, 2005).

An even newer development is the ability to create "magnetic tower" jets in the laboratory using a radial array of wires, instead of a cylindrical or conical array, as shown in Fig. 27(d) (Lebedev *et al.*, 2005a, 2005b). Such magnetized, high Mach number jets resemble aspects of magnetically formed protostellar jets, and thus add one more capability to the techniques available to study jet dynamics in the laboratory. The radial flow of current converges to the center then runs axially down the stem or stalk. The net magnetic forces cause the radial wire "sheet" to bulge upwards. Once the wires "break," the magnetic cavity expands and rises. This is illustrated schematically on the left side of Fig. 27(d). An image in x-ray emission for an experiment where the radial wires were W is shown on the right side of Fig. 27(d). Simula-

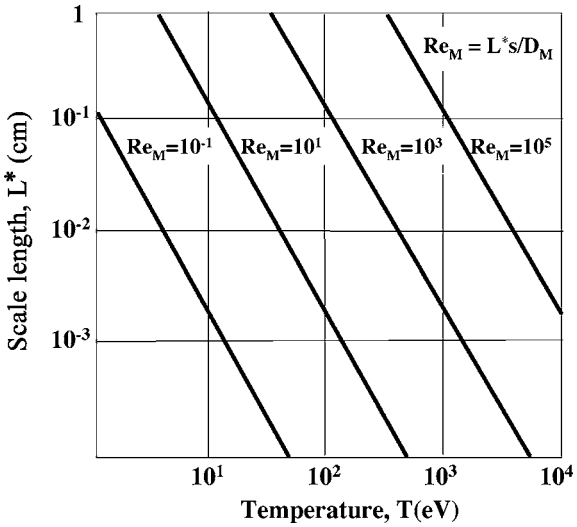

FIG. 28. Lines of constant magnetic Reynolds number Re_M =const for a fully stripped carbon plasma as a function of the characteristic length scale and temperature. Adapted from Ryutov *et al.*, 2001.

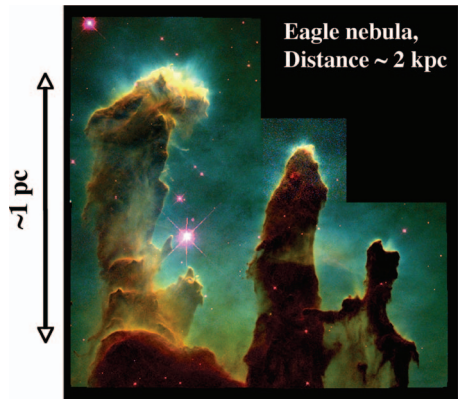

FIG. 29. (Color) The Hubble Space Telescope image of the Eagle Nebula. Radiation is absorbed in a very thin layer near the surface of the cloud. Adapted from Hester *et al.*, 1996.

tions show in detail the dynamics and conditions of these laboratory high Mach number magnetic tower jets, an example of which is shown in Fig. 27(e) (Ciardi *et al.*, 2005). Based on comparison of simulations with experiment, it is estimated that the Mach number of the magnetic cavity in the axial direction is $M\sim 10$ and in the central jet column $T\sim 120$ eV, $Z\sim 20$, $\beta=P_{\mathrm{thermal}}/P_{\mathrm{magnetic}}\sim 1$, and $\mathrm{Re}_M\sim 10$ (Lebedev *et al.*, 2005a).

In order to experimentally simulate aspects of the magnetohydrodynamics of astrophysical jets, the magnetic Reynolds number Re_M in the laboratory experiment must be at least an order of magnitude higher than 1. Recall that $\mathrm{Re}_M\equiv sL^*/D_M$, where D_M is the magnetic diffusivity, s is the sound speed, and L^* is the characteristic length scale in the laboratory experiment (Ryutov, Drake, and Remington, 2000). Under typical astrophysical conditions, Re_M is extremely large, due to the large spatial scales involved. For example, for a hydrogen plasma at a temperature of ~0.1 eV, and at the scale typical for Herbig-Haro jets ($L^*\sim 10^{17}$ cm), Re_M is of the order of 10^{15}. Reaching such values of Re_M in laboratory experiments with laser-driven or Z-pinch-driven targets is very difficult if not impossible. On the other hand, reaching values of $\mathrm{Re}_M\gg 1$ may be possible (Fig. 28). A key parameter is the plasma temperature. [Note that there is a factor of 10 error in Eqs. (19) and (20) of Ryutov, Drake, and Remington (2000), where the analogous figure was first presented: the right-hand side of Eq. (19) is actually ten times smaller, and the right-hand side of Eq. (20) is ten times larger. Therefore our Fig. 28 here is somewhat different from Fig. 1 of that paper or Fig. 3 of Ryutov *et al.* (2001).] As an example, consider ~$(1\ \mathrm{mm})^3$ of plasma. At a temperature of $T\sim 10$ eV, the magnetic Reynolds number would be $\mathrm{Re}_M\sim 10$, whereas the same $(1\ \mathrm{mm})^3$ of plasma at 100 eV would have $\mathrm{Re}_M\sim 10^3$. This increase is because $\mathrm{Re}_M\sim sL/D_M$, where sound speed $s\sim T^{1/2}$ and $D_M\sim 1/T^{3/2}$ (Ryutov, Drake, and Remington, 2000). Hence $\mathrm{Re}_M\sim LT^2$. So at a factor of 10 higher temperature, Re_M increases by a factor of 100, from Re_M of ~10 to ~10^3. This suggests that a possible direction for research on next generation, high power HED facilities such as NIF or ZR could be to generate hotter hydrodynamics conditions to increase Re_M well beyond ~10, where magnetic-field effects could start to play an interesting role in coupling to the evolution of turbulent hydrodynamics.

VII. HYDRODYNAMICS OF PHOTOEVAPORATED MOLECULAR CLOUDS

A. Introduction

Cold gaseous clouds illuminated by neighboring bright massive stars may experience an intense ablation of material from their surfaces. The UV radiation from stars is absorbed by photoionization and photodissociation processes near the surface of the cloud, causing a continuous ablation of surface layers and generating a flow of ionized gas directed away from the surface of the cloud. This process, first discussed by Oort (1953), Spitzer (1954), and Oort and Spitzer (1955), is commonly called "photoevaporation." One of the best-known objects of this type is the Eagle Nebula (White *et al.*, 1999). Figure 29 shows the Hubble space telescope (HST) image of this object and Fig. 30 shows its orientation with respect to the nearest young stars. Long pillars visible in the picture are sometimes called "elephant trunks" (Frieman, 1954). Other examples of photoevaporation flows have been found; see, e.g., Leung (1985) and Pound *et al.* (2003). Detailed studies of the ionization front dynamics have been carried out by Kahn (1954, 1958), who laid the groundwork for classifying various possible regimes, as well as Dalgarno and McCray (1972) and Bertoldi (1989), who produced a comprehensive analysis of the process with a detailed account of ionization and recombination processes. Dense molecular clouds in the vicin-

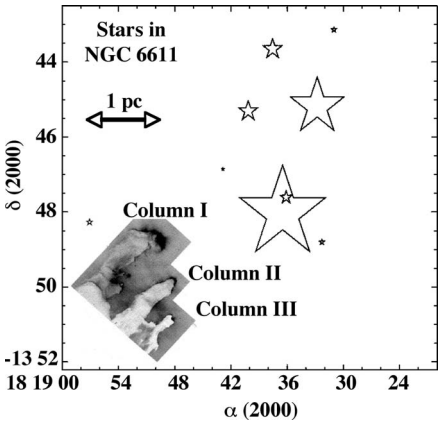

FIG. 30. The projection of the Eagle Nebula and neighboring stars on the plane of the sky. From Pound, 1998. The size of the symbols indicates the relative strength of the Lyman continuum flux. Adapted from Pound, 1998.

ity of bright young stars are of broader interest because these clouds may serve as "cosmic nurseries," where star formation occurs (Shu *et al.*, 1987; Elmegreen, 1998; Sugitani *et al.*, 2002).

In recent years, detailed information about the physical conditions in both the hot ionized flow and cold gaseous cloud in the Eagle Nebula has been obtained. The hot ionized part was characterized by Hester *et al.* (1996) on the basis of Hubble Space Telescope observations in Hα, [SII], and [OIII] lines. Imaging of the cold interior of the cloud at millimeter- and submillimeter-range wavelengths (emitted by molecules of the cold gas) was carried out by Pound (1998) and White *et al.* (1999). Levenson *et al.* (2000) have characterized the photodissociation zone as well as parameters of the ionized matter. These data make possible a much more detailed analysis of the physics processes responsible for the formation of visible structures. In particular, hydrodynamic velocities inside the cold gas have been found by Pound.

Below we discuss hydrodynamic phenomena occurring during photoevaporation of gas clouds, with the main emphasis made on possible instabilities of the cloud surface. We argue that a significant part of the problem can be correctly described in the framework of ideal hydrodynamics and modeled in scaled experiments.

B. Main physical processes

It has been realized many years ago (Spitzer, 1954) that complex hydrodynamic motion and, eventually, the shape of photoevaporated clouds is largely determined by the ablation force arising from the intense photoevaporation. Molecular clouds are typically quite cold: the balance of heating the cloud material by cosmic rays and radiation cooling in the microwave range (Spitzer, 1978) establishes an initial (preshock) temperature of only ~30 K. Ultraviolet radiation of bright young stars is absorbed in a very thin layer near the cloud surface by photoionization and photodissociation of hydrogen. The ionized gas thus formed begins to expand away from the cloud surface. The pressure from the "rocket effect" then compresses the cloud. Typical ablation pressures are orders of magnitude higher than the initial pressure of the cold cloud interior. A strong shock is launched into the cloud, compressing and heating it. Once the shock wave has traversed the cloud, a rarefaction wave from its far surface travels back to the front surface, after which the whole slab is accelerated. For the Eagle Nebula, the time scale for these developments is $\sim 10^5$ yr and is comparable to the time scale inferred by Pound (1998) to develop the structures.

The properties of the material in the Eagle Nebula have been determined by Hester *et al.* (1996), Pound (1998), and Levenson *et al.* (2000). They are discussed by Ryutov and Remington (2002) and are summarized in Table II. In addition, Pound determined that the velocity difference between the heads and bases of the pillars is $\Delta v \sim 10^6$ cm/s, implying that the characteristic acceleration g of the cloud material is $g \sim (\Delta v)^2/L \sim 3 \times 10^{-7}$ cm/s^2.

One can readily show that the hydrodynamic description applies to these objects. The mean free path λ of H_2 molecules is determined by molecular collisions with a cross section $\sim 2 \times 10^{-16}$ cm^2. For the density as in Table II, one has $\lambda \sim 10^{11}$ cm, many orders of magnitude less than any other characteristic dimension of the cloud. The Reynolds number for motions on the scale L is very large $\mathrm{Re} \sim 10^7 - 10^8$. The viscous effects at the scales of interest are therefore unimportant. The particulate heat transport is also negligible. We therefore conclude that the interior of the gas cloud can be adequately described by the inviscid hydrodynamics.

TABLE II. Parameters of the Eagle Nebula and possible simulation experiment

Parameter	Notation	Numerical value in the Eagle Nebula	Numerical value in the experiment
Characteristic length scale	L	3×10^{18} cm	6×10^{-3} cm
Average density of the cloud	ρ	1.5×10^{-19} g/cm^3	2 g/cm^3
Ablation pressure	p_a	5×10^{-9} dyn/cm^2	10^{13}
Density of the ablation flow	ρ_a	3×10^{-21} g/cm^3	0.02 g/cm^3
Temperature in the ablation flow	T_a	1 eV	10 eV
Velocity of theablation flow	v_a	2×10^6 cm/s	5×10^6 cm/s

In the ablative flow, which is almost totally ionized, the collisional mean free path is determined by Coulomb collisions, which at a temperature ~1 eV have a cross section $\sim 3\times 10^{-13}$ cm^2. Therefore, despite a smaller density, the collisional mean free path λ_c in the ablation flow is very small: $\lambda_c \sim 3\times 10^9$ cm for density of $n_a \sim 10^3$ cm^{-3}. Therefore the particulate heat and momentum transport are both negligible here. One can check that radiation losses from the ionized low-density gas are also small.

Despite being quite cold, molecular clouds are electrically conducting, because of finite (albeit small) ionization. This ionization is nonthermal, it is produced by cosmic rays for which clouds are transparent. A substantial fraction of electrons are probably attached to dust grains (which are present in cold clouds). Estimates of the degree of ionization for conditions typical for the Eagle Nebula yield the value $\sim 3\times 10^{-8}$ (Elmegreen, 1979). The magnetic Reynolds number turns out to be very large (Ryutov and Remington, 2002).

Detailed estimates of radiation losses from molecular clouds have been done by Neufeld *et al.* (1995). Basically they showed that the cooling time, defined as the ratio of the thermal energy density to the power radiated from a unit volume, is very short, of order of 100–1000 yr. This means that the shocked material cools down very quickly, orders of magnitude quicker than it takes for the shock to traverse the cloud ($\sim 10^5$ yr). This brings up a paradox. Because of strong radiation cooling, the shocked material must collapse to a high density to maintain pressure balance, $nT = p_{\rm abl}$, at a low temperature ($T \sim 3\times 10^{-3}$ eV). This yields a density $n \sim 3\times 10^6$ cm^{-3}, which directly contradicts observed values.

Several solutions to this paradox have been proposed: the effect of ram pressure from a small-scale turbulence; the presence of a quasihomogeneous magnetic field; the presence of small-scale MHD turbulence; and the presence of force-free, random, static magnetic field. The latest discussion of these models was by Ryutov *et al.* (2004, 2005), where references to earlier models can be found. The present authors assume that one or a combination of these effects restores a hydrodynamic picture of the shock-compressed gas, with some effective adiabatic index.

There are multiple time scales involved in this problem. As pointed out by Pound (1998), there is a characteristic time scale for hydrodynamic motion $\tau_{\rm dyn} \sim (\Delta v')^{-1}$, where $\Delta v'$ is the velocity shear inside the cloud. According to Pound, $\tau_{\rm dyn} \sim 3\times 10^{12}$ s $\sim 10^5$ yr. The significance of this is that it establishes the maximum time that has passed since this shear motion began: At times much greater than $\tau_{\rm dyn}$, the cloud would have become much larger than we actually see it. In this sense, the time $\tau_{\rm dyn}$ sets the upper limit for the time when the photoevaporation began (when the nearby O-type stars have "turned on"). It was noted by Pound that the time $\tau_{\rm dyn}$ is much shorter than the evolutionary time of the typical O-type star ($\sim 10^7$ yr). Therefore we are witnessing a very early stage of the photoevaporation process. This is a very important circumstance, because it points at a possibility that stars are still in a transient stage of their formation, and their luminosity may have varied significantly during the past 10^5 yr. Such variations, including nonmonotonic variations, with the luminosity passing through a maximum are a common phenomenon in the evolution of very young stars (e.g., Iben and Talbot, 1966; Cohen and Kuhi, 1979).

The time scale for photoevaporation to remove a considerable amount of the initial molecular hydrogen is much longer: $\sim 10^7$ yr. In other words, the loss of cold gas from the molecular cloud due to photoevaporation up to the present time is very small.

C. Hydrodynamic models of the formation of the elephant trunks

There exist several models that attempt to explain the origin of the pillars in the Eagle Nebula. The earliest one was suggested by Spitzer (1954) and is based on the observation that after the shock breaks out at the back side of the cloud and the resulting rarefaction wave reaches the front side, the cloud as a unit begins to accelerate. This drives the Rayleigh-Taylor instability at the ablation front (remember that $n_{\rm abl} \ll n$). The pillars are then identified with the familiar "spikes" of a heavy fluid penetrating through the light fluid (Frieman, 1954).

We note that if the intensity of UV radiation grows with time, the interface will be accelerated into the cloud even before the return of the rarefaction wave to the front surface. This would allow the early onset of the RT instability. Generally, the possible effects of the temporal dependence of the ionizing radiation have not been studied in any detail.

Another popular model relates the formation of the pillars to the assumed presence of the preexisting dense "clumps," whose density is substantially higher than the density of the surrounding cloud. The ablation pressure is unable to move these heavy clumps, which stay, roughly speaking, at their initial places, and shadow the cloud material downstream. Then, whereas the rest of the cloud is moved over a significant distance by the ablation pressure, the shadowed parts remain static, giving rise to the pillar structure. This process has been studied numerically by Williams *et al.* (2001).

A third possible model is that pillars are formed from the gas evaporated from stand-alone dense clumps situated in front of the gaseous cloud. A part of the clump material is pushed by the ablation pressure away from the radiation source, forming a cometary-like structure (Bertoldi, 1989; Bertoldi and McKee, 1990; Lefloch and Lazareff, 1994), whence a name "cometary model." The long tail eventually reaches the cloud and mixes with it, making the whole structure very similar to the one observed.

D. Laboratory experiments

Provided that our conclusion regarding the applicability of ordinary compressible hydrodynamics for the de-

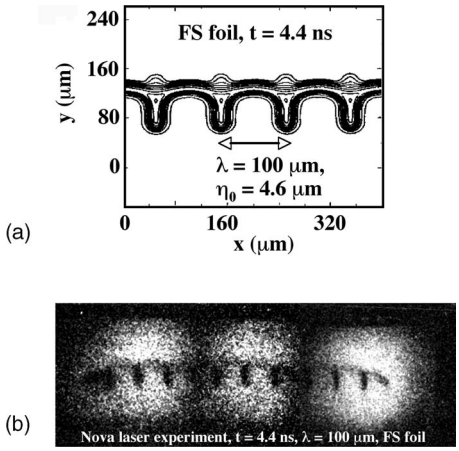

FIG. 31. Results of (a) a simulation and (b) an experiment on the ablation front Rayleigh-Taylor instability. Perturbations are viewed side-on at 4.4 ns. The ablation front corresponds to the lower side of the material. The initial wavelength was 100 μm and the initial peak-to-valley variation was 4.6 μm. Three nearly simultaneous gated x-ray pinhole images are juxtaposed. Due to the ~100 μm of parallax differences between the views, the full extent of the foil is observed. Adapted from Remington *et al.*, 1993.

scription of the cloud interior is correct, one can simulate, in a scaled fashion, any of these models. Experiments using x-ray irradiation from hohlraums seem to be more relevant than experiments based on a direct laser irradiation of the target, since experiments of the first type involve the direct photoevaporation of the material by x rays. It also matters that the density of the material in the ablation flow is at least an order of magnitude less than the density of the underlying material. Experiments of the second type ("direct drive" experiments, Sec. II) are less relevant to astrophysical photoevaporation fronts, because they introduce complications not present in astrophysical systems. Specifically, the absorption zone for the laser radiation is spatially decoupled from the ablation zone, with heat being transported between these two regions by electron heat conduction. Additional complications involving laser-plasma interactions are also possible (Kruer, 2000).

Because of the importance of Rayleigh-Taylor instabilities at ablating surfaces to inertial confinement fusion, there have been many experiments related to this subject. The first paper on this subject was that by Remington *et al.* (1993). Weber *et al.* (1994) carried out an exhaustive study of radiation transport and ablation front structure for conditions close to those of these experiments. The density of the ablated material was small compared to the density of the initial foil. Absorption in these experiments occurs in a relatively narrow layer, as is the case in the Eagle Nebula. Ablative stabilization (see below) plays a role only for short wavelengths, $\lambda < 10$ μm, whereas the range of wavelengths studied was up to 150 μm. It is interesting to note that the structure of well-developed RT perturbations observed by Remington *et al.* (1993) (Fig. 31) is very similar to the elephant trunks observed in the Eagle Nebula. Although the experiment was not optimized to have scaled parameters relevant to the Eagle Nebula, it certainly has produced relevant results, somewhat by serendipity. Comparison of the parameters of the Eagle Nebula with those of this laboratory experiment is presented in Table II.

Note that the so-called "ablative stabilization" was insignificant in both the laboratory experiment and its astrophysical counterpart. The underlying qualitative explanation of this stabilization mechanism is that the Rayleigh-Taylor perturbation is localized in a layer of thickness $\sim\lambda/2\pi$ near the surface, so that if the ablation front "consumes" or burns off a layer of thickness $\sim\lambda/2\pi$ of the fluid within a time interval shorter than the instability e-folding time, a considerable reduction in the growth rate, compared to $\gamma_{\mathrm{RT}}=(2\pi g/\lambda)^{1/2}$, occurs. In other words, ablative stabilization becomes significant when $v_a > (\rho_a/\rho)(g\lambda/2\pi)^{1/2}$, where v_a is the velocity of the ablative flow and we ignore a numerical factor of order unity; see surveys by Lindl (1995) and Takabe *et al.* (1999), for more detail and further references. Using the numbers of Table II, one finds that, indeed, the ablative stabilization is unimportant for the wavelengths of interest.

For completeness, we mention that ablation front RT instability has also been studied in extensive detail in direct drive (Azechi *et al.*, 1997; Knauer *et al.*, 2000).

E. Issues for experiments and theory

There exist several additional effects that have to be properly factored into the theory, numerical simulations, and experiment in order to produce a more complete picture of the real photoevaporation front phenomenon.

The first effect is related to absorption of incident radiation in ablation flow. Absorption is caused from the small fraction of electrons and ions that recombine, producing neutral hydrogen atoms which absorb ionizing radiation. Depending on the specifics of the geometry, this effect may be quite substantial. Kahn (1958) argued qualitatively that absorption of incoming radiation by hydrogen atoms formed by recombination in the ablation outflow can have a stabilizing effect, because of the stronger absorption near the dimples of the surface relief compared to the bumps. Axford (1964) presented a quantitative study that showed that this stabilization mechanism is most effective for perturbations larger than the recombination length. Sysoev (1997) provided a more complete analysis. Williams (2002) confirmed it and included the effects of radiation tilt. These papers dealt with the situation of a nonaccelerated ablation front. In a more recent study by Mizuta *et al.* (2005a, 2005b), both effects of acceleration and radiation absorption were included. It turned out that the linear RT instability, for the characteristic parameters of the Eagle Nebula, is stabilized by radiation absorption in the ablated plasma for concave surfaces, causing a "self-annealing" effect of any small ripples in the cloud surface. On the other hand, nonlinear perturbations may continue to grow. These results are illustrated in Fig. 32.

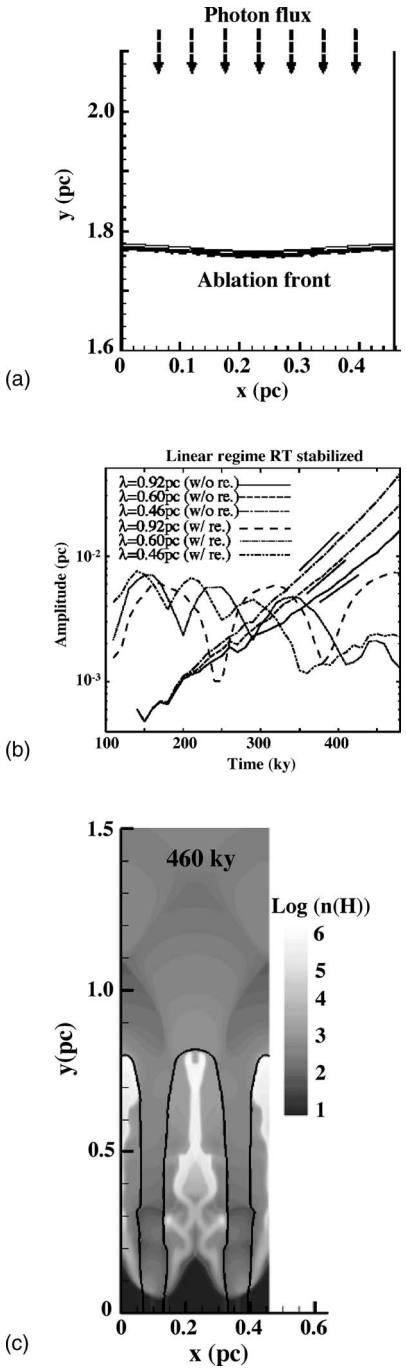

FIG. 32. Numerical simulations accounting for the absorption of the ionizing radiation in the ablation outflow. (a) The initial perturbation on the cloud surface. (b) This panel shows that when the absorption is artificially turned off the amplitude of perturbations grows approximately according to the Rayleigh-Taylor model. If the absorption is "turned on," however, the exponential growth is replaced by a damped oscillation. (c) The 2D simulation result showing that *nonlinear* perturbations can grow even in the presence of absorption. Adapted from Mizuta *et al.*, 2005b.

Figure 32(a) shows the initial configuration for the simulation, and the RT-stabilized dynamics in the linear regime calculation is shown in Fig. 32(b). A simulation with larger initial perturbation is shown in Fig. 32(c). Once the curvature exceeds a critical value, the RT instability "wins out" over the self-annealing effect, and ripples grow into the deep nonlinear regime, resembling pillars in the Eagle Nebula.

In the aforementioned experiment by Remington *et al.* (1993), the parameters of the ablation flow were such that absorption of incident radiation was insignificant. On the other hand, by a proper choice of dopants it may be possible to reach conditions where absorption of radiation in the outflow would be similar to that in the Eagle Nebula outflow. This would then open a possibility to experimentally assess the effect of absorption on both the linear and the nonlinear stage.

The second additional effect is produced by noting that the incident ionizing radiation may be tilted with respect to the surface of the ablation front. The perturbation of the ablation pressure will then be different on the two slopes of a small-amplitude sinusoidal surface wave, leading to the excitation of this wave as a traveling wave. This effect was studied for nonaccelerated clouds by Vandervoort (1962) and, more recently, by Williams (2002). Ryutov *et al.* (2003) have included both the effect of acceleration and the tilt and predicted that, in the nonlinear regime, an effect similar to the breaking of the waves on the ocean surface may occur. This phenomenon can be experimentally studied in an asymmetrically radiated hohlraum, where there will be an asymmetry in the radiation flux (Ryutov and Remington, 2002).

The third effect is related to that situation where radiation from a distant star in the location of the cloud has a narrow angular distribution. Kane has found that this may introduce new features to the development of small-scale perturbations of the ionization front (Kane *et al.*, 2005). This effect can also be studied with the use of a hohlraum technique, by placing the target outside the hohlraum, far enough from the hole in the hohlraum wall, so that the radiation would become strongly collimated.

As summarized in this section, the dynamics and evolution of photoevaporated molecular clouds is controlled by a wide variety of external parameters. Experiments carried out in the simplest setting (weak absorption in the blow-off plasma, no tilt) have demonstrated that structures strongly resembling elephant trunks can indeed be formed as a result of the ablation front Rayleigh-Taylor instability. This supports the viewpoint of astrophysicists that ablation front dynamics is key to understanding the shape and evolution of such objects. An assessment presented above shows that there is a possibility to include other effects and make scaled laboratory experiments much more realistic in reproducing the dynamics of real systems. These more sophisticated experiments will hopefully be carried out within a few years.

VIII. PLANETARY INTERIORS AND EQUATIONS OF STATE

The interior structure of the giant planets of our solar system (Jupiter, Saturn, Uranus, and Neptune) is deter-

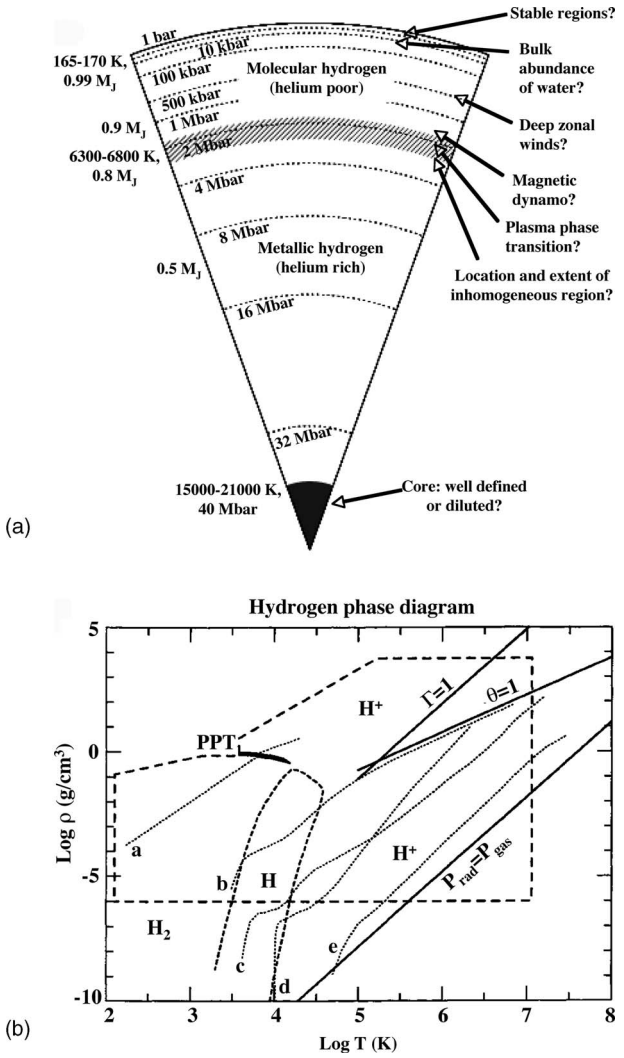

FIG. 33. The interior structure of Jupiter is sensitive to the high pressure, high density properties of hydrogen. (a) Schematic of the interior of Jupiter. Adapted from Guillot *et al.*, 2004. (b) Phase diagram of high-pressure hydrogen. Reproduced from Saumon *et al.*, 1995. Curve *a* corresponds to the interior of Jupiter. Curves *b*, *c*, and *e* represent the interiors of main sequence stars of mass 0.3, 1.0, and $15M_{\odot}$, respectively. Curve *d* corresponds to the hydrogen envelope of a white dwarf. The heavy solid line labeled PPT represents the predicted plasma phase transition.

mined by the compressibility of their constituent matter under high pressures due to the inwardly directed force of gravity (Guillot, 1999; Guillot *et al.*, 2004). In laboratory terms, this compressibility is determined by the equation of state (EOS) of the constituent matter along an isentrope (Saumon and Guillot, 2004). The EOS and other properties of matter at the extreme pressures and densities found in the interiors of the giant planets, however, are uncertain. The pressures of interest along an isentrope range from 1–8 Mbar in Uranus and Neptune (Hubbard, 1997), 1–40 Mbar in Saturn, to 1–70 Mbar in Jupiter (Guillot, 1999), as shown for Jupiter in Fig. 33(a) (Guillot *et al.*, 2004).

Characteristic isentropes for the giant planets indicate that the plasma in their interiors is both strongly coupled, with $\Gamma=(Ze)^2/aT>1$, where Z, e, a, and T correspond to ionization state, electron charge, average atomic spacing, and temperature (in units of energy), and degenerate, meaning $\theta=T/\varepsilon_F<1$, where ε_F is the Fermi energy (Van Horn, 1991). This is shown for Jupiter, as well as for a brown dwarf and a low-mass star, in the phase diagram of hydrogen in Fig. 33(b) (Saumon *et al.*, 1995, 2000). The compressibility of hydrogen along a high-pressure isentrope and the predicted phase separation in a He-H mixture when hydrogen transitions to a metallic state are of central interest both for the giant planets of our solar system and for models of the extrasolar planets (Fortney *et al.*, 2004). Also shown in the pressure-temperature plot of hydrogen in Fig. 33(b) are curves of $\Gamma=1$ and degeneracy $\theta=1$, showing strongly coupled Fermi degenerate conditions. Given the large theoretical uncertainties, experimental data on the high-pressure EOS, phase, and conductivity of hydrogen is needed, to guide the testing and refining of interior models of Jupiter and Saturn.

The giant ice planets Uranus and Neptune also have significant uncertainties in our understanding of their interior structures. They are thought to consist of a gaseous atmosphere, a rocky core, and a thick intermediate ocean of hot H_2O (water), NH_3 (ammonia), and CH_4 (methane) in a dense liquid phase customarily referred to as "ice" (Hubbard, 1997; Cavazzoni *et al.*, 1999). Pressures and temperatures in the ice layer range from 20 to 600 GPa and 2000 to 7000 K, respectively, as shown in Fig. 34(a). Many of the observable quantities of the giant ice planets, such as gravitational moments, atmospheric composition, and magnetic field, are thought to be determined by the properties and conditions within the ice layer. There are large uncertainties in our understanding of how the magnetic fields of Neptune and Uranus are formed. In particular, experimental data are needed on the conductivity of water, methane, and ammonia at $P>100$ GPa, before models of the origin of their magnetic fields can be firmed up.

The phase diagram of high-pressure water, shown in Fig. 34(b), has large uncertainties. Starting at low temperature, water will be in the solid ice state, and depending on pressure, this can have several different phases (Cavazzoni *et al.*, 1999). At high pressure $P>100$ GPa, as the temperature is increased to $T\gtrsim 2000$ K it is thought that a transition occurs to a solid, superionic state, where oxygen atoms maintain a crystalline body-centered-cubic (bcc) lattice structure, but protons can readily diffuse. This makes this solid-state material an ionic conductor but electronic insulator. As the temperature is further increased to $T\gtrsim 3500$ K, the oxygen sublattice also melts, and a two-component ionic liquid (molten salt) is formed, which again is an ionic conductor but electronic insulator. Finally, above 7000–7500 K, water is thought to become a metal, that is, the electronic band gap closes, $E_{\rm gap}/kT<1$. Experimental data on the high-pressure EOS, phase, and conductivity of

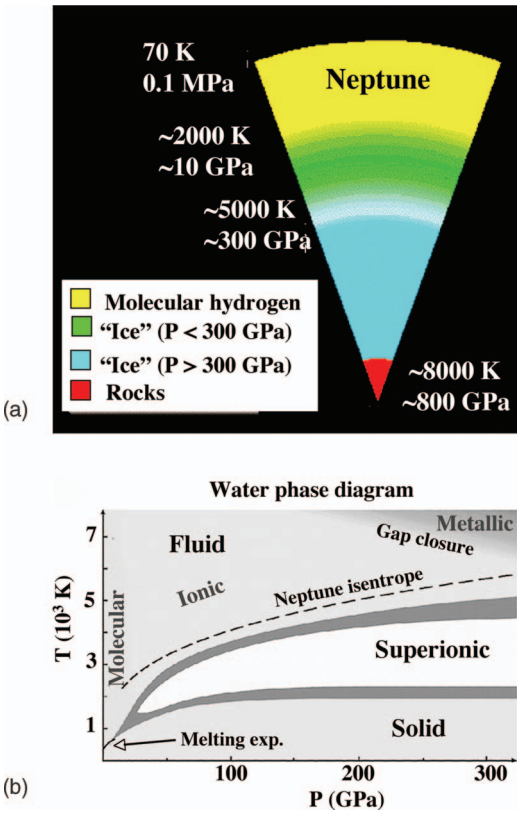

FIG. 34. (Color) The interior structure of Neptune is sensitive to the high pressure properties of water. (a) Schematic of the interior of Neptune. Reproduced from Hubbard, 1997. (b) Phase diagram of high-pressure water. Adapted from Cavazzoni *et al.*, 1999.

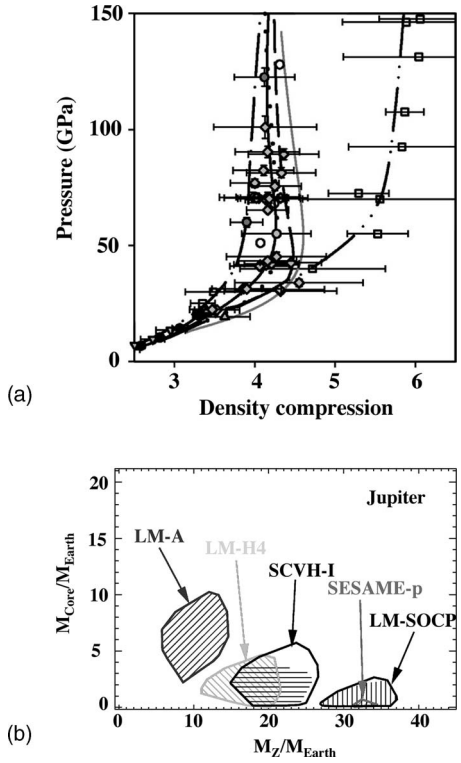

FIG. 35. Models used to predict the interior structure of Jupiter are tested with strong shock experiments. (a) Summary plot of recent high-pressure shock Hugoniot measurements of D_2. Adapted from Knudson *et al.*, 2004. (b) Plot showing the sensitivity of calculations of the interior of Jupiter to the models of the high-pressure EOS of hydrogen. Adapted from Saumon and Guillot, 2004. Different curves correspond to the following models. LM-A: Modified Ross linear mixing model. LM-H4: Linear mixing, with D_4 chains, D_2 molecules, and a $D^+ + e^-$ fluid metal. LM-SOCP: Ross linear mixing model, only with the one component plasma (OCP) replaced with a screened OCP for the metallic (atomic) fluid free energy. SCVH-I: The Saumon-Chabrier, Van Horn EOS. SESAME-p: original SESAME, patched to better reproduce data in the molecular regime for $P < 0.2$ Mbar.

water are needed to allow theoretical progress to be made on interior models of Neptune and Uranus. Fortunately, experimental progress has been made on the high-pressure properties of both hydrogen and water.

A summary of recent experimental measurements of the shock-driven EOS of D_2 at ~1 Mbar pressures is given in Fig. 35(a) (Knudson *et al.*, 2004). Achieving ~Mbar pressures in these cryogenic hydrogen experiments is very difficult. The results from four different techniques are shown in Fig. 35(a), corresponding to experiments done on a gas gun (Holmes *et al.*, 1995), the Sandia Z facility (Knudson *et al.*, 2003), a spherically convergent, high-explosive-driven experiment (Belov *et al.*, 2002; Boriskov *et al.*, 2005; Trunin *et al.*, 2005), and the Nova laser (Collins *et al.*, 1998). The gas gun, *Z*, and high-explosive results all more or less agree with each other. The gas gun and *Z* experiments both used the impedance matching technique that measures the EOS of D_2 relative to an assumed known EOS of Al. The Nova experiment was the only measurement in this set of four experiments that was absolute, that is, the compressibility of D_2 was measured directly as opposed to being inferred by comparison with the EOS of a reference material. This experiment showed enhanced compressibility, not evident in the other experiments. The reason for the difference between the Nova laser measurements and all the rest of the measurements is still under debate. A new set of relative measurements done on the Omega laser favors an EOS of D_2 that is less compressible than the Nova data (Boehly *et al.*, 2004), however, the situation is still far from settled (Mostovych *et al.*, 2001; Nellis, 2002). To conclude this ongoing debate, it seems likely that a new set of absolute measurements will be necessary. There are a number of models of the EOS of high-pressure hydrogen being compared with these data, as shown in Fig. 35(a). The tabular SESAME EOS and *ab initio* models generally are in agreement with the stiffer EOS data from *Z*. The linear mixing models and the Saumon–Chabrier–Van Horn model generally favor a softer EOS, that is, higher compressibility. First measurements have also been made of shock compressing hydrogen precompressed in a diamond anvil cell (DAC), allowing denser states to be experimentally accessed (Loubeyre *et al.*, 2004).

The impact on the predicted structure of the interior of Jupiter for the different EOS models is shown in Fig. 35(b) (Saumon and Guillot, 2004). This figure shows the mass of the core of Jupiter versus the mass of high-Z elements mixed throughout the planet, predicted using five different models of high-pressure EOS of D_2. Models that did not reproduce the global gravitational moments of Jupiter, as determined by satellite fly-by missions, were eliminated from these comparisons. The results in Fig. 35(b) show that the interior structure of Jupiter is surprisingly sensitive to the details of the high-pressure EOS of hydrogen. Hence there is considerable impact and scientific interest in concluding the experimental debate on the EOS of D_2.

There are new experimental results measuring the EOS and conductivity of high-pressure water (Celliers *et al.*, 2004; Koenig *et al.*, 2004) relevant to the interior of Neptune. In these measurements, the principle Hugoniot of water was measured by the impedance matching technique at an Al-H_2O interface, as shown in Fig. 36(a) (Celliers *et al.*, 2004). Also, the reflectivity of high-pressure water at the shock front was measured, as shown in Fig. 36(b), from which the electronic conductivity σ_e was inferred with the aid of a Drude model. This model, thus calibrated, was used to estimate σ_e along the isentrope of Neptune, as shown in Fig. 36(c). This compared with measurements of the total dc conductivity of water σ_{dc} done with singly shocked (Nellis *et al.*, 1988) and reverberating shocks on a gas gun (Chau *et al.*, 2001) suggest that the electronic conductivity contributes roughly equally with ionic conductivity at 5000 K along the isentrope of Neptune, and will begin to dominate at higher temperatures. This will have significant implications for future models of the interior of Nepture, and, in particular, on models of the formation of its magnetic field.

Also, new dynamic measurements address the EOS and high-pressure melt transition in Fe (Benuzzi-Mounaix *et al.*, 2002; Koenig *et al.*, 2004; Nguyen and Holmes, 2004), relevant to the inner-core, outer-core boundary region of the interior of Earth. A key issue here is resolving the discrepancy between the high-pressure melt temperature detected dynamically in shock experiments and static measurements in a diamond-anvil cell (DAC). Additional experiments and research will likely be required to conclude this debate.

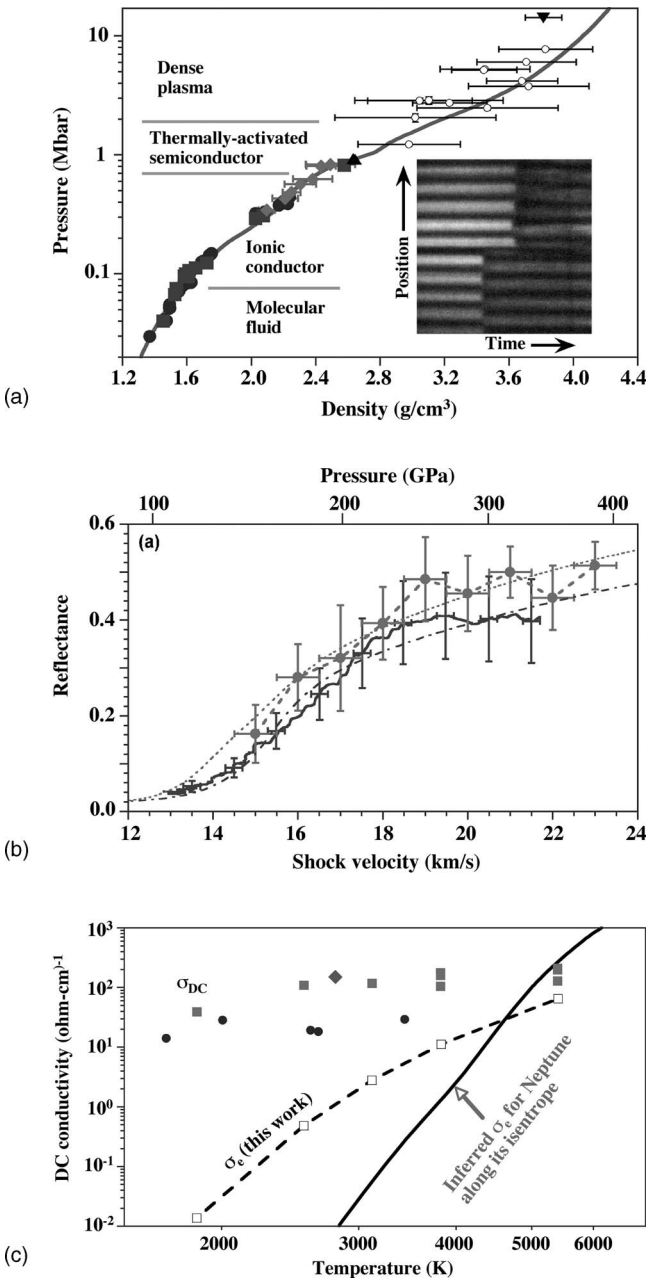

FIG. 36. The high-pressure properties of water are probed with strong shock experiments. (a) Plot of the measured EOS of water along the principle Hugoniot, at pressures up to ~1000 GPa. (b) Measurements of the reflectivity of shocked water vs shock velocity and shock pressure. (c) Analysis of the decomposition of the dc conductivity of water at high pressure along the isentrope appropriate for the interior of Nepture. Adapted from Celliers *et al.*, 2004.

IX. COMPACT OBJECT ACCRETION DISKS AND PHOTOIONIZED PLASMAS

Photoionized plasmas are encountered in a wide variety of situations in astrophysics, namely, wherever gas is bathed in a strong radiative flux. Examples include emission nebulae that result from the photoionization of a diffuse gas cloud by ultraviolet photons from a hot "exciting" star (Osterbrock, 1989), line emission induced by continuum radiation from strong shocks, and x-ray-continuum-pumped line emission from accretion disks around compact objects such as neutron stars, black holes, or white dwarfs (e.g., Ballantyne *et al.*, 2002). Such pumping by continuum x rays occurs in x-ray binaries, discussed further below, as well as in active galactic nuclei, not discussed here (Krolik, 1999).

Here we focus primarily on the photoionized plasma conditions generating line emission from x-ray binaries, which are neutron stars or stellar-mass black holes in orbit with a stellar companion. These typically fall into two categories, divided by the mass of the stellar com-

panion: low-mass x-ray binaries (LMXB), where the companion mass is less than about $(1-2)M_\odot$ (solar masses); and high-mass x-ray binaries (HMXB), where the companion star is typically several tens of solar masses. The line emission from LMXBs is mostly thought to arise in an irradiated accretion disk [as illustrated schematically in Fig. 37(a) (Jimenez-Garate *et al.*, 2002)]. In HMXBs, much line emission can be produced by photopumping of a wind issuing from the companion [illustrated schematically in Fig. 37(b) (Willingale *et al.*, 1985)].

An example of an accreting compact object is Cygnus X-3 (Bonnet-Bidaut and Chardin, 1988), an object whose companion likely started out life as a massive star (although its mass today is highly uncertain) and the nature of whose compact object remains controversial (e.g., Lommen *et al.*, 2005). A sample Chandra x-ray spectrum from Cyg X-3 is shown in Fig. 37(c) (Paerels *et al.*, 2000). The energy source "pumping" the emission lines is believed to be the hard x-ray continuum emanating from the accreting compact object. The simplest interpretation of Cyg X-3 is that the x-ray emission is from plasma in photoionization equilibrium (Liedahl and Paerels, 1996). Particularly striking in Fig. 37(c) are the radiative recombination continuum (RRC) peaks. The widths of these RRC peaks give a very good determination of T_e in the plasma, which is too small to produce the observed ionization states by collisional ionization. Different peaks correspond to different levels of ionization, and their widths typically suggest different temperatures of their emitting regions. Global shifts of the identified peaks in the photoionized plasma spectra are produced by variations in the collective plasma flow velocity. Hence, through the combined observations of $\langle Z\rangle$, RRC peak widths, and shifts in various line positions, the overall dynamics of the plasma in the vicinity of the accreting compact object can start to be mapped out.

To illustrate the basics of photoionized plasmas [following the nomenclature of Liedahl (1999)], we assume steady-state ionization balance, and write

$$\beta_i n_i + n_e C_i n_i = n_e \alpha_{i+1} n_{i+1} + n_e^2 \alpha_{3,i+1} n_{i+1}, \tag{9.1}$$

where n_e, n_i, β_i, and C_i represent electron density (cm^{-3}), ion density of charge state i (cm^{-3}), the photoionization rate (s^{-1}) of charge state i, and the collisional ionization rate coefficient ($\mathrm{cm}^3\,\mathrm{s}^{-1}$) of i, respectively. The coefficients α_{i+1} and $\alpha_{3,i+1}$ are for charge state $i+1$ the two-body recombination rate coefficient ($\mathrm{cm}^3\,\mathrm{s}^{-1}$), including radiative recombination and dielectronic recombination, and the three-body recombination coefficient ($\mathrm{cm}^6\,\mathrm{s}^{-1}$), respectively. Three-body recombination is the inverse process of electron collisional ionization, and is generally important only at high densities, $n_e > 10^{16}\ \mathrm{cm}^{-3}$. For the case of x-ray binaries, which is the example we discuss here, typically $n_e\alpha_{3,i+1} \ll \alpha_{i+1}$, that is, three-body recombination is negligible relative to two-body recombination (Jimenez-Garate *et al.*, 2002), so we assume $\alpha_{3,i+1} \sim 0$. The situation with $\beta_i = 0$ represents collisional ionization equilibrium (CIE), also referred to as coronal equilibrium, where radiative recombination is balanced by collisional ionization by electrons, and ionization by radiation is negligible. The CIE ionization balance is written as

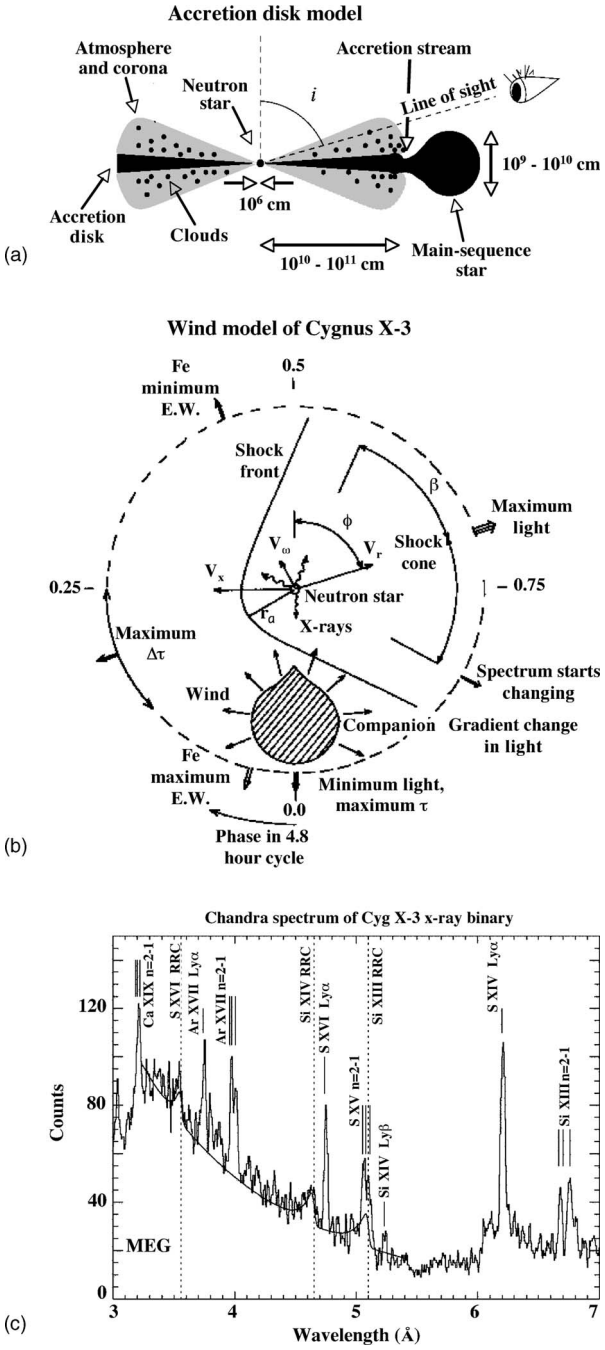

FIG. 37. Models of accreting compact objects, such as neutron stars or black holes, and an x-ray spectrum from such an object. (a) Accretion disk model for low-mass x-ray binaries. Adapted from Jimenez-Garate *et al.*, 2002. (b) Stellar wind model for high-mass x-ray binaries. Adapted from Willingale *et al.*, 1985. (c) X-ray spectrum from the Chandra medium energy grating spectrometer of the photoionized plasma in the immediate vicinity of Cyg X-3 x-ray binary. The Cygnus X-3 binary system sits at a distance of ~10 kpc, and has a binary orbital period of 4.79 hr. Adapted from Paerels *et al.*, 2000.

$$\left(\frac{n_{i+1}}{n_i}\right)_{\mathrm{CIE}} = \frac{C_i}{\alpha_{i+1}}. \tag{9.2}$$

In contrast, the situation with $n_e C_i \ll \beta_i$ can be referred to as photoionization equilibrium (PIE). The photoionization rate for a point source of ionizing continuum at a distance r from the location of interest can be written (Liedahl, 1999) $\beta_i = L_x \phi_i / r^2$, where L_x is the x-ray luminosity (ergs/s) from the accreting compact object, and the coefficient ϕ_i having units of $\mathrm{cm}^2/\mathrm{erg}$ is defined by

$$\phi_i = \frac{1}{4\pi}\int_{\chi_i}^{\infty} d\varepsilon \frac{f_\varepsilon(\varepsilon)}{\varepsilon}\sigma_i(\varepsilon).$$

Here χ_i is the ionization potential out of charge state i and $f_\varepsilon(\varepsilon)$ is the spectral shape function, normalized so that $\int d\varepsilon f_\varepsilon(\varepsilon) = 1$, where the integral is over x-ray energy ε. The PIE ionization balance is then written as

$$\left(\frac{n_{i+1}}{n_i}\right)_{\mathrm{PIE}} = \frac{\beta_i}{n_e \alpha_{i+1}} = \frac{L_x}{n_e r^2}\frac{\phi_i}{\alpha_{i+1}} = \xi \frac{\phi_i}{\alpha_{i+1}}, \tag{9.3}$$

in which we have defined the ionization parameter ξ as $L_x/n_e r^2$ (with units of erg cm/s) which is one of several similar definitions in the astrophysical literature. Note that while the ratio of ionization state populations in CIE depends only on a ratio of coefficients, the ratio in PIE depends on a ratio of coefficients and in addition on ξ.

In terms of the ionization parameter (ignoring three-body recombination), one can write Eq. (9.1) as

$$\left(\frac{n_{i+1}}{n_i}\right) = \frac{C_i}{\alpha_{i+1}}\left(1 + \frac{\xi \phi_i}{C_i}\right). \tag{9.4}$$

This allows one to see easily the CIE limit, where $\xi = 0$, and the PIE limit, where ξ is very large. One can also see why photoionized plasmas are often described as "over-ionized," since their ionization is always larger (and is sometimes much larger) than the ionization of a CIE plasma at the same electron temperature T_e.

The emission spectrum from a photoionized plasma having large ξ includes prominent recombination lines, produced when electrons radiatively recombine with an ion, reducing its charge state. Recombination lines are thermally broadened to higher energy because the electron that joins the ion may have a range of initial energies. Thus the amount of broadening increases with and is a diagnostic of T_e. The recombination lines from a strongly photoionized plasma are narrow compared to those from collisionally ionized plasmas, because the charge states (and thus transition energies) are far larger than those that would be produced by thermal electrons without the radiation. The narrowness of the recombination lines is one signature of a photoionized plasma. There are also other differences in the emission spectra of photoionized (as opposed to collisionally ionized) plasmas (Liedahl *et al.*, 2001). In regions of PIE, highly ionized ions are observed by UV and x-ray satellites over the range $\xi = 10$–10^4 ergs cm/s. Below that range, recombination lines fall at energies below the x-ray band and are not observed by x-ray satellites. Above that range, most ions are fully stripped and neither free-bound nor bound-bound transitions are observed.

Photoionized plasma codes that calculate ionization balance and predict emission spectra are essential for interpreting spectral data from astrophysics and from the laboratory. Most of the different codes in wide use have similar overall structures and approaches (Ferland *et al.*, 1998; Liedahl *et al.*, 2001). These models do not assume an equilibrium (LTE) distribution of ionization or of excited states and they may or may not assume a Planckian radiation spectrum. The level of ionization is determined by balancing all ionization and recombination processes. Ionization processes include photo, Auger, and collisional ionization and charge transfer. Recombination processes include radiative, dielectronic, three-body recombination, and charge transfer. Free electrons are typically assumed to have a Maxwellian velocity distribution. These models typically solve equations for the line and continuum radiative transfer simultaneously, and thus evolve the radiation spectrum and predict the detailed emission spectra. The charge state fractions, atomic excitations, and emission spectra are computed in some kind of "detailed level accounting" methodology, evolving the dominant rates into and out of each energy level. The various models treat the atomic structure and detailed level accounting at various levels of sophistication and detail. Examples follow of codes currently in wide use that calculate spectral emissions from photoionized plasmas.

GALAXY is a collisional-radiative code that calculates the steady-state ionization balance within the plasma, given density, temperature, and incident radiation field as input (Rose, 1998; Foord *et al.*, 2004, 2006; Rose *et al.*, 2004). Collisional and radiative excitation and ionization as well as autoionization and all reverse processes are included. Screened hydrogenic rates for both collisional and radiative processes are assumed, and Hartree-Dirac-Slater (HDS) cross sections are used for photoionization. The GALAXY code employs an average-of-configuration approximation for electronic states with a principal quantum number $n \leq 5$ and configuration averages for higher n.

NIMP is a non-LTE, average-atom model (Djaoui and Rose, 1992; Rose *et al.*, 2004). It follows the time evolution of principal quantum shell occupancies, averaged over the distribution of ionic states. As a result, the shell occupancies are noninteger. By following the shell populations in time, the number of differential equations is reduced in comparison with what is needed for a model that follows individual ionic states. A fundamental approximation made is that there is no statistical correlation between electrons occupying different shells. NIMP includes photoexcitation and photionization, as well as their inverse rates, using simple Kramers photoionization cross sections, convolved with the intensity of the ambient radiation field. NIMP employs a time-dependent model, that is, it does not assume steady-state conditions.

FLYCHK is a collisional-radiative model that calculates non-LTE, non-steady-state ionization distributions, given inputs of density, temperature, and radiative flux (Chung *et al.*, 2003). It uses highly accurate atomic data for ions with an open K shell and for Li-like ions. Their populations are calculated from rate equations including all relevant collisional and radiative processes. The kinetics of other ions with an open L shell or M shell are included by assuming a hydrogenic model for selected ions, for which transitions out of and into excited states are calculated, and ground states for the remaining ions. Alternatively, a screened hydrogenic model for all ions, including ions with an open K shell, can be selected. In this case, ground-state and excited-state configurations are considered in the calculation of all rates. FLYCHK is capable of performing calculations for steady-state or time-dependent cases, and for collisionally dominated as well as radiation-dominated cases. This code, and its predecessor FLY, were developed originally to model ionization balance and kinetics in high power laser experiments. They have been compared against a wide variety of laboratory data over the past two decades.

CLOUDY is a steady-state, photoionized-plasma code developed to analyze and interpret spectral observations of astrophysical plasmas. It has been in use in the astrophysics community for ~25 years (Ferland *et al.*, 1998). More recently, it has started to come into use to calculate ionization balance in laboratory experiments on high-energy-density facilities, such as Z pinches and lasers (Foord *et al.*, 2006). CLOUDY is a large-scale, spectral-synthesis code designed to simulate the heating and cooling within an astrophysical plasma of a given density and then to predict the emitted spectrum. It relies on atomic databases to allow accurate comparisons with spectral emission data. CLOUDY calculates both the ionization balance and electron temperature by a detailed energy accounting of all relevant heating and cooling processes in the plasma, such as from collisional excitation followed by radiative cooling. With input of density, species concentrations, and incident x-ray flux, CLOUDY will calculate emission spectra and the plasma T_e. The other models above assume T_e is given as input.

There are other photoionized plasma codes that have not yet been applied to the experiments discussed below. One example is the XSTAR code (Kallman *et al.*, 1996, 2004; Bautista and Kallman, 2001; Kallman and Bautista, 2001; Boroson *et al.*, 2003), which calculates a steady-state model of a spherical gas cloud with a radiation source at its center. The input parameters include the source spectrum, the gas composition and density, and ionization parameters. XSTAR then finds as a function of radius the electron temperature, the atomic level populations, and the emitted spectrum that escapes the cloud. XSTAR has been applied (Boroson *et al.*, 2003) to HMXBs. Another example is the code TITAN (Dumont *et al.*, 2000; Collin *et al.*, 2004), which makes similar assumptions to those of XSTAR and also includes Comptonization and emphasizes an accurate treatment of radiative line transfer.

To test and validate the models used to interpret astrophysical photoionized plasma spectra, such as that shown in Fig. 37(c), experimental data from photoionized plasmas in relevant regimes are required. It was recognized recently that relevant conditions could be created in the laboratory using the intense burst of x rays coming from the Z-pinch at the SNLA Z facility (Bailey *et al.*, 2001; Heeter *et al.*, 2001; Cohen *et al.*, 2003). An experiment was developed to measure the x-ray spectra from a photoionized plasma under approximately scaled conditions. As discussed above, the figure of merit is the ionization parameter $\xi = L_x/n_e r^2$. The goal was to reproduce, in a scaled sense, the photoionization conditions found in the x-ray binary Cyg X-3, where $\xi = 10^2 - 10^3$ erg cm/s.

In the experiments radiation from the pinch was generated by coupling a 20-MA, 100-ns rise time current pulse into a 2-cm-diameter, 1-cm-length, cylindrical wire array, producing plasma that implodes at hundreds of km/s and then stagnates, causing intense x-ray emission. This created an 8-ns full width at half maximum x-ray source with a spectrum close to that of a black body with a temperature T_r of 165 eV. The x-ray flux from the pinch is spectrally measured with the combination of an absolutely calibrated transmission grating spectrometer, an array of filtered x-ray detectors (XRDs), and an array of filtered photoconducting detectors (PCDs). The result is shown in Fig. 38(a). For comparison, a peak-normalized $T_r = 165$ eV black-body radiation spectrum is also shown (Foord *et al.*, 2004). This x-ray burst at peak power is preceded by a period of lower radiation flux. A sample was designed so that the early, lower radiation flux would produce a large, slowly evolving plasma through which the later, intense radiation could penetrate. The charge-state distribution in the sample, the density in the sample, and absolute radiative flux as a function of energy were measured independently. The pinch also produces a quasicontinuum x-ray source at the energies required to produce a useful absorption spectrum. A typical absorption spectrum from an Fe sample, located a distance of 1.5–1.6 cm from the pinch, is shown in Fig. 38(b) (Foord *et al.*, 2004). In this experiment, ξ reaches a value near 25 ergs cm/s at the peak of the radiation pulse, and the observed time-integrated absorption spectrum is believed to correspond to $\xi \sim 20$. The measured electron density is $n_e \sim 2 \times 10^{19}$ cm^{-3}. Also, calculations show that electrons and ions equilibrate rapidly, so the ion temperature T_i can be taken to equal T_e (Foord *et al.*, 2004, 2006). The code CLOUDY, when allowed to calculate the electron temperature and run with a model consistent with the measured saturation of the Fe resonance lines, finds $T_e = 150$ eV.

A number of photoionized plasma models have now been compared with these results, as shown in Figs. 38(c) and 38(d). In Fig. 38(c) (Foord *et al.*, 2004, 2006) we show the results for steady-state simulations using fixed T_e and n_e. The radiation field has a spectrum and energy density consistent with those produced by the pinch in the experiment, but is implemented in the simulations as

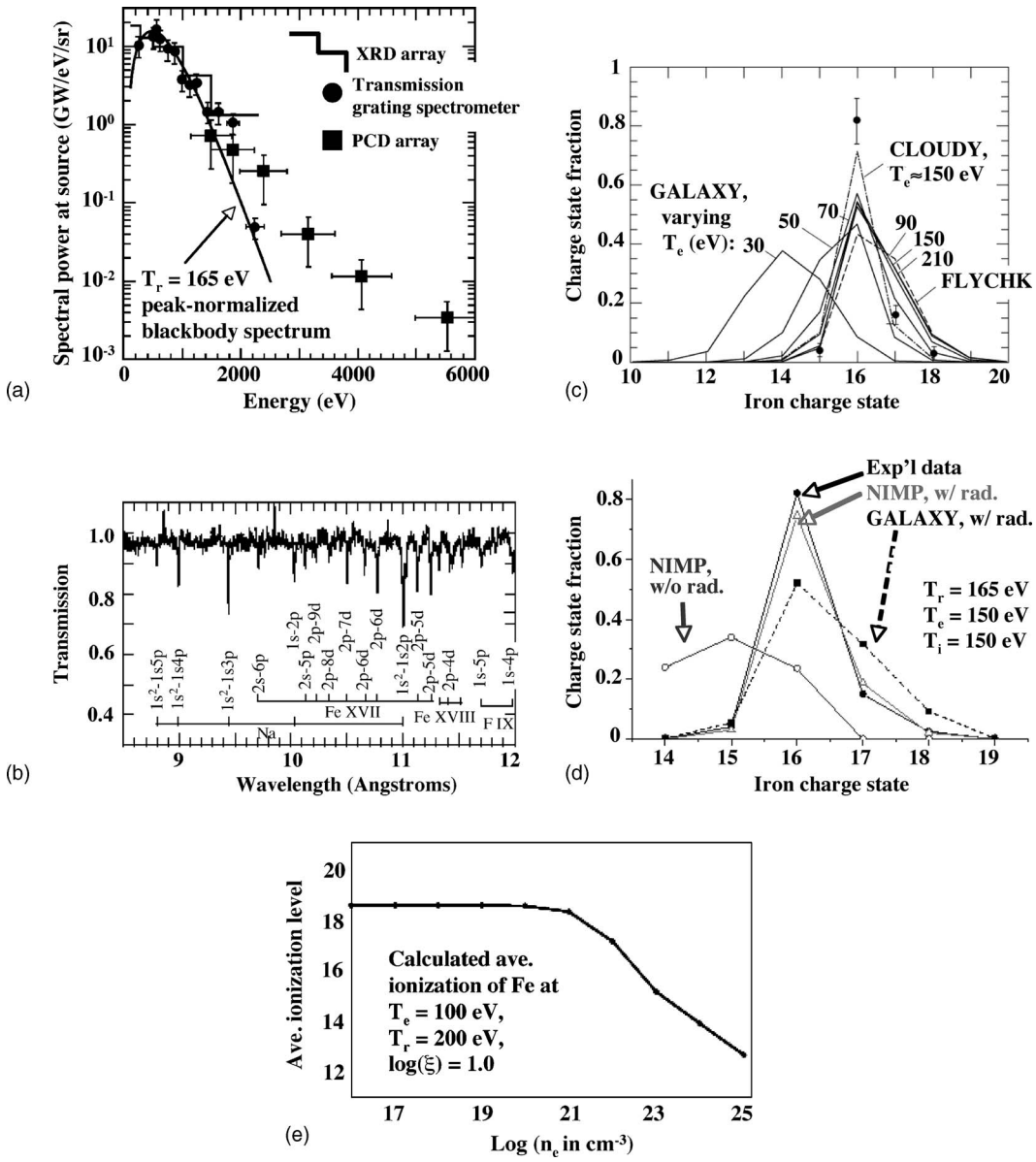

FIG. 38. The results from experiments on the Z facility test models of photoionized plasmas. (a) Z-pinch x-ray flux spectral measurement at peak power with an XRD array (stepped lines), a transmission grating spectrometer (solid circles), and a PCD array (solid squares). Shown for comparison is a peak-normalized T_r=165 eV black-body spectrum. Adapted from Foord *et al.*, 2004. (b) X-ray spectrum in a scaled experiment done on the Z-pinch facility. The figure shows the absorption spectrum of iron lines from ions with an open L shell and of sodium and fluorine lines from ions with an open K shell. Adapted from Foord *et al.*, 2004. (c) Calculations of the ionization distribution from the photoionized plasma models GALAXY, CLOUDY, and FLYCHK compared with observations. Adapted from Foord *et al.*, 2004. (d) Calculations of the ionization distribution from the photoionized plasma models NIMP and GALAXY, compared with that observed in the experiment of (a). Adapted from Rose *et al.*, 2004. (e) A calculation using the GALAXY model of the average ionization of iron vs electron density for input conditions described in the text, which were similar to those of the experiment of (a). Adapted from Phillips *et al.*, 2001.

an isotropic field. The conditions used correspond to ξ =20. Results from the model GALAXY are shown as a function of temperature from 30 to 210 eV. The experimental data are shown by the circular symbols with error bars. At the density of the experiment ~2 $\times 10^{19}$ cm^{-3} calculations show that as T_e is lowered below ~50 eV, three-body recombination becomes important, and $\langle Z \rangle$ starts to decrease. From 70 to 210 eV, however, additional increases in temperature have little effect, because three-body recombination has become small and thermal electrons have insufficient energy to ionize ions that were produced by photoionization. Simulations from the models FLYCHK (Chung *et al.*, 2003) run with T_e=150 eV and CLOUDY (Ferland *et al.*, 1998) are also shown. It is interesting to note that FLYCHK and GALAXY predict broader distributions than CLOUDY (and the data), shown in Fig. 38(c). For temperatures in the range T_e=70–210 eV, GALAXY predicts

a width of full width at half maximum of 1.6–1.7, compared to 1.2 for CLOUDY. Differences in the widths are likely due to differences in the specific rates that couple the Fe^{15+}, Fe^{16+}, Fe^{17+}, and Fe^{18+} ions (Foord *et al.*, 2004). For example, dielectric recombination and autoionization are treated somewhat differently in each code, which could effect $\langle Z \rangle$ and the ionization distribution width (Foord *et al.*, 2000; Rose *et al.*, 2004). The fact that CLOUDY calculates T_e and the charge state self-consistently may be relevant to its better agreement with the data (Foord *et al.*, 2006). More extensive comparisons with data would be needed, however, before such a conclusion could be firmed up. Properly treating radiative transfer in the major cooling lines, which are at least partially optically thick, is also important for getting more realistic models. This is an area where considerable work still needs to be done (Van Hoof, 2005).

Additional comparisons of the predicted versus experimentally observed ionization distribution for this plasma are shown in Fig. 38(d) (Rose *et al.*, 2004), for calculations with the average-atom model NIMP (Rose *et al.*, 2004), making the assumptions described in the previous paragraph regarding n_e, T_e, and the magnitude and spectrum of the radiation field. Calculations are shown without and with inclusion of the radiation field. Without radiation, the observed ionization state would be underpredicted. In other words, photoionized plasmas exhibit $\langle Z \rangle$ which is significantly greater than the result in collisional regimes at the same T_e. Also included in the comparison are predictions from GALAXY (Rose, 1998) presented for the same conditions. It is interesting that the average atom model NIMP, which is a much simpler model, does a better job at reproducing the measured ionization distribution than GALAXY, which includes much more detailed atomic physics. This suggests that refinements may be needed in the transition rates used by GALAXY to populate the Fe^{16+}, Fe^{17+}, and Fe^{18+} ions, in particular, in the dielectronic recombination and autoionization processes (Foord *et al.*, 2006). NIMP, on the other hand, follows the time evolution of principal quantum shell occupancies, averaged over the distribution of ionic states. This class of model has been used widely over the past three decades, and has been extensively and successfully calibrated against laser experiments, which may contribute to the better agreement with data shown in Fig. 38(d). It may also be that "coverage" is more important than "accuracy" for capturing the average charge state distribution of the plasma (Rose *et al.*, 2004). Even though the atomic data used in NIMP are not as detailed or as accurate as in GALAXY, NIMP includes all possible energy levels and transition pathways in an average sense. This may, in fact, be more important for calculating the average ionization state. If, on the other hand, one is trying to match an individual spectral line position or shape, then accuracy is more important, and GALAXY would be superior to NIMP.

An evaluation of the predicted effect of density on $\langle Z \rangle$ is shown explicitly in Fig. 38(e). This figure shows the results of GALAXY calculations (Phillips *et al.*, 2001) for the average ionization of Fe, over a wide range of electron density $n_e(\mathrm{cm}^{-3})$. The calculations assumed that $T_e = 100$ eV, that the radiation spectrum was Planckian with $T_r = 200$ eV, and adjusted the radiation flux to maintain $\xi = 10$ ergs cm/s. This shows that, for the conditions roughly similar to those achieved in the experiment at the Z facility, the electron density needs to stay below $n_e < 10^{19}$ cm^{-3} for collisional effects (three-body recombination, collisional ionization) to be negligible in the ionization balance.

X. OUTLOOK FOR THE FUTURE

There are a multitude of new facilities on the horizon that will enhance the ability to pursue HED laboratory astrophysics. These include high-energy, long pulse lasers and magnetic pinch facilities; high-energy, short pulse lasers; and ultrashort pulse lasers. In the category of high-energy HED facilities, the NIF (at LLNL) (Hogan *et al.*, 2001; Miller, 2004; Moses, 2004) and LMJ (at CEA in Bordeaux, France) (Andre, 1999; Cavailler *et al.*, 2004) lasers will each deliver about ~2 MJ of laser energy, once they are complete. The LIL laser in Bordeaux, France, will be an eight-beam demonstration facility for LMJ, and should achieve at full performance over 60 kJ of 3ω light (Di-Nicola *et al.*, 2004). The ZR magnetic pinch facility (at SNLA) will deliver a fast rise-time pulse of 30 MA current to implode a cylindrical wire array, generating over ~2 MJ of x rays (Matzen *et al.*, 2005). The Omega-EP facility (Stoeckl *et al.*, 2006) will include two 2.5-kJ PW lasers, which can be focused either into a stand-alone chamber or into the Omega 60-beam chamber, synchronized with the 30 kJ, 60-beam Omega laser, enabling new regimes of high intensity laser-matter interaction studies (Sangster, 2004). The LULI laser facility is being upgraded to have four beams: one 1-kJ, 1ω-long pulse beam, one PW beam, and two 100-J probe beams (Koenig *et al.*, 2004). The Gekko-12 laser facility at Osaka University will be upgraded so that the 12-beam, 10-kJ-long pulse Gekko will be augmented by a high-energy (up to ~10 kJ) petawatt beam for fast ignition studies (Miyanaga *et al.*, 2004). The Helen laser at AWE in the UK will be upgraded into Orion, which will be ten 1/2-kJ 2ω beams, plus two 1/2-kJ petawatt lasers. And the Vulcan petawatt is just starting routine operation at ~500 J in ~1/2 ps (Danson *et al.*, 2004). There are also a number of ultrashort pulse ($\lesssim$1 ps), moderate-energy lasers operating or under development, such as the Texas Petawatt at the University of Texas at Austin (Gaul *et al.*, 2005), and the Leopard laser at the University of Nevada at Reno. The Zebra magnetic pinch machine, also at the University of Nevada at Reno, is being developed, and will be combined with the Leopard laser, to form the Nevada Terawatt Facility (Erlandson *et al.*, 2004). All of these facilities will eventually be equipped with an array of time-resolved diagnostics, for carrying out unique HED experiments.

The greater number of HED experimental facilities will allow the new area of HED laboratory astrophysics

to be developed at a much faster pace. With the advent of the next generation of very large facilities (NIF, LMJ, ZR), key new regimes will be accessible where current facilities have fallen short. Based on the discussions given in this article, we suggest the following as potential fruitful areas for next generation HED laboratory astrophysics studies on the large facilities.

In the area of SN explosion hydrodynamics, a scaled, multilayer, spherically divergent experiment could be carried out that should transition well into the turbulent regime. Attempts at a scaled down version of such an experiment on the Omega laser came up short in the amount of energy available to drive the package. The desired hydrodynamic instabilities were initiated, but never entered the deep nonlinear regime (Robey *et al.*, 2001; Drake *et al.*, 2002). With the larger energies available on NIF and LMJ, this multilayer, divergent geometry experiment could serve as a conclusive test whether the "standard (spherical shock) model" of core-collapse SNe is correct, at least from a hydrodynamic perspective.

It should become possible to test high Mach number jet propagation and collimation over longer distances through an ambient medium, with and without the effects of radiative cooling. Experiments such as this should help answer whether astrophysical jets can remain collimated from a purely hydrodynamic or radiative-hydrodynamic perspective or whether additionally magnetic fields are required.

With the more intense bursts of x rays possible on the next generation larger facilities (NIF, LMJ, ZR), it should be possible to conduct photoionized plasma experiments in the correct regime of ionization parameter, $\xi \sim L/n_e r^2$, allowing black-hole accretion disk models to be tested under properly scaled conditions.

In the area of opacities, the larger facilities open up the possibility for measurements of opacity under conditions relevant to the core of solar-sized stars (~1 keV, 100 g/cm^3). Also, measurements of expansion opacities, that is, opacities in a homologously expanding ball of plasma, should be possible. These are relevant to SN light curve calculations.

Another new regime will be the ability to study matter under planetary interior conditions, with quasi-isentropic drives that reach 1–10-Mbar conditions, or higher, in a well-controlled, reproducible manner. This should allow EOS determinations and measurements of phase, conductivity, and maybe even solubility of mixtures of H, He, and more complex "ices" under conditions relevant to planetary interiors. It should be possible to experimentally show, unambiguously, whether or not the plasma phase transition in hydrogen exists. It may even be possible to study properties of matter under even more extreme conditions relevant to the envelopes of white dwarf stars. White dwarfs are interesting in their own right, but also serve as "cosmochronometer" (Fontaine *et al.*, 2001), and when accreting from a binary partner, form the initial conditions for a type-I SN.

Extended duration radiation sources will be available, which will be ideal for experimental studies of models and the dynamics of radiatively driven molecular clouds, such as the Eagle Nebula (Mizuta *et al.*, 2005a, 2005b; Pound *et al.*, 2005). Unique effects are predicted due to the directionality of the radiation, due to stars acting effectively as "point sources," and due to the photoevaporated plasma not necessarily being optically thin (Kane *et al.*, 2005; Mizuta *et al.*, 2005a, 2005b).

Once ignition is achieved, the intense burst of D-T neutrons, generating a flux of 10^{32}–10^{33} neutrons/cm^2 s, may allow excited-state reactions to occur, which are relevant to the nucleosynthesis of heavy elements, i.e., those nuclei more massive than Fe (Libby *et al.*, 2004). It may also be possible to study thermonuclear reactions in highly screened, dense plasmas, relevant to reactions in dwarf stars. If high gain ($G > 100$) implosions can be produced (Suter *et al.*, 2004), it may be possible to examine some of the physics issues surrounding the proposed deflagration-to-detonation transition, and the role of hydrodynamic mixing, relevant to type-I supernovae.

Finally, with ultrahigh intensity, short-pulse lasers it may be possible to study matter under ultraextreme conditions relevant to the vicinity and atmospheres of accreting neutron stars (Moon *et al.*, 2005). Extreme large magnetic fields are needed in a radiation-dominated plasma. Generation of the electron-positron plasma of relevance to particle acceleration mechanisms in astrophysics has also been discussed (Liang *et al.*, 2003; Wilks *et al.*, 2005). Aspects of these conditions may be within reach with the combination of multiple petawatt lasers, plus the NIF, LMJ, or ZR driver.

ACKNOWLEDGMENTS

We gratefully acknowledge insightful discussions with Mark Foord, Bob Heeter, Duane Liedahl, Steve Rose, Peter van Hoof, and Julian Krolik in the area of photoionized plasmas.

REFERENCES

Ampleford, D. J., S. V. Lebedev, A. Ciardi, S. N. Bland, S. C. Bott, J. P. Chittenden, G. Hall, C. A. Jennings, G. Armitage, G. Blyth, S. Christie, and L. Rutland, 2005, "Formation of working surfaces in radiatively cooled laboratory jets," Astrophys. Space Sci. **298**, 241–246.

Anderson, M. C., and L. Rudnick, 1995, "The deceleration powering of synchrotron emission from the ejecta contents in supernova remnant Cassiopeia A," Astrophys. J. **441**, 307–333.

Andre, M. L., 1999, "The French megajoule laser project (LMJ)," Fusion Eng. Des. **44**, 43–49.

Arnett, W. D., 1988, "On the early behavior of supernova 1987A," Astrophys. J. **331**, 377–387.

Arnett, D., 1996, *Supernovae and Nucleosynthesis* (Princeton University Press, Princeton).

Arnett, D., 2001, "Consistency and prediction in stellar evolutionary theory," Nucl. Phys. A **688**, 177C–184C.

Arnett, D., B. Fryxell, and E. Muller, 1989, "Instabilities and nonradial motion in SN-1987A," Astrophys. J. Lett. **351**,

L63–L66.
Axford, W. I., 1964, "The stability of ionization fronts," Astrophys. J. **140**, 112–118.
Azechi, H., M. Nakai, K. Shigemori, N. Miyanaga, H. Shiraga, H. Nishimura, M. Honda, R. Ishizaki, J. G. Wouchuk, H. Takabe, K. Nishihara, K. Mima, A. Nishiguchi, and T. Endo, 1997, "Direct-drive hydrodynamic instability experiments on the GEKKO XII laser," Phys. Plasmas **4**, 4079–4089.
Bailey, J. E., G. A. Chandler, D. Cohen, M. E. Cuneo, M. E. Foord, R. F. Heeter, D. Jobe, P. W. Lake, J. J. MacFarlane, T. J. Nash, D. S. Nielson, R. Smelser, and J. Torres, 2002, "Radiation science using Z-pinch x rays," Phys. Plasmas **9**, 2186–2194.
Bailey, J. E., D. Cohen, G. A. Chandler, M. E. Cuneo, M. E. Foord, R. F. Heeter, D. Jobe, P. Lake, D. A. Liedahl, J. J. MacFarlane, T. J. Nash, D. Nielson, R. Smelser, and W. A. Stygar, 2001, "Neon photoionization experiments driven by Z-pinch radiation," J. Quant. Spectrosc. Radiat. Transf. **71**, 157–168.
Ballantyne, D. R., R. R. Ross, and A. C. Fabian, 2002, "Soft x-ray emission lines from photoionized accretion discs: Constraints on their strength and width," Mon. Not. R. Astron. Soc. **336**, 867–872.
Bar-Shalom, A., J. Oreg, W. H. Goldstein, D. Shvarts, and A. Zigler, 1989, "Super-transition-arrays: A model for the spectral analysis of hot, dense plasma," Phys. Rev. A **40**, 3183–3193.
Bautista, M. A., and T. R. Kallman, 2001, "The XSTAR atomic database," Astrophys. J., Suppl. Ser. **134**, 139–149.
Belov, S. I., G. V. Boriskov, A. I. Bykov, R. I. Il'kaev, N. B. Luk'yanov, A. Ya. Matveev, O. L. Mikhailova, V. D. Selemir, G. V. Simakov, R. F. Trunin, I. P. Trusov, V. D. Urlin, V. E. Fortov, and A. N. Shuikin, 2002, "Shock compression of solid deuterium," Pis'ma Zh. Eksp. Teor. Fiz. **76**, 508–510 [JETP Lett. **76**, 433–435 (2002)].
Bennet, G. R., D. B. Sinars, R. B. Cambpell, M. E. Cuneo, T. A. Mehlhorn, J. L. Porter, B. H. Wilde, R. F. Coker, P. A. Rosen, J. M. Foster, T. S. Perry, and B. B. Afeyan, 2004, "Z-pinch-driven-hohlraum high-Mach number jets on Z," Bull. Am. Phys. Soc. **49**, 113.
Benuzzi-Mounaix, A., M. Koenig, G. Huser, B. Faral, D. Batani, E. Henry, M. Tomasini, B. Marchet, T. A. Hall, M. Boustie, T. De Resseguier, M. Hallouin, F. Guyot, D. Andrault, and T. Charpin, 2002, "Absolute equation of state measurements of iron using laser driven shocks," Phys. Plasmas **9**, 2466–2469.
Bertoldi, F., 1989, "The photoevaporation of interstellar clouds. 1. Radiation-driven implosion," Astrophys. J. **346**, 735–755.
Bertoldi, F., and C. F. McKee, 1990, "The photoevaporation of interstellar clouds. 2. Equilibrium cometary clouds," Astrophys. J. **354**, 529–548.
Bertschinger, E., 1986, "On the structure and stability of radiative shock waves," Astrophys. J. **304**, 154–177.
Bethe, H. A., 1990, "Supernova mechanisms," Rev. Mod. Phys. **62**, 801–866.
Bethe, H. A., and J. R. Wilson, 1985, "Revival of a stalled supernova shock by neutrino heating," Astrophys. J. **295**, 14–23.
Bettinger, A., and M. Decroisette, 1999, "Laser megajoule project and impact on the inertial fusion program," Fusion Eng. Des. **46**, 457–460.
Birkinshaw, M., and R. L. Davies, 1985, "The orientations of the rotation axes of radio galaxies. I. Radio morphologies of bright elliptical galaxies," Astrophys. J. **291**, 32–44.
Blair, W. P., J. A. Morse, J. C. Raymond, R. P. Kirshner, J. P. Hughes, M. A. Dopita, R. S. Sutherland, K. S. Long, and P. F. Winkler, 2000, "Hubble space telescope observations of oxygen-rich supernova remnants in the magellanic clouds. Ii. Elemental abundances in n132d and 1e 0102.2-7219," Astrophys. J. **537**, 667–688.
Blondin, J. M., E. B. Wright, K. J. Borkowski, and S. P. Reynolds, 1998, "Transition to the radiative phase in supernova remnants," Astrophys. J. **500**, 342–354.
Blondin, John M., Bruce A. Fryxell, and Arieh Konigl, 1990, "The structure and evolution of radiatively cooling jets," Astrophys. J. **360**, 370–386.
Blue, B. E., S. V. Weber, S. G. Glendinning, N. E. Lanier, D. T. Woods, M. J. Bono, S. N. Dixit, C. A. Haynam, J. P. Holder, D. H. Kalantar, B. J. MacGowan, A. J. Nikitin, V. V. Rekow, B. M. Van Wonterghem, E. I. Moses, P. E. Stry, B. H. Wilde, W. W. Hsing, and H. F. Robey, 2005, "Experimental investigation of high-Mach-number 3D hydrodynamic jets at the National Ignition Facility," Phys. Rev. Lett. **94**, 095005.
Boehly, T. R., D. G. Hicks, P. M. Celliers, T. J. B. Collins, R. Earley, J. H. Eggert, D. Jacobs-Perkins, S. J. Moon, E. Vianello, D. D. Meyerhofer, and G. W. Collins, 2004, "Properties of fluid deuterium under double-shock compression to several Mbar," Phys. Plasmas **11**, L49–L52.
Boehly, T. R., R. L. McCrory, C. P. Verdon, W. Seka, S. J. Loucks, A. Babushkin, R. E. Bahr, R. Boni, D. K. Bradley, R. S. Craxton, J. A. Delettrez, W. R. Donaldson, R. Epstein, D. Harding, P. A. Jaanimagi, S. D. Jacobs, K. Kearney, R. L. Keck, J. H. Kelly, T. J. Kessler, R. L. Kremens, J. P. Knauer, D. J. Lonobile, L. D. Lund, F. J. Marshall, P. W. McKenty, D. D. Meyerhofer, S. F. B. Morse, A. Okishev, S. Papernov, G. Pien, T. Safford, J. D. Schnittman, R. Short, M. J. Shoup, M. Skeldon, S. Skupsky, A. W. Schmid, V. A. Smalyuk, D. J. Smith, J. M. Soures, M. Wittman, and B. Yaakobi, 1999, "Inertial confinement fusion experiments with OMEGA-A 30-kJ, 60-beam UV laser," Fusion Eng. Des. **44**, 35–42.
Bohm-Vitense, Erika, 1989a, *Introduction to Stellar Astrophysics, Vol. 1: Basic Stellar Observations and Data* (Cambridge University Press, New York).
Bohm-Vitense, Erika, 1989b, *Introduction to Stellar Astrophysics, Vol. 3: Stellar Structure and Evolution* (Cambridge University Press, New York).
Bonnet-Bidaud, J.-M., and G. Chardin, 1988, "Cygnus X-3, a critical review," Phys. Rep. **170**, 325–404.
Boriskov, G. V., A. I. Bykov, R. I. Il'kaev, V. D. Selemir, G. V. Simakov, R. F. Trunin, V. D. Urlin, A. N. Shuikin, and W. J. Nellis, 2005, "Shock compression of liquid deuterium up to 109 GPa," Phys. Rev. B **71**, 092104.
Boroson, B., S. D. Vrtilek, T. Kallman, and M. Corcoran, 2003, "Chandra grating spectroscopy of the x-ray binary 4U 1700-37 in a flaring state," Astrophys. J. **592**, 516–531.
Bouquet, S., C. Stehle, M. Koenig, J-P. Chieze, A. Benuzzi-Mounaix, D. Batani, S. Leygnac, X. Fleury, H. Merdji, C. Michaut, F. Thais, N. Grandjouan, T. Hall, E. Henry, V. Malka, and J-PJ. Lafon, 2004, "Observation of laser driven supercritical radiative shock precursors," Phys. Rev. Lett. **92**, 225001.
Budil, K. S., T. S. Perry, S. A. Alvarez, D. Hargrove, J. R. Mazuch, A. Nikitin, and P. M. Bell, 1997, "Point projection radiography with the flexible x-ray imager," Rev. Sci. Instrum. **68**, 796–798.

Buresi, E., J. Coutant, R. Dautray, M. Decroisette, B. Dubourgel, P. Guillaneux, J. Launspach, P. Nelson, C. Patou, J. M. Reisse, and J. P. Watteau, 1986, "Laser program development at CEL-V: Overview of recent experimental results," Laser Part. Beams **4**, 531–544.

Burrows, A., and J. Hayes, 1996, "Pulsar recoil and gravitational radiation due to asymmetrical stellar collapse and explosion," Phys. Rev. Lett. **76**, 352–355.

Busquet, M., 1993, "Radiation-dependent ionization model for laser-created plasmas," Phys. Fluids B **5**, 4191–4206.

Calder, A., L. J. Dursi, B. Fryxell, T. Plewa, T. Weirs, T. Dupont, H. F. Robey, J. O. Kane, B. A. Remington, F. Timmes, G. Dimonte, J. Hayes, M. Zingale, R. P. Drake, P. Ricker, J. Stone, and K. Olson, 2004, "Validating astrophysical simulation codes," Comput. Sci. Eng. **6**, 10–20.

Calder, A., B. Fryxell, T. Plewa, R. Rosner, T. Dupont, H. F. Robey, J. O. Kane, B. A. Remington, R. P. Drake, G. Dimonte, M. Zingale, L. J. Dursi, F. X. Timmes, K. Olson, P. Ricker, P. MacNeice, and H. M. Tufo, 2002, "On validating an astrophysical simulation code," Astrophys. J., Suppl. Ser. **143**, 201–229.

Campbell, E. M., J. T. Hunt, E. S. Bliss, D. R. Speck, and R. P. Drake, 1986, "Nova Experimental Facility," Rev. Sci. Instrum. **57**, 2101–2106.

Cantwell, B. J., 1981, "Organized motion in turbulent-flow," Annu. Rev. Fluid Mech. **13**, 457–515.

Cavailler, Claude, Noel Camarcat, Francis Kovacs, and Michel Andre, 2004, "Status of the LMJ program," *Proceedings of IFSA-2003*, edited by B. A. Hammel, D. D. Meyerhofer, J. Meyher-ter-Vehn, and H. Azechi (American Nuclear Society, La Grange Park, IL), pp. 523–528.

Cavazzoni, C., G. L. Chiarotti, S. Scandolo, E. Tosatti, M. Bernasconi, M. Parrinello, 1999, "Superionic and metallic states of water and ammonia at giant planet conditions," Science **283**, 44–46.

Celliers, P. M., G. W. Collins, D. G. Hicks, M. Koenig, E. Henry, A. Benuzzi-Mounaix, D. Batani, D. K. Bradley, L. B. Da Silva, R. J. Wallace, S. J. Moon, J. H. Eggert, K. K. M. Lee, L. R. Benedetti, R. Jeanloz, I. Masclet, N. Dague, B. Marchet, M. Rabec Le Gloahec, Ch. Reverdin, J. Pasley, O. Willi, D. Neely, and C. Danson, 2004, "Electronic conduction in shock-compressed water," Phys. Plasmas **11**, L41–L44.

Chau, R., A. C. Mitchell, R. W. Minich, and W. J. Nellis, 2001, "Electrical conductivity of water compressed dynamically to pressures of 70–180 GPa (0.7–1.8 Mbar)," J. Chem. Phys. **114**, 1361–1365.

Chenais-Popovics, C., 2002, "Astrophysics in laboratory: Opacity measurements," Laser Part. Beams **20**, 291–298.

Chevalier, R. A., 1982, "The radio and X-ray emission from Type II supernovae," Astrophys. J. **259**, 302–310.

Chevalier, R. A., 1999, "Supernova remnants in molecular clouds," Astrophys. J. **511**, 798–811.

Chiaberge, Marco, Roberto Gilli, F. Duccio Macchetto, William B. Sparks, and Alessandro Capetti, 2003, "What do the Hubble Space Telescope and Chandra tell us about the jet and the nuclear region of the radio galaxy 3C 270," Astrophys. J. **582**, 645–653.

Chung, H-K., W. L. Morgan, and R. W. Lee, 2003, "FLYCHK: An extension to the K-shell spectroscopy kinetics model FLY," J. Quant. Spectrosc. Radiat. Transf. **81**, 107–115.

Ciardi, A., S. V. Lebedev, J. P. Chittendon, D. J. Ampleford, S. N. Gland, S. C. Bott, and J. Rapley, 2005, "Modeling magnetic tower jets in the laboratory," Astrophys. Space Sci. **298**, 277–286.

Cioffi, D. F., C. F. McKee, and E. Bertschinger, 1988, "Dynamics of radiative supernova remnants," Astrophys. J. **334**, 252–265.

Cohen, David H., Joseph J. MacFarlane, James E. Bailey, and Duane A. Liedahl, 2003, "X-ray spectral diagnostics of neon photoionization experiments on the Z-machine," Rev. Sci. Instrum. **74**, 1962–1965.

Cohen, Ehud, Tsvi Piran, and Re'em Sari, 1998, "Fluid dynamics of semiradiative blast waves," Astrophys. J. **509**, 717–727.

Cohen, M., L. V. Kuhi, 1979, "Observational studies of star formation: Conclusions," Astrophys. J. **227**, L105–L106.

Collin, S., A. M. Dumont, and O. Godet, 2004, "A new type of photoionized code required for the new era of X-ray spectroscopy," Astron. Astrophys. **419**, 877–886.

Collins, G. W., L. B. Da Silva, P. Celliers, D. M. Gold, M. E. Foord, R. J. Wallace, A. Ng, S. V. Weber, K. S. Budil, and R. Cauble, 1998, "Measurements of the Equation of State of Deuterium at the Fluid Insulator-Metal Transition," Science **281**, 1178–1181.

Connor, J. W., and J. B. Taylor, 1977, "Scaling laws for plasma confinement," Nucl. Fusion **17**, 1047–1055.

Cordes, J. M., R. W. Romani, and S. C. Lundgren, 1993, "The Guitar Nebula—A bow shock from a slow-spin, high-velocity neutron star," Nature (London) **362**, 133–135.

Courtois, C., R. A. D. Grundy, A. D. Ash, D. M. Chambers, N. C. Woolsey, R. O. Dendy, and K. G. McClements, 2004, "Experiment on collisionless plasma interaction with applications to supernova remnant physics," Phys. Plasmas **11**, 3386–3393.

Cox, A. N., and J. E. Tabor, 1976, "Radiative opacity tables for 40 stellar mixtures," Astrophys. J., Suppl. **31**, 271–312.

Da Silva, L. B., B. J. MacGowan, D. R. Kania, B. A. Hammel, C. A. Back, E. Hsich, R. Doyas, C. A. Iglesias, F. J. Rogers, and R. W. Lee, 1992, "Absorption measurements demonstrating the importance of $\Delta n=0$ transitions in the opacity of iron," Phys. Rev. Lett. **69**, 438–441.

Dalgarno, A., and R. A. McCray, 1972, "Heating and ionization of HI regions," Annu. Rev. Astron. Astrophys. **10**, 375.

Danson, C. N., P. A. Brummitt, J. Collier, R. J. Clark, M. Dominey, C. B. Edwards, R. Edwards, A. J. Frackiewicz, J. A. C. Govans, S. Hancock, P. E. Hatton, S. Hawkes, C. R. Heathcote, C. Hernandez-Gomez, P. Holligan, C. Hooker, M. H. R. Hutchinson, A. Jackson, A. Kidd, W. J. Lester, J. Monk, D. Neely, D. R. Neville, P. Norreys, M. Notley, D. A. Pepler, M. R. Pitts, C. J. Reason, D. Robinson, K. J. Rodgers, D. Rose, I. N. Ross, A. J. Ryder, M. R. Selley, D. Shepherd, T. Strange, M. Tolley, R. Wellstood, G. N. Wiggins, T. B. Winstone, P. N. M. Wright, R. W. W. Wyatt, B. E. Wyborn, and Ch. Ziener, 2004, "The Vulcan Petawatt Interaction Facility," *Proceedings of the 2003 International Conference on Inertial Fusion Science and Applications*, edited by B. A. Hammel, D. D. Meyerhofer, J. Meyher-ter-Vehn, and H. Azechi (American Nuclear Society, La Grange Park, IL), pp. 512–516.

DeYoung, David S., 1991, "Astrophysical jets," Science **252**, 389–395.

Di-Nicola, J. M., J. P. Leidinger, J. L. Bruneau, B. Le Garrec, X. Julien, E. Bordenave, R. Maleck, F. Jequier, E. Journot, O. Lutz, G. Thiell, C. Feral, H. Graillot, and M. Luttmann, 2004, "The LIL Facility start-up: First high power and high energy laser experimental results at 1053 nm and 351 nm," *Proceeding of the 2003 International Conference on Inertial Fusion Science and Applications*, edited by B. A. Hammel, D. D. Meyerhofer, J. Meyher-ter-Vehn, and H. Azechi (Ameri-

can Nuclear Society, La Grange Park, IL), pp. 558–562.
Dickel, J. R., J. A. Eilek, E. M. Jones, and S. P. Reynolds, 1989, "Radio emission from young supernova remnants: Effects of an inhomogeneous circumstellar medium," Astrophys. J., Suppl. Ser. **70**, 497–538.
Dimotakis, P. E., 2000, "The mixing transition in turbulent flows," J. Fluid Mech. **409**, 69–98.
Ditmire, T., K. Shigemori, B. A. Remington, K. G. Estabrook, and R. A. Smith, 2000, "The production of strong blast waves through intense laser irradiation of atomic clusters," Astrophys. J., Suppl. Ser. **127**, 299–304.
Djaoui, A., and S. J. Rose, 1992, "Calculation of the time-dependent excitation and ionization in a laser-produced plasma," J. Phys. B **25**, 2745–2762.
Drake, R. P., 1999, "Laboratory experiments to simulate the hydrodynamics of supernova remnants and supernovae," J. Geophys. Res. **104**, 14505–14515.
Drake, R. P., 2000, "The design of laboratory experiments to produce collisionless shocks of cosmic relevance," Phys. Plasmas **7**, 4690–4698.
Drake, R. P., 2002a, "Design of flyer-plate-driven compressible turbulent mix experiments using Z," Phys. Plasmas **9**, 3545–3551.
Drake, R. P., 2002b, "Comment on 'Collisionless shock and supernova remnant simulations on Vulcan' [N.C. Woolsey *et al.*, Phys. Plasmas 8, 2439 (2001)]," Phys. Plasmas **9**, 727–728.
Drake, R. P., 2005, "Radiative shocks in astrophysics and the laboratory," Astrophys. Space Sci. **298**, 49.
Drake, R. P., J. J. Carroll, K. Estabrook, S. G. Glendinning, B. A. Remington, and R. McCray, 1998, "Development of a laboratory environment to test models of supernova remnant formation," Astrophys. J. Lett. **500**, L157–L161.
Drake, R. P., J. J. Carroll III, T. B. Smith, P. Keiter, S. G. Glendinning, O. Hurricane, K. Estabrook, D. D. Ryutov, B. A. Remington, R. J. W., LLNL, E. Michael, and R. McCray, 2000, "Laboratory experiments to simulate supernova remnants," Phys. Plasmas **7**, 2142–2148.
Drake, R. P., S. G. Glendinning, K. Estabrook, B. A. Remington, R. McCray, R. Wallace, L. J. Suter, T. B. Smith, R. London, and E. Liang, 1998, "Observation of forward shocks and stagnated ejecta driven by high-energy-density plasma flow," Phys. Rev. Lett. **81**, 2068–2071.
Drake, R. P., D. R. Leibrandt, E. C. Harding, C. C. Kuranz, M. A. Blackburn, H. F. Robey, B. A. Remington, M. J. Edwards, A. R. Miles, T. S. Perry, R. J. Wallace, H. Louis, J. P. Knauer, and D. Arnett, 2004, "Nonlinear mixing behavior of the three-dimensional Rayleigh-Taylor instability at a decelerating interface," Phys. Plasmas **11**, 2829–2837.
Drake, R. P., H. F. Robey, O. A. Hurricane, Y. Zhang, B. A. Remington, J. Knauer, J. Glimm, D. Arnett, J. O. Kane, K. S. Budil, and J. Grove, 2002, "Experiments to produce a hydrodynamically unstable, spherically diverging system of relevance to instabilities in supernovae," Astrophys. J. **564**, 896–908.
Drake, R. P., T. Smith, J. J. Carroll, III, Y. Yan, S. G. Glendinning, K. Estabrook, D. D. Ryutov, B. A. Remington, R. J. Wallace, and R. McCray, 2000, "Progress toward the laboratory simulation of young supernova remnants," Astrophys. J., Suppl. Ser. **127**, 305–310.
Dumont, A. M., A. Abrassart, and S. Collin, 2000, "A code for optically thick and hot photoionized media," Astron. Astrophys. **357**, 823–838.
Edens, A. D., T. Ditmire, J. F. Hansen, M. J. Edwards, R. G. Adams, P. Rambo, L. Ruggles, I. C. Smith, and J. L. Porter, 2004, "Study of high Mach number laser driven blast waves," Phys. Plasmas **11**, 4968–4972.
Edens, A. D., T. Ditmire, J. F. Hansen, M. J. Edwards, R. G. Adams, P. K. Rambo, L. Ruggles, I. C. Smith, and J. L. Porter, 2005, "Measurement of the decay rate of single-frequency perturbations on blast waves," Phys. Rev. Lett. **95**, 244503.
Edwards, M. J., A. J. MacKinnon, J. Zweiback, K. Shigemori, D. D. Ryutov, A. M. Rubenchik, K. A. Keitlty, E. Liang, B. A. Remington, and T. Ditmire, 2001, "Investigation of ultrafast laser-driven radiative blast waves," Phys. Rev. Lett. **87**, 085004.
Elmegreen, B. G., 1979, "Magnetic diffusion and ionization fractions in dense molecular clouds—The role of charged grains," Astrophys. J. **232**, 729.
Elmegreen, B. G., 1998, "Observation and theory of dynamical triggers for star formation," Astron. Soc. Pac. Conf. Ser. **148**, 150.
Erlandson, A. C., Al Astanovitskiy, S. Batie, B. Bauer, A. Bayramian, J. A. Caird, C. Ebbers, J. Fuchs, H. Faretto, J. Glassman, V. Ivanov, B. LeGalloudec, N. LeGalloudec, S. Letzring, S. Payne, B. Stuart, and T. E. Cowan, 2004, "Design of a 50 TW / 20 J chirped-pulse amplification laser for high-energy-density plasma physics experiments at the Nevada Terawatt Facility of the University of Nevada," *Proceedings of the 2003 International Conference of Inertial Fusion Science and Applications*, edited by B. A. Hammel, D. D. Meyerhofer, J. Meyher-ter-Vehn, and H. Azechi (American Nuclear Society, La Grange Park, IL), pp. 626–629.
Ferland, G. J., K. T. Korista, D. A. Verner, J. W. Ferguson, J. B. Kingdon, and E. M. Verner, 1998, "CLOUDY 90: Numerical simulation of plasmas and their spectra," Publ. Astron. Soc. Pac. **110**, 761–778.
Fontaine, G., P. Brassard, and P. Bergeron, 2001, "The potential of white dwarf cosmochronology," Publ. Astron. Soc. Pac. **113**, 409–435.
Foord, M. E., S. H. Glenzer, R. S. Thoe, K. L. Wong, K. B. Fournier, B. G. Wilson, and P. T. Springer, 2000, "Ionization Processes and Charge-State Distribution in a Highly Ionized High-Z Laser-produced Plasma," Phys. Rev. Lett. **85**, 992–995.
Foord, M. E., R. F. Heeter, H.-K. Chung, P. A. M. van Hoof, J. E. Bailey, M. E. Cuneo, D. A. Liedahl, K. B. Fornier, V. Jonauskas, R. Kisielius, C. Ramsbottom, P. T. Springer, F. P. Keenan, S. J. Rose, and W. H. Goldstein, 2006, "Study of x-ray photoionized Fe plasma and comparisons with astrophysical modeling codes," J. Quant. Spectrosc. Radiat. Transf. **99**, 712–729.
Foord, M. E., R. F. Heeter, P. A. M. van Hoof, R. S. Thoe, J. E. Bailey, M. E. Cuneo, H.-K. Chung, D. A. Liedahl, K. B. Fournier, G. A. Chandler, V. Jonauskas, R. Kisielius, L. P. Mix, C. Ramsbottom, P. T. Springer, F. P. Keenan, S. J. Rose, and W. H. Goldstein, 2004, "Charge-State Distribution and Doppler Effect in an Expanding Photoionized Plasma," Phys. Rev. Lett. **93**, 055002.
Fortney, Jonathan, J., and W. B. Hubbard, 2004, "Effects of helium phase separation on the evolution of extrasolar giant planets," Astrophys. J. **608**, 1039–1049.
Foster, J. M., B. H. Wilde, P. A. Rosen, T. S. Perry, M. Fell, M. J. Edwards, B. F. Lasinski, R. E. Turner, and M. L. Gittings, 2002, "Supersonic jet and shock interactions," Phys. Plasmas **9**, 2251–2263.
Foster, J. M., B. H. Wilde, P. A. Rosen, R. J. R. Williams, B. E.

Blue, R. F. Coker, R. P. Drake, A. Frank, P. A. Keiter, A. M. Khokhlov, J. P. Knauer, and T. S. Perry, 2005, "High-energy-density laboratory astrophysics studies of jets and bow shocks," Astrophys. J. Lett. **634**, L77–L80.

Fragile, P., Chris, Stephen D. Murray, Peter Anninos, and Wil van Breugel, 2004, "Radiative shock-induced collapse of intergalactic clouds," Astrophys. J. **604**, 74–87.

Frank, A., D. Ryu, T. W. Jones, and A. Noriega-Crespo, 1998, "Effects of cooling on the propagation of magnetized jets," Astrophys. J. Lett. **494**, L79–L83.

Frieman, E. A., 1954, "On 'elephant-trunk' structures in the region of O associations," Astrophys. J. **120**, 18–21.

Fryer, C. L., 1999, "What Powers Core-Collapse Supernovae?," in *Cosmic Explosions*, edited by S. S. Holt and W. W. Zhang, AIP Conf. Proc. No. 522 (AIP, Melville, NY), p. 113.

Fryer, Chris, Adam Burrows, and Willy Benz, 1998, "Population syntheses for neutron star systems with intrinsic kicks," Astrophys. J. **496**, 333–351.

Fryer, C. L., and A. Heger, 2000, "Core-collapse simulations of rotating stars," Astrophys. J. **541**, 1033–1050.

Fryxell, B., E. Müller, and D. Arnett, 1991, "Instabilities and clumping in SN-1987A: Early evolution in 2 dimensions," Astrophys. J. **367**, 619–634.

Gaetz, T. J., Y. M. Butt, R. J. Edgar, K. A. Eriksen, P. P. Plucinsky, E. M. Schlegel, and R. K. Smith, 2000, "Chandra X-Ray Observatory arcsecond imaging of the young, oxygen-rich supernova remnant 1E 0102.2-7219," Astrophys. J. Lett. **534**, L47–L50.

Gaul, E. W., T. Ditmire, M. D. Martinez, S. Douglas, D. Gorski, G. R. Hays, W. Henderson, A. C. Erlandson, J. Caird, C. Ebbers, I. Lovanovic, W. Molander, 2005, "Design of the Texas Petawatt Laser," in *Proceedings of the Conference on Lasers and Electro-Optics/Quantum Electronics and Laser Science and Photonic Applications, Systems and Technologies*, 2005 (Optical Society of America, Washington, DC), JFB2.

Gjevik, B., 1980, in "Orographic Effects in Planetary Flows," Global Atmospheric Research Programme (GARP) Publication No. 23, World Meteorological Organization—International Council of Scientific Unions (WMO/ICSU), p. 304.

Glaze, J. A., 1976, "High-energy glass lasers," Opt. Eng. (Bellingham) **15**, 136–142.

Glimm, J., J. W. Grove, and Yongmin Zhang, 2001, "Interface tracking for axisymmetric flows," SIAM J. Sci. Comput. (USA) **24**, 208–236.

Gregory, C. D., A. D. Ash, D. M. Chambers, C. Courtois, R. A. D. Grundy, and N. C. Woolsey, 2005, "Interferometric measurements of the interaction of two plasmas in a transverse magnetic field," Astrophys. Space Sci. **298**, 389–393.

Grun, J., J. Stamper, C. Manka, J. Resnick, R. Burris, J. Crawford, and B. H. Ripin, 1991, "Instability of Taylor-Sedov blast waves propagating through a uniform gas," Phys. Rev. Lett. **66**, 2738–2741.

Guillot, T., D. J. Stevenson, W. B. Hubbard, and D. Saumon, 2004, "The interior of Jupiter," in Jupiter. *The Planet, Satellites and Magnetosphere*, edited by Fran Bagenal, Timothy E. Dowling, and William B. McKinnon, Cambridge Planetary Science Vol. 1 (Cambridge University Press, Cambridge, UK), pp. 35–57.

Guillot, Tristan, 1999, "Interiors of giant planets inside and outside the solar system," Science **286**, 72–77.

Gull, S. F., 1973, "A numerical model of the structure and evolution of young supernova remnants," Mon. Not. R. Astron. Soc. **161**, 47–69.

Guo, Zhiyu, and David N. Burrows, 1997, "ASCA observations of the supernova remnant VRO 42.05.01," Astrophys. J. **480**, 151–154.

Hansen, C. J., and S. D. Kawaler, 1995, *Stellar Interiors: Physical Principles, Structure, and Evolution* (Springer-Verlag, New York).

Hansen, J. F., M. J. Edwards, D. Froula, G. Gregori, A. Edens, and T. Ditmire, 2005, "Laboratory simulations of supernova shock wave propagation," Astrophys. Space Sci. **298**, 61–67.

Hansen, J. F., M. J. Edwards, D. Froula, G. Gregori, A. Edens, and T. Ditmire, 2006, "Laboratory observation of secondary shock formation ahead of a strongly radiative blast wave," Phys. Plasmas **13**, 022105–022111.

Hartigan, Patrick, Jon A. Morse, Bo Reipurth, Steve Heathcote, and John Bally, 2001, "Proper motions of the HH 111 jet observed with the Hubble Space Telescope," Astrophys. J. Lett. **559**, L157–L161.

Heathcote, S., J. A. Morse, P. Hartigan, B. Reipurth, R. D. Schwartz, J. Bally, and J. M. Stone, 1996, "Hubble Space Telescope observations of the HH 47 jet: Narrowband images," Astron. J. **112**, 1141–1168.

Heeter, R. F., J. E. Bailey, M. E. Cuneo, J. Emig, M. E. Foord, P. T. Springer, and R. S. Thoe, 2001, "Plasma diagnostics for x-ray driven foils at Z," Rev. Sci. Instrum. **72**, 1224–1227.

Heger, A., N. Langer, and S. E. Woosley, 2000, "Presupernova evolution of rotating massive stars. I. Numerical method and evolution of the internal stellar structure." Astrophys. J. **528**, 368–396.

Hester, J. J., P. A. Scowen, R. Sankrit, T. R. Lauer, E. A. Ajhar, W. A. Baum, A. Code, D. G. Currie, G. E. Danielson, S. P. Ewald, S. M. Faber, C. J. Grillmair, E. J. Groth, J. A. Holtzman, D. A. Hunter, J. Kristian, R. M. Light, C. R. Lynds, D. G. Monet, E. J. O'Neil, Jr., E. J. Shaya, K. P. Seidelmann, and J. A. Westphal, 1996, "Hubble space telescope WFPC2 imaging of M16—photoevaporation and emerging young stellar objects," Astron. J. **111**, 2349–2360.

Hogan, W., E. Moses, B. Warner, M. Sorem, and J. Soures, 2001, "The National Ignition Facility," Nucl. Fusion **41**, 567–573.

Holmes, N. C., M. Ross, and W. J. Nellis, 1995, "Temperature measurements and dissociation of shock-compressed liquid deuterium and hydrogen," Phys. Rev. B **52**, 15835–15845.

Hubbard, W. B., 1997, "Neptune's deep chemistry," Science **275**, 1279–1280.

Hughes, J. P., C. E. Rakowski, D. N. Burrows, and P. O. Slane, 2000, "Nucleosynthesis and mixing in Cassiopeia A," Astrophys. J. Lett. **528**, L109–L113.

Hughes, J. P., C. E. Rakowski, and A. Decourchelle, 2000, "Electron heating and cosmic rays at a supernova shock from Chandra x-ray observations of E 0102.2 7219," Astrophys. J. Lett. **543**, L61–L65.

Hwang, U., K. A. Flanagan, and R. Petre, 2005, "Chandra x-ray observation of a mature cloud-shock interaction in the bright eastern knot region of Puppis A," Astrophys. J. **635**, 355–364.

Iben, I., Jr., and R. J. Talbot, 1966, "Stellar formation rates in young clusters," Astrophys. J. **144**, 968–977.

Icke, V., G. Mellema, B. Balick, F. Eulderink, and A. Frank, 1992, Nature (London) **355**, 524–526.

Iglesias, C. A., and F. J. Rogers, 1991, "Opacity tables for Cepheid Variables," Astrophys. J. Lett. **371**, L73–L75.

Iglesias, C. A., and F. J. Rogers, 1996, "Updated OPAL opaci-

ties," Astrophys. J. **464**, 943–953.
Iglesias, C. A., and B. G. Wilson, 1994, J. Quant. Spectrosc. Radiat. Transf. **52**, 127–136.
Innes, D. E., J. R. Giddings, and S. A. E. G. Falle, 1987, "Dynamical models of radiative shocks. II. Unsteady shocks," Mon. Not. R. Astron. Soc. **226**, 67–93.
Jeffery, D. J., 1991, "Analysis of SN 1987A Polarimetry," Astrophys. J. **375**, 264–287.
Jimenez-Garate, M. A., J. C. Raymond, and D. A. Liedahl, 2002, "The structure and x-ray recombination emission of a centrally illuminated accretion disk atmosphere and corona," Astrophys. J. **581**, 1297–1327.
Jun, B. I., T. W. Jones, and M. L. Norman, 1996, "Interaction of Rayleigh-Taylor fingers and circumstellar cloudlets in young supernova remnants," Astrophys. J. **468**, L59–L63.
Kahn, F. D., 1954, "The acceleration of interstellar clouds." Bull. Astron. Inst. Neth. **12**, 187.
Kahn, F. D., 1958, "On the stability of ionization fronts," Rev. Mod. Phys. **30**, 1058–1061.
Kallman, T., and M. Bautista, 2001, "Photoionization and high-density gas," Astrophys. J., Suppl. Ser. **133**, 221–253.
Kallman, T. R., D. Liedahl, A. Osterheld, W. Goldstein, and S. Kahn, 1996, "Photoionization equilibrium modeling of iron L line emission," Astrophys. J. **465**, 994–1009.
Kallman, T. R., P. Palmeri, M. A. Bautista, C. Mendoza, and J. H. Krolik, 2004, "Photoionization Modeling and the K Lines of Iron," Astrophys. J., Suppl. Ser. **155**, 675–701.
Kane, J., D. Arnett, B. A. Remington, S. G. Glendinning, G. Bazan, R. P. Drake, B. A. Fryxell, R. Teyssier, and K. Moore, 1999, "Scaling supernova hydrodynamics to the laboratory," Phys. Plasmas **6**, 2065–2071.
Kane, J., D. Arnett, B. A. Remington, S. G. Glendinning, G. Bazan, E. Muller, B. A. Fryxell, and R. Teyssier, 2000, "Two-dimensional versus three-dimensional supernova hydrodynamic instability growth," Astrophys. J. **528**, 989–994.
Kane, J. O., D. Arnett, B. A. Remington, S. G. Glendinning, J. Castor, R. Wallace, A. Rubenchik, and B. A. Fryxell, 1997, "Supernova-relevant hydrodynamic instability experiments on the Nova laser," Astrophys. J. Lett. **478**, L175–L178.
Kane, J., R. P. Drake, and B. A. Remington, 1999, "An evaluation of the Richtmyer-Meshkov instability in supernova remnant formation," Astrophys. J. **511**, 335–340.
Kane, J. O., B. A. Remington, R. P. Drake, J. Knauer, D. D. Ryutov, H. Louis, R. Teyssier, D. Arnett, R. Rosner, and A. Calder, 2001, "Interface imprinting by a rippled shock using an intense laser," Phys. Rev. E **63**, 055401.
Kane, J. O., D. D. Ryutov, A. Mizuta, B. A. Remington, and M. W. Pound, 2005, "Molecular clouds: Observation to experiment," Astrophys. Space Sci. **298**, 261–265.
Kang, Y. G., K. Nishihara, H. Nishimura, H. Takabe, A. Sunahara, T. Norimatsu, H. Kim, M. Nakatsuka, H. J. Kong, and N. J. Zabusky, 2001, "Blast wave-sphere interaction using a laser produced plasma: An experiment motivated by supernova 1987A," Phys. Rev. E **64**, 047402.
Kang, Y. G., H. Nishimura, H. Takabe, H. Azechi, T. Norimatsu, M. Nakai, H. Nagatomo, J. Sunahara, K. Fujita, M. Nakatsuka, K. Mima, H. G. Kim, and H. J. Kong, 2000, "Hydrodynamic model experiment of the collision of supernova 1987A with its circumstellar ring using high power laser," Proc. SPIE **3886**, 489–495.
Kang, Y. G., H. Nishimura, H. Takabe, K. Nishihara, A. Sunahara, T. Norimatsu, H. Kim, M. Nakatsuka, and H. J. Kong, 2001, "Laboratory simulation of the collision of supernova 1987A with its circumstellar ring nebula," Plasma Phys. Rep. **27**, 843–851.
Keilty, K., E. P. Liang, T. Ditmire, *et al.*, 2000, "Modeling of laser-generated radiative blast waves," Astrophys. J. **538**, 645.
Keiter, P. A., R. P. Drake, T. S. Perry, H. F. Robey, B. A. Remington, C. A. Iglesias, R. J. Wallace, and J. Knauer, 2002, "Observation of a hydrodynamically-driven, radiative-precursor shock," Phys. Rev. Lett. **89**, 165003.
Keohane, J. W., L. Rudnick, and M. C. Anderson, 1996, "A comparison of the x-ray and radio emission from the supernova remnant Cassiopeia A," Astrophys. J. **466**, 309–316.
Khokhlov, A. M., P. F. Hoflich, E. S. Oran, J. C. Wheeler, L. Wang, and A. Y. Chtchelkanova, 1999, "Jet-induced explosions of core-collapse supernovae," Astrophys. J. Lett. **524**, L107–L110.
Kifonidis, K., T. Plewa, H.-Th. Janka, and E. Muller, 2000, "Nucleosynthesis and clump formation in a core-collapse supernova," Astrophys. J. Lett. **531**, L123–L126.
Kifonidis, K., T. Plewa, H.-Th. Janka, and E. Muller, 2003, "Non-spherical core-collapse supernovae. I. Neutrino-driven convection, Rayleigh-Taylor instabilities, and the formation and propagation of metal clumps," Astron. Astrophys. **408**, 621–649.
Kifonidis, K., T. Plewa, L. Scheck, H.-Th. Janka, and E. Muller, 2006, "Non-spherical core-collapse supernovae. II. The late-time evolution of globally anisotropic neutrino-driven explosions and their implications for SN 1987A," Astron. Astrophys. (to be published).
Kirshner, Robert P., 1999, "Supernovae, an accelerating universe and the cosmological constant," Proc. Natl. Acad. Sci. U.S.A. **96**, 4224–4227.
Klein, R. I., K. S. Budil, T. S. Perry, and D. R. Bach, 2000, "Interaction of supernova remnants with interstellar clouds: From the Nova laser to the Galaxy," Astrophys. J., Suppl. Ser. **127**, 379–383.
Klein, R. I., K. S. Budil, T. S. Perry, and D. R. Bach, 2003, "The interaction of supernova remnants with interstellar clouds: Experiments on the Nova laser," Astrophys. J. **583**, 245–259.
Knauer, J. P., R. Betti, D. K. Bradley, T. R. Boehly, T. J. B. Collins, V. N. Goncharov, P. W. McKenty, D. D. Meyerhofer, V. A. Smalyuk, C. P. Verdon, S. G. Glendinning, D. H. Kalantar, and R. G. Watt, 2000, "Single-mode, Rayleigh-Taylor growth-rate measurements on the OMEGA laser system," Phys. Plasmas **7**, 338–345.
Knudson, M. D., D. L. Hanson, J. E. Bailey, C. A. Hall, and J. R. Asay, 2003, "Use of a wave reverberation technique to infer the density compression of shocked liquid deuterium to 75 GPa," Phys. Rev. Lett. **90**, 035505.
Knudson, M. D., D. L. Hanson, J. E. Bailey, C. A. Hall, J. R. Asay, and W. W. Anderson, 2001, "Equation of state measurements in liquid deuterium to 70 GPa," Phys. Rev. Lett. **87**, 225501.
Knudson, M. D., D. L. Hanson, J. E. Bailey, C. A. Hall, J. R. Asay, and C. Deeney, 2004, "Principal Hugoniot, reverberating wave, and mechanical reshock measurements of liquid deuterium to 400 GPa using plate impact techniques," Phys. Rev. B **69**, 144209–144220.
Koch, J. A., O. L. Landen, B. A. Hammel, C. Brown, J. Seely, and Y. Aglitskiy, 1999, "Recent progress in high-energy, high-resolution x-ray imaging techniques for application to the National Ignition Facility," Rev. Sci. Instrum. **70**, 525–529.
Koenig, M., E. Henry, G. Huser, A. Benuzzi-Mounaix, B.

Faral, E. Martinolli, S. Lepape, T. Vinci, D. Batani, M. Tomasini, B. Telaro, P. Loubeyre, T. Hall, P. Celliers, G. Collins, L. DaSilva, R. Cauble, D. Hicks, D. Bradley, A. MacKinnon, P. Patel, J. Eggert, J. Pasley, O. Willi, D. Neely, M. Notley, C. Danson, M. Borghesi, L. Romagnani, T. Boehly, and K. Lee, 2004, "High pressures generated by laser driven shocks: applications to planetary physics," Nucl. Fusion **44**, S208–S214.

Krolik, Julian H., 1999, *Active Galactic Nuclei* (Princeton University Press, Princeton, NJ).

Kruer, W. L., 2000, "Interaction of plasmas with intense lasers," Phys. Plasmas **7**, 2270–2278.

Kuranz, C. C., R. P. Drake, D. R. Leibrandt, E. C. Harding, H. F. Robey, A. R. Miles, B. E. Blue, J. F. Hansen, H. Louis, M. Bono, J. Knauer, D. Arnett, and C. A. Meakin, 2005, "Progress toward the study of laboratory scale, astrophysically relevant, turbulent plasmas," Astrophys. Space Sci. **298**, 9–16.

Landau, L. D., and E. M. Lifshitz, *Fluid Mechanics* (Pergamon, New York).

Landen, O. L., D. R. Farley, S. G. Glendinning, L. M. Logory, P. M. Bell, J. A. Koch, F. D. Lee, D. K. Bradley, D. H. Kalantar, C. A. Back, and R. E. Turner, 2001, "X-ray backlighting for the National Ignition Facility," Rev. Sci. Instrum. **72**, 627–634.

Larsen, J. T., and S. M. Lane, 1994, "HYADES—A plasma hydrodynamics code for dense-plasma studies," J. Quant. Spectrosc. Radiat. Transf. **51**, 179–186.

Lebedev, S. V., D. Ampleford, A. Ciardi, S. N. Bland, J. P. Chittendon, M. G. Haines, A. Frank, E. G. Blackman, and A. Cunningham, 2004, "Jet deflection via cross winds: Laboratory astrophysical studies," Astrophys. J. **616**, 988–997.

Lebedev, S. V., J. P. Chittenden, F. N. Beg, S. N. Bland, A. Ciardi, D. Ampleford, S. Hughes, M. G. Haines, A. Frank, E. G. Blackman, and T. Gardiner, 2002, "Laboratory astrophysics and collimated stellar outflows: The production of radiatively cooled hypersonic plasma jets," Astrophys. J. **564**, 113–119.

Lebedev, S. V., A. Ciardi, D. J. Ampleford, S. N. Bland, S. C. Bott, J. P. Chittenden, G. N. Hall, J. Rapley, C. A. Jennings, A. Frank, E. G. Blackman, and T. Lery, 2005a, "Magnetic tower outflows from a radial wire array Z-pinch," Mon. Not. R. Astron. Soc. **361**, 97–108.

Lebedev, S. V., A. Ciardi, D. J. Ampleford, S. N. Bland, S. C. Bott, J. P. Chittenden, G. N. Hall, J. Rapley, C. Jennings, M. Sherlock, A. Frank, and E. G. Blackman, 2005b, "Production of radiatively cooled hypersonic plasma jets and links to astrophysical jets," Plasma Phys. Controlled Fusion **47**, B465–B479.

LeBlanc, J. M., and J. R. Wilson, 1970, Astrophys. J. **161**, 541–551.

Lefloch, B., and B. Lazareff, 1994, "Cometary globules. 1. Formation, evolution and morphology," Astron. Astrophys. **289**, 559–578.

Leonard, D. C., A. V. Filippenko, and T. Matheson, 2000, "Probing the Geometry of Supernovae with Spectropolarimetry," in *Cosmic Explosions*, edited by S. S. Holt and W. W. Zhang, AIP Conf. Proc. No. 522 (AIP, Melville, NY), p. 165.

Leung, C. M., 1985, in *Protostars and Planets II*, edited by D. Black and M. Matthews (University of Arizona Press, Tucson) p. 104.

Levenson, N. A., and J. R. Graham, 2001, "Shocking clouds in the Cygnus Loop," Astrophys. J. **559**, 948–953.

Levenson, N., J. R. Graham, I. S. McLean, E. E. Becklin, D. F. Figer, A. M. Gilbert, J. E. Larkin, H. I. Teplitz, and M. K. Wilcox, 2000, "Hot stars and cool clouds: The photodissociation region M16," Astrophys. J. Lett. **533**, L53–L56.

Liang, E. and K. Keilty, 2000, "An analytic approximation to radiative blast wave evolution," Astrophys. J. **533**, 890.

Liang, E., K. Nishimura, Li Hui, and S. P. Gary, 2003, "Particle energization in an expanding magnetized relativistic plasma," Phys. Rev. Lett. **90**, 085001.

Libby, S. B., M. Tabak, R. D. Hoffman, M. A. Stoyer, S. W. Haan, S. P. Hatchett, D. P. NcNabb, W. E. Ormand, J. Escher, P. Navratil, D. Gogny, M. S. Weiss, M. Mustafa, J. Becker, W. Younes, E. Hartouni, and R. A. Ward, 2004, "Prospects for investigating unusual nuclear reaction environments using the National Ignition Facility," *Proceedings of the 2003 International Conference of Inertial Fusion Science and Applications*, edited by B. A. Hammel, D. D. Meyerhofer, J. Meyher-ter-Vehn, and H. Azechi (American Nuclear Society, La Grange Park, IL), pp. 935–939.

Liedahl, Duane A., 1999, "The x-ray spectral properties of photoionized plasmas and transient plasmas," in *X-ray Spectroscopy in Astrophysics*, edited by Jan van Paradijs and Johan A. M. Bleeker (Springer-Verlag, Berlin), pp. 189–268.

Liedahl, Duane A., and Frits Paerels, 1996, "Photoionization-driven x-ray line emission in Cygnus X-3," Astrophys. J. **468**, 133–136.

Liedahl, Duane A., Patrick S. Wojdowski, Mario A. Jimenez-Garate, and Masao Sako, 2001, *Spectroscopic Challenges of Photoionized Plasmas*, edited by Gary Ferland and Daniel Wolf Savin, ASP Conference Series Vol. 247 (Astronomy Society of the Pacific, San Francisco), p. 417.

Lindl, J., 1995, "Development of the indirect-drive approach to inertial confinement fusion and the target physics basis for ignition and gain," Phys. Plasmas **2**, 3933–4024.

Lindl, J. D., P. Amendt, R. L. Berger, S. G. Glendinning, S. H. Glenzer, S. W. Haan, R. L. Kauffman, O. L. Landen, and L. J. Suter, 2004, "The physics basis for ignition using indirect-drive targets on the National Ignition Facility," Phys. Plasmas **11**, 339–491.

Livio, Mario, 1999, "Astrophysical jets: A phenomenological examination of acceleration and collimation," Phys. Rep. **311**, 225–245.

Lommen, D., L. Yungelson, E. van den Heuvel, G. Nelemans, and S. Portegies-Zwaart, 2005, "Cygnus X-3 and the problem of the missing Wolf-Rayet x-ray binaries," Astron. Astrophys. **443**, 231–241.

Loubeyre, P., *et al.*, 2004, "Coupling static and dynamic compressions: First measurements in dense hydrogen," High Press. Res. **24**, 25–31.

Lovelace, R. V. E., M. M. Romanova, and J. Contopoulos, 1993, "Theory of jets from young stars," Astrophys. J. **403**, 158–163.

Lyne, A. G., and D. R. Lorimer, 1994, "High birth velocities of radio pulsars," Nature (London) **369**, 127–129.

Matzen, M. Keith, *et al.*, 2005 "Pulsed-power-driven high-energy-density physics and inertial confinement fusion research," Phys. Plasmas **12**, 055502.

McKee, C. F., 1974, "X-ray emission from an inward-propagating shock in young supernova remnants," Astrophys. J. **188**, 335–339.

Michaut, C., C. Stehle, L. Boireau, and S. Leygnac, 2004, "Microscopic aspects of radiative shock structures," in *Proceedings of the 2003 International Conference of Inertial Fusion Science and Applications*, edited by B. A. Hammel, D. D.

Meyerhofer, J. Meyer-terVehn, and H. Azechi (American Nuclear Society, LaGrange Park, IL), p. 954–957.
Michaut, C., C. Stehle, S. Leygnac, T. Lanz, and L. Boireau, 2004, "Jump conditions in hypersonic shocks," Eur. Phys. J. D **28**, 381–392.
Miles, A. R., B. Blue, M. J. Edwards, J. A. Greenough, J. F. Hansen, H. F. Robey, R. P. Drake, C. Kuranz, and D. R. Leibrandt, 2005, "Transition to turbulence and effect of initial conditions on three-dimensional compressible mixing in planar blast-wave-driven systems," Phys. Plasmas **12**, 056317–056327.
Miles, A. R., D. G. Braun, M. J. Edwards, H. F. Robey, R. P. Drake, and D. R. Leibrandt, 2004. "Numerical simulation of supernova-relevant laser-driven hydro experiments on OMEGA," Phys. Plasmas **11**, 3631–3645.
Miles, A. R., M. J. Edwards, B. Blue, J. F. Hansen, H. F. Robey, R. P. Drake, C. Kuranz, and D. R. Leibrandt, 2004, "The effect of a short-wavelength mode on the evolution of a long-wavelength perturbation driven by a strong blast wave," Phys. Plasmas **11**, 5507–5519.
Miller, George H., 2004, "The National Ignition Facility," in *Proceedings of the 2003 International Conference of Inertial Fusion Science and Applications*, edited by B. A. Hammel, D. D. Meyerhofer, J. Meyher-ter-Vehn, and H. Azechi (American Nuclear Society, La Grange Park, IL), pp. 529–534.
Miyanaga, N., H. Azechi, K. A. Tanaka, T. Kanabe, T. Jitsuno, Y. Fujimoto, R. Kodama, H. Shiraga, K. Kondo, K. Tsubakimoto, Y. Kitagawa, H. Fujita, S. Sakabe, H. Yoshida, K. Mima, T. Yamanaka, and Y. Izawa, 2004, "FIREX petawatt laser development for fast ignition research at ILE, Osaka," in *Proceedings of the 2003 International Conference of Inertial Fusion Science and Applications*, edited by B. A. Hammel, D. D. Meyerhofer, J. Meyher-ter-Vehn, and H. Azechi (American Nuclear Society, La Grange Park, IL), pp. 507–511.
Mizuta, Akira, Jave O. Kane, Marc W. Pound, Bruce A. Remington, Dmitri D. Ryutov, and Hideaki Takabe, 2005a, "Hydrodynamic instability of ionization fronts in HII regions," Astrophys. J. **621**, 803–807.
Mizuta, Akira, Jave O. Kane, Marc W. Pound, Bruce A. Remington, Dmitri D. Ryutov, and Hideaki Takabe, 2005b, "Hydrodynamic instability of ionization fronts in HII regions—from linear to nonlinear evolution," Astrophys. Space Sci. **298**, 197–202.
Moon, S. J., S. C. Wilks, R. I. Klein, B. A. Remington, D. D. Ryutov, A. J. McKinnon, P. K. Patel, and A. Spikovsky, 2005, "A neutron star atmosphere in the laboratory with petawatt lasers," Astrophys. Space Sci. **298**, 293–298.
Moore, A. S., D. R. Symes, and R. A. Smith, 2005a, "Tailored blast wave formation: Developing experiments pertinent to laboratory astrophysics," Phys. Plasmas **12**, 052707.
Moore, A. S., D. R. Symes, and R. A. Smith, 2005b, "Tailored blast wave production pertaining to supernova remnants," Astrophys. Space Sci. **298**, 287–291.
Morse, J. A., P. Hartigan, G. Cecil, J. C. Raymond, and S. Heathcote, 1992, "The bow shock and Mach disk of HH 34," Astrophys. J. **399**, 231–245.
Moses, Edward, I., 2004, "The National Inition Facility: transition to a target shooter," in *Proceedings of the 2003 International Conference of Inertial Fusion Science and Applications*, edited by B. A. Hammel, D. D. Meyerhofer, J. Meyher-ter-Vehn, and H. Azechi (American Nuclear Society, La Grange Park, IL), pp. 535–540.
Mostovych, A. N., Y. Chan, T. Lehecha, L. Phillips, A. Schmitt, and J. D. Sethian, 2001, "Reflected shock experiments on the equation-of-state properties of liquid deuterium at 100–600 GPa (1–6 Mbar)," Phys. Plasmas **8**, 2281–2286.
Müller, E., B. Fryxell, and D. Arnett, 1991, "Instability and clumping in SN-1987a," Astron. Astrophys. **251**, 505–514.
Nellis, W. J., 2002, "Shock compression of deuterium near 100 GPa pressures," Phys. Rev. Lett. **89**, 165502.
Nellis, W. J., D. C. Hamilton, N. C. Holmes, H. H. Radousky, F. H. Ree, A. C. Mitchell, and M. Nicol, 1988, "The nature of the interior of uranus based on studies of planetary ices at high dynamic pressure," Science **240**, 779–781.
Neufeld, David A., Stephen Lepp, and Gary J. Melnick, 1995, "Thermal balance in dense molecular clouds: Radiative cooling rates and emission-line luminosities," Astrophys. J., Suppl. Ser. **100**, 132–147.
Nguyen, J. H., and N. C. Holmes, 2004, "Melting of iron at the physical conditions of the Earth's core," Nature (London) **427**, 339–342.
Norman, M. L., L. Smarr, K.-H. A. Winkler, and M. D. Smith, 1982, "Structure and dynamics of supersonic jets," Astron. Astrophys. **113**, 285–302.
Oort, J. H., 1953, paper read at Cambridge Symposium on Gas Dynamics of Interstellar Clouds.
Oort, J. H., Spitzer, L., 1955, "Acceleration of interstellar clouds by O-type stars," Astrophys. J. **121**, 6–23.
Osterbrock,Donald E.,1989, *Astrophysics of Gaseous Nebulae and Active Galactic Nuclei* (University Science Books, Mill Valley, CA).
Paerels, Frits, Jean Cottam, Masao Sako, Duane A. Liedahl, A. C. Brinkman, R. L. J. van der Meer, J. S. Kaastra, and P. Predehl, 2000, "High-resolution spectroscopy of the x-ray–photoionized wind in Cygnus X-3 with the Chandra high-energy transmission grating spectrometer," Astrophys. J. Lett. **533**, L135–L138.
Perlmutter, S., *et al.*, 1999, "Measurements of Omega and Lambda from 42 high-redshift supernovae." Astrophys. J. **517**, 565–586.
Phillips, M. E., F. P. Keenan, S. J. Rose, G. J. J. Botha, M. E. Foord, R. F. Heeter, and G. J. Ferland, 2001, "Photoionized plasma calculations using laboratory and astrophysical models," in *Spectroscopic Challenges of Photoionized Plasmas*, ASP Conference Series, Vol. CS-247, edited by Gary Ferland and Daniel Wolf Savin (Publications of the Astronomical Society of the Pacific (PASP), Brigham Young University, Provo, UT), pp. 123–126.
Poludnenko, A. Y., K. K. Dannenberg, R. P. Drake, A. Frank, J. Knauer, D. D. Meyerhofer, M. Furnish, J. R. Asay, and S. Mitran, 2004, "A laboratory investigation of supersonic clumpy flows: Experimental design and theoretical analysis," Astrophys. J. **604**, 213–221.
Pound, M. W., 1998, "Molecular gas in the Eagle Nebula," Astrophys. J. Lett. **493**, L113–L116.
Pound, M. W., Bo Reipurth, and J. Bally, 2003, "Looking into Horsehead," Astron. J. **125**, 2108–2122.
Pound, Marc W., Jave O. Kane, Bruce A. Remington, Dmitri D. Ryutov, Akira Mizuta, and Hideaki Takabe, 2005, "Eagle Nebula pillars: From models to observations," Astrophys. Space Sci. **298**, 177–181.
Pudritz, Ralph E., and Colin A. Norman, 1986, "Bipolar hydromagnetic winds from disks around protostellar objects," Astrophys. J. **301**, 571–586.
Rambo, P. K., I. C. Smith, J. L. Porter, M. J. Hurst, C. S. Speas, R. G. Adams, A. J. Garcia, E. Dawson, B. D. Thurston, C.

Wakefield, J. W. Kellogg, M. J. Slattery, H. C. Ives, R. S. Broyles, J. A. Caird, A. C. Erlandson, J. E. Murray, W. C. Behrendt, N. D. Neilsen, and J. M. Narduzzi, 2005, "Z-Beamlet: a multikilojoule, terawatt-class laser system," Appl. Opt. **44**, 2421–2430.

Rasmussen, A. P., E. Behar, S. M. Kahn, J. W. den-Herder, and K. van-der-Heyden, 2001, The X-ray spectrum of the supernova remnant 1E 0102.2-7219, Astron. Astrophys. **365**, L231–L236.

Reed, J. I., J. J. Hester, A. C. Fabian, and P. F. Winkler, 1995, "The three dimensional structure of the Cassiopeia A supernova remnant. I. The spherical shell," Astrophys. J. **440**, 706–721.

Reighard, A. B., 2006, Phys. Plasmas (to be published).

Reighard, A. B., R. P. Drake, K. K. Dannenberg, D. J. Kremer, M. Grosskopf, E. C. Harding, D. Leibrandt, S. G. Glendinning, T. S. Perry, B. A. Remington, J. Greenough, J. Knauer, T. Boehly, S. Bouquet, L. Boireau, M. Koenig, and T. Vinci, 2006, "Observation of collapsing radiative shocks in laboratory experiments" (unpublished).

Reipurth, Bo, and John Bally, 2001, "Herbig-Haro flows: Probes of early stellar evolution," Annu. Rev. Astron. Astrophys. **39**, 403–455.

Remington, B. A., D. Arnett, R. P. Drake, and H. Takabe, 1999, "Modeling Astrophysical Phenomena in the Laboratory with Intense Lasers," Science **284**, 1488–1493.

Remington, B. A., J. Kane, R. P. Drake, S. G. Glendinning, K. Estabrook, R. London, J. Castor, R. J. Wallace, D. Arnett, E. Liang, R. McCray, A. Rubenchik, and B. Fryxell, 1997, "Supernova hydrodynamics experiments on the Nova laser," Phys. Plasmas **4**, 1994–2003.

Remington, B. A., S. V. Weber, S. W. Haan, J. D. Kilkenny, S. G. Glendinning, R. J. Wallace, W. H. Goldstein, B. G. Wilson, and J. K. Nash, 1993, "Laser Driven Hydrodynamic Instability Experiments," Phys. Fluids B **5**, 2589–2595.

Remington, Bruce A., 2005, "High energy density laboratory astrophysics," Plasma Phys. Controlled Fusion **47**, A191–A203.

Remington, Bruce A., R. Paul Drake, Hideaki Takabe, and David Arnett, 2000, "A review of astrophysics experiments on intense lasers," Phys. Plasmas **7**, 1641–1652.

Ripin, B. H., C. K. Manka, T. A. Peyser, E. A. McLean, J. A. Stamper, A. N. Mostovych, J. Grun, K. Kearney, J. R. Crawford, J. D. Huba, and k. Sugitani, 1990, "Laboratory laser-produced astrophysical-like plasmas," Laser Part. Beams **8**, 183–190.

Robey, H. F., 2004, "Effects of viscosity and mass diffusion in hydrodynamically unstable plasma flows," Phys. Plasmas **11**, 4123–4133.

Robey, H. F., J. O. Kane, B. A. Remington, R. P. Drake, O. A. Hurricane, H. Louis, R. J. Wallace, J. Knauer, P. Keiter, D. Arnett, and D. D. Ryutov, 2001, "An experimental testbed for the study of hydrodynamic issues in supernovae," Phys. Plasmas **8**, 2446–2453.

Robey, H. F., A. R. Miles, J. F. Hansen, B. E. Blue, and R. P. Drake, 2003. 'Laser-Driven Hydrodynamic Experiments in the turbulent Plasma Regime: from Omega to NIF," in *Proceedings of the 2003 International Conference on Inertial Fusion Science and applications*, edited by B. A. Hammel, D. D. Meyerhofer, J. Meyer-terVehn, and H. Azechi (American Nuclear Society, LaGrange Parks, IL), p. 135.

Robey, H. F., T. S. Perry, R. I. Klein, J. O. Kane, J. A. Greenough, and T. R. Boehly, 2002, "Experimental investigation of the three-dimensional interaction of a strong shock with a spherical density inhomogeneity," Phys. Rev. Lett. **89**, 085001.

Robey, H. F., Ye Zhou, A. C. Buckingham, P. Keiter, B. A. Remington, and R. P. Drake, 2003, "The time scale for the transition to turbulence in a high Reynolds number, accelerated flow," Phys. Plasmas **10**, 614–622.

Rogers, F. J., and C. A. Iglesias, 1992, "Radiative atomic Rosseland mean opacity tables," Astrophys. J., Suppl. Ser. **79**, 507–568.

Rogers, F. J., and C. A. Iglesias, 1998, "Opacity of stellar matter," Space Sci. Rev., **85**, 61–70.

Rogers, Forest J., and Carlos A. Iglesias, 1994, "Astrophysical opacity," Science **263**, 50–55.

Rose, S. J., 1991, "Laser-produced plasma and astrophysics," Laser Part. Beams **9**, 869–879.

Rose, S. J., 1998, "The non-LTE excitation/ionization code GALAXY," J. Phys. B **31**, 2129–2144.

Rose, S. J., P. A. M. van Hoof, V. Jonauskas, F. P. Keenan, R. Kisielius, C. Ramsbottom, M. E. Foord, R. F. Heeter, and P. T. Springer, 2004, "Calculation of photoionized plasmas with an average-atom model," J. Phys. B **37**, L337–L342.

Rosen, P. A., B. H. Wilde, R. J. R. Williams, J. M. Foster, P. A. Keiter, R. F. Coker, T. S. Perry, M. J. Taylor, A. M. Khokhlov, R. P. Drake, G. R. Bennett, D. B. Sinars, and R. B. Campbell, 2005, "Recent experimental results and modeling of high-mach-number jets and the transition to turbulence," Astrophys. Space Sci. **298**, 121–128.

Ryu, D., and E. T. Vishniac, 1987, "The growth of linear perturbations of adiabatic shock waves," Astrophys. J. **313**, 820–841.

Ryutov, D. D., M. S. Derzon, and M. K. Matzen, 2000, "The physics of fast Z pinches," Rev. Mod. Phys. **72**, 167–223.

Ryutov, D. D., R. P. Drake, J. Kane, E. Liang, B. A. Remington, and W. M. Wood-Vasey, 1999, "Similarity criteria for the laboratory simulation of supernova hydrodynamics," Astrophys. J. **518**, 821–832.

Ryutov, D. D., R. P. Drake, and B. A. Remington, 2000, "Criteria for scaled laboratory simulations of astrophysical MHD phenomena," Astrophys. J., Suppl. Ser. **127**, 465–468.

Ryutov, D. D., J. O. Kane, A. Mizuta, M. W. Pound, and B. A. Remington, 2004. "Eagle Nebula: The problem of missing stiffness and the hypothesis of magnetostatic turbulence," in *Plasmas in the Laboratory and in the Universe*, edited by G. Bertin, D. Farind, and R. Pozzdi, AIP Conference Proceedings No. 703 (AIP, Melville, NY), p. 415.

Ryutov, D. D., J. O. Kane, A. Mizuta, M. W. Pound, and B. A. Remington, 2005, "Two models of magnetic support for photoevaporated molecular clouds," Astrophys. Space Sci. **298**, 183–190.

Ryutov, D. D., J. O. Kane, M. W. Pound, and B. A. Remington, 2003, "Instability of an ablatively-accelerated slab in the case of non-normal irradiation," Plasma Phys. Controlled Fusion **45**, 769–781.

Ryutov, D. D., and B. A. Remington, 2002, "Scaling astrophysical phenomena to high-energy-density laboratory experiments," Plasma Phys. Controlled Fusion **44**, B407–B423.

Ryutov, D. D., and B. A. Remington, 2003a, "A perfect hydrodynamic similarity and effect of the Reynolds number on the global scale motion," Phys. Plasmas **10**, 2629–2632.

Ryutov, D. D., and B. A. Remington, 2003b. "A perfect hydrodynamic similarity and the effect of small-scale vortices on the large-scale dynamics," in *Proceedings of the 2003 Interna-*

tional Conference on Inertial Fusion Science and Applications, edited by B. A. Hammel, D. D. Meyerhofer, J. MeyerterVehn, and H. Azechi (American Nuclear Society, LaGrange Park, IL), p. 945–949.

Ryutov, D. D., B. A. Remington, H. F. Robey, and R. P. Drake, 2001, "Magnetohydrodynamic scaling: From astrophysics to the laboratory," Phys. Plasmas **8**, 1804–1816.

Sanford, T. W. L., R. E. Olson, R. C. Mock, *et al.*, 2000, "Dynamics of a Z-pinch x-ray source for heating inertial-confinement-fusion relevant hohlraums to 120–160 eV," Phys. Plasmas **7**, 4669–4682.

Sangster, C., 2004, private communication.

Saumon, D., G. Chabrier, and H. M. Van Horn, 1995, "An equation of state for low-mass stars and giant planets," Astrophys. J., Suppl. Ser. **99**, 713–741.

Saumon, D., G. Chabrier, D. J. Wagner, and X. Xie, 2000, "Modeling pressure-ionization of hydrogen in the context of astrophysics," High Press. Res. **16**, 331–343.

Saumon, D., and T. Guillot, 2004, "Shock compression of deuterium and the interiors of Jupiter and Saturn," Astrophys. J. **609**, 1170–1180.

Scheck, L., T. Plewa, H.-T. Janka, K. Kifonidis, and E. Muller, 2004, "Pulsar recoil by large-scale anisotropies in supernova explosions," Phys. Rev. Lett. **92**, 011103.

Shigemori, K., T. Ditmire, B. A. Remington, V. Yanovsky, D. Ryutov, K. G. Estabrook, M. J. Edwards, A. J. MacKinnon, A. M. Rubenchik, K. A. Keilty, and E. Liang, 2000, "Developing a radiative shock experiment relevant to astrophysics," Astrophys. J. Lett. **533**, L159–L162.

Shigemori, K., R. Kodama, D. R. Farley, T. Koase, K. G. Estabrook, B. A. Remington, D. D. Ryutov, Y. Ochi, H. Azechi, J. Stone, and N. Turner, 2000, "Experiments on radiative collapse in laser-produced plasmas relevant to astrophysical jets," Phys. Rev. E **62**, 8838–8841.

Shigeyama, T., and K. Nomoto, 1990, "Theoretical light curve of SN 1987A and mixing of hydrogen and nickel in the ejecta," Astrophys. J., **360**, 242–256.

Shirkey, R. C., 1978, "The radio dynamical evolution of young supernova remnants," Astrophys. J. **224**, 477–87.

Shu, F. H., F. C. Adams, and S. Lizano, 1987, "Star formation in molecular clouds: Observation and theory," Annu. Rev. Astron. Astrophys. **25**, 23–81.

Shu, Frank H., Joan Najita, Eve C. Ostriker, and Hsien Shang, 1995, "Magnetocentrifugally driven flows from young stars and disks. V. Asymptotic collimation into jets," Astrophys. J. Lett. **455**, L155–L158.

Sinars, D. B., G. R. Bennett, D. F. Wenger, M. E. Cuneo, D. L. Hanson, J. L. Porter, R. G. Adams, P. K. Rambo, D. C. Rovang and I. C. Smith, 2004,"Monochromatic x-ray imaging experiments on the Sandia National Laboratories Z facility," Rev. Sci. Instrum. **75**, 3672–3677.

Spitzer, L., 1954,"Behavior of matter in space," Astrophys. J. **120**, 1–17.

Spitzer, L., 1978, *Physical Processes in the Interstellar Medium* (Wiley, New York).

Springer, P. T., *et al.*, 1992, "Spectroscopic absorption measurements of an iron plasma," Phys. Rev. Lett. **69**, 3735–3738.

Springer, P. T., *et al.*, 1997, "Laboratory measurement of opacity for stellar envelopes," J. Quant. Spectrosc. Radiat. Transf. **58**, 927–935.

Spruit, H., 1999, "Differential rotation and magnetic fields in stellar interiors," Astron. Astrophys. **349**, 189–202.

Stoeckl, C., J. A. Delettrez, J. H. Kelly, T. J. Kessler, B. E. Kruschwitz, S. J. Loucks, R. L McCrory, D. D. Meyerhofer, D. N. Maywar, S. F. B. Morse, J. Myatt, A. L. Rigatti, L. J. Waxer, J. D. Zuegel, and R. B. Stephens, 2006, "High-energy petawatt project at the University of Rochester's Laboratory for Laser Energetics," Fusion Sci. Technol. **49**, 367–373.

Stone, James, M., and Michael L. Norman, 1994, "Numerical simulations of protostellar jets with nonequilibrium cooling. III. Three-dimensional results," Astrophys. J. **420**, 237–246.

Stone, James M., Neal Turner, Kent Estabrook, Bruce Remington, David Farley, S. Gail Glendinning, and Siegfried Glenzer, 2000, "Testing astrophysical radiation hydrodynamics codes with hypervelocity jet experiments on the Nova laser," Astrophys. J., Suppl. Ser., **127**, 497–502.

Sugitani, K., M. Tamura, Y. Nakajima, C. Nagashima, T. Nagayama, H. Nakaya, A. J. Pickles, T. Nagata, S. Sato, N. Fukuda, and K. Ogura, 2002, "Near-infrared study of M-16: Star formation in the elephant trunks," Astrophys. J. Lett. **565**, L25–L28.

Suter, L. J., S. Glenzer, S. Haan, B. Hammel, K. Manes, N. Meezan, J. Moody, M. Spaeth, L. Divol, K. Oades, and M. Stevenson, 2004, "Prospects for high-gain, high yield NIF targets driven by 2ω (green) light," *Proceedings of the 2003 International Conference of Inertial Fusion Science and Applications*, edited by B. A. Hammel, D. D. Meyerhofer, J. Meyher-ter-Vehn, and H. Azechi (American Nuclear Society, La Grange Park, IL), pp. 23–34.

Sutherland, P. G., 1990, "Gamma-rays and x-rays from supernovae," in *Supernovae*, edited by A. G. Petschek (Springer-Verlag, New York), p. 111.

Sysoev, N. E., 1997, "Long-wave instability of an ionization front," Astron. Lett. **23**, 409.

Takabe, H., 2001, "Astrophysics with intense and ultra-intense lasers: Laser astrophysics," Prog. Theor. Phys. Suppl. **143**, 202–265.

Takabe H., H. Nagatomo, A. Sunahara, N. Ohnishi, A. I. Mahdy, Y. Yoda, S. Naruo, H. Azechi, H. Nishimura, and K. Mima, 1999, "Recent studies of laser produced plasmas," Plasma Phys. Controlled Fusion **41**, A75–A97.

Taylor, Mark, John Foster, Paula Rosen, Robin Williams, B. H. Wilde, T. S. Perry, P. Keiter, R. Coker, R. P. Drake, and A. M. Khokhlov, 2004 "Transition to turbulence in plasma jet experiments," in *Proceedings of the 2003 International Conference of Inertial Fusion Science and Applications*, edited by B. A. Hammel, D. D. Meyerhofer, J. Meyher-ter-Vehn, and H. Azechi (American Nuclear Society, La Grange Park, IL), pp. 485–489.

Tenorio-Tagle, G., J. Canto, and M. Rozyczka, 1988, "The formation of interstellar jets," Astron. Astrophys. **202**, 256–266.

Tipton, R., "Modeling flux compression generators with a 2D ALE code," in *Megagauss Fields and Pulsed Power Systems* (Nova Science, New York), pp. 217–231.

Trammell, S. R., D. C. Hines, and J. C. Wheeler, 1993, "Spectropolarimetry of SN-1993J in NGC-3031," Astrophys. J. **414**, L21–L24.

Tran, H. D., A. V. Filippenko, G. D. Schmidt, K. S. Bjorkman, B. T. Jannuzi, and P. S. Smith, 1997, "Probing the Geometry and Circumstellar Environment of SN 1993J in M81," Publ. Astron. Soc. Pac. **109**, 489–503.

Trunin, R. F., G. V. Boriskov, S. I. Belov, A. I. Bykov, R. I. Il'kaev, G. V. Simakov, V. D. Urlin, and A. N. Shuikin, 2005, "Shock-wave compression of hydrogen to pressures of 65 GPa," JETP Lett. **82**, 317–319.

Van Dyke, M., 1982, *An Album of Fluid Motion* (Parabolic

Press, Stanford, CA), p. 100.
Van Hoof, Peter, 2005, private communication.
Van Horn, H. M., 1991, "Dense astrophysical plasmas," Science **252**, 384–389.
Vandervoort, P. O., 1962, "On the stability of ionization fronts," Astrophys. J. **135**, 212–234.
Vishniac, E. T., 1983, "The dynamic and gravitational instabilities of spherical shocks," Astrophys. J. **274**, 152–167.
Wang, L., J. C. Wheeler, P. Hoefflich, A. Khokhlov, D. Baade, D. Branch, P. Challis, A. Filippenko, C. Fransson, P. Garnavich, R. P. Kirshner, P. Lundquist, R. McCray, N. Panagia, C. S. J. Pun, M. M. Phillips, G. Sonnenborn, and N. B. Suntzeff, 2002, "The axisymmetric ejecta of supernova 1987A," Astrophys. J. **579**, 671–677.
Wang, F. L., G. Zhao, and J. M. Yuan, 2004, "Electronic structure and radiative opacity of the metallic elements in hot and dense stellar material," Astrophys. J. **600**, 963–971.
Weber, S. V., B. A. Remington, S. W. Haan, B. Wilson, and J. Nash, 1994, "Modeling of Indirect-Drive Rayleigh-Taylor Experiments," Phys. Plasmas **1**, 3652–3661.
Wheeler, J. C., I. Yi, P. Hoflich, and L. Wang, 2000, "Asymmetric supernovae, pulsars, magnetars, and gamma-ray bursts," Astrophys. J. **537**, 810–823.
White, G. J., *et al.*, 1999, "The Eagle Nebula fingers—pointers to the earliest stages of star formation?," Astron. Astrophys. **342**, 233–256.
Whitham, G. B., 1974, *Linear and Nonlinear Waves* (Wiley, New York), p. 636.
Wilks, S. C., H. Chen, E. Liang, P. Patel, D. Price, B. Remington, R. Shepherd, M. Tabak and W. L. Kruer, 2005, "Electron-positron plasmas created by ultra-intense laser pulses interacting with solid targets," Astrophys. Space Sci. **298**, 347–355.
Williams, F. A., 1985, *Combustion Theory* (Addison-Wesley, Reading, MA).
Williams, R. J. R., 2002, "On the stability of D-type ionization fronts," Mon. Not. R. Astron. Soc. **331**, 693–706.
Williams, R. J. R., D. Ward-Thompson, and A. P. Whitworth, 2001, "Hydrodynamics of photoionized columns in the Eagle Mebula, M16," Mon. Not. R. Astron. Soc. **327**, 788–798.
Willingale, R., A. R. King, and K. A. Pounds, 1985, "EXOSAT MEDA observations of Cygnus X-3," Mon. Not. R. Astron. Soc. **215**, 295–314.
Woolsey, N. C., Y. Abou Ali, R. G. Evans, R. A. D. Grundy, S. J. Pestehe, P. G. Carolan, N. J. Conway, R. O. Dendy, P. Helander, K. G. McClements, J. G. Kirk, P. A. Norreys, M. M. Notley, and S. J. Rose, 2002, "Response to 'Comment on 'Collisionless shock and supernova remnant simulations on VULCAN,' Phys. Plasmas, 9, 727 (2002)," Phys. Plasmas **9**, 729–730.
Woolsey, N. C., Y. A. Ali, R. G. Evans, R. A. D. Grundy, S. J. Pestehe, P. G. Carolan, N. J. Conway, R. O. Dendy, P. Helander, K. G. McClements, J. G. Kirk, P. A. Norreys, M. M. Notley, and S. J. Rose, 2001, "Collisionless shock and supernova remnant simulations on VULCAN," Phys. Plasmas **8**, 2439–2445.
Woolsey, N. C., C. Courtois, and R. O. Dendy, 2004, "Laboratory plasma astrophysics simulation experiments using lasers," Plasma Phys. Controlled Fusion **46**, B397–B405.
Woosley, S., 1990, "Type I supernovae: Carbon deflagration and detonation," in *Supernovae*, edited by A. G. Petschek (Springer-Verlag, New York).
Woosley, S. E., and R. G. Eastman, 1997, "Types 1B and 1C supernovae: Models and spectra," in *Thermonuclear Supernovae, NATO Advanced Study Institute*, edited by B. Ruiz-Lapuente, R. Canal, and J. Iser (Kluwer, Dordrecht).
Xu, Jianjun, Philip E. Hardee, and James M. Stone, 2000, "The stability of radiatively cooled jets in three dimensions," Astrophys. J. **543**, 161–177.
Yamanaka, C., S. Nakai, T. Yamanaka, Y. Izawa, Y. Kato, K. Mima, K. Nishihara, T. Mochizuki, M. Yamanaka, M. Nakatsuka, T. Sasaki, T. Yabe, K. Yoshida, H. Azechi, H. Nishimura, T. Norimatsu, S. Ido, N. Miyanaga, S. Sakabe, H. Takabe, J. Jitsuno, and M. Takagi, 1987, "High thermonuclear neutron yield by shock multiplexing implosion with Gekko-XII green laser," Nucl. Fusion **27**, 19–30.